Overcoming drug resistance by stimulus-sensitive drug delivery systems –

A preclinical characterization of polymer-drug conjugates for the treatment of multi-drug resistant cancer

Dissertation

zur Erlangung des
Doktorgrades der Naturwissenschaften (Dr. rer. nat.)

der

Naturwissenschaftlichen Fakultät I – Biowissenschaften –

der Martin-Luther-Universität
Halle-Wittenberg,

vorgelegt

von Frau Anne-Kathrin Heinrich
geb. am 27.12.1986 in Hennigsdorf

Gutachter:

1. Prof. Dr. Karsten Mäder
2. Prof. Dr. Gerd Bendas
3. Prof. Dr. Lea Ann Dailey

Datum der öffentlichen Verteidigung: 26.10.2017

“Nothing in life is to be feared, it is only to be understood. Now is the time to understand more, so that we may fear less.”

— Marie Curie

Table of Contents

Table of Contents **III**

List of Abbreviations **V**

German Summary **VII**

1. Introduction **1**

1.1 Cancer and its therapeutic challenge 1

1.2 Drug delivery systems 2

1.3 Cancer nanomedicines 4

1.4 HPMA 6

1.5 Imaging procedures 7

1.6 Multispectral fluorescence imaging of HPMA copolymers 10

1.7 Aims and Objectives 11

2. Materials and Methods **12**

2.1 Materials 12

2.1.1 Polymers and polymer-drug conjugates 12

2.1.2 Fluorescence dyes 13

2.1.3 Cell lines and cell culture 14

2.1.4 Animal specification and origin 14

2.2 Methods 15

2.2.1 *In vitro* toxicity experiments 15

2.2.2 Non-invasive multispectral fluorescence imaging 16

2.2.3 Animal care and *in vivo* experiments 19

2.2.4 *Ex vivo* experiments and histological examinations 23

2.2.5 Multispectral fluorescence microscopy 25

3. Results and Discussion **28**

3.1 Comparison of different stimulus-sensitive drug delivery systems 28

3.1.1 HPMA copolymers with reduction-sensitive drug release 28

3.1.2 HPMA copolymers with enzymatic drug release 38

3.1.3 HPMA copolymers with pH-sensitive drug release 50

3.2 Therapy study with HPMA copolymers with pH-sensitive drug-release 59

3.2.1 Evaluation of a drug resistant tumor model 59

3.2.2 Verification of drug resistance *in vivo* 61

3.2.3 Determination of efficacy: Therapy study with pHPMA-doxorubicin conjugates in drug resistant tumor bearing mice 63

3.2.4 Summary 68

3.3 Investigation of the underlying mechanism of action 70

3.3.1 Influence of the treatment schedule 70

3.3.2 Examination of increased Doxorubicin delivery to the tumor site 72

3.3.3 *In vitro* testing of pH-dependent cytotoxicity 73

3.3.4 Tumor microenvironment studies by multispectral fluorescence imaging 75

3.3.5 Further investigations of a tumor-type-dependency 81

3.3.6 Multispectral fluorescence microscopy of fixed cancer cell monolayers 84

3.3.7 Multispectral fluorescence microscopy of fixed tumor xenograft sections 91

3.3.8 Summary 97

4. Summary and Perspectives 100

5. Appendix XIII

References XIII

Declaration of Original Authorship XXII

Acknowledgements XXIII

Curriculum Vitae XXV

Publications XXVI

List of Abbreviations

AD	Anno Domini
ALL	Acute lymphoblastic leukemia
BC	Before Christ
BW	Bodyweight
CA IX	Carbonic anhydrase 9
CCD	Charge-coupled device
CT	Computed tomography
DAPI	4',6-diamidino-2-phenylindole
DNA	Deoxyribonucleic acid
Dox	Doxorubicin
ECM	Extracellular matrix
EGFR	Epidermal growth factor receptor
EMA	European Medicines Agency
EPR	Enhanced permeability and retention (effect)
FCS	Fetal calf serum
FDA	Food and Drug Administration
FDG	Fluorodeoxyglucose
FI	Fluorescence imaging
FR	Folate receptor
GFLG	Gly-Phe-Leu-Gly (Tetrapeptide of Glycine, Phenylalanine, Leucine & Glycine)
H & E	Hematoxylin & Eosin
IC_{50}	Half maximal inhibitory concentration
ICG	Indocyanine green
i.p.	Intraperitoneally (injection)
i.v.	Intravenously (injection)
LCTF	Liquid crystal tunable filter

mAb	Monoclonal antibody
MDR-1	Multidrug-Resistance-Protein 1
MRI	Magnetic resonance imaging
msFI	Multispectral Fluorescence Imaging
msFM	Multispectral Fluorescence Microscopy
M_w	Weight-averaged molecular weight
NIR	Near infrared
PAMAM	Poly-amidoamine
PBS	Phosphate buffered saline
PEG	Polyethylene glycol
PET	Positron emission tomography
pHPMA	poly- N-(2-hydroxypropyl)methacrylamide
PYR	4-oxo-4-(2-pyridyl)butanoyl
RES	Reticuloendothelial system
R_H	Hydrodynamic radius
RNA	Ribonucleic acid
ROI	Region of interest
s.c.	Subcutaneously (injection)
SRB	Sulforhodamine B
TAV	Tumor Accumulation Value
TCA	Trichloroacetic acid
TfR	Transferrin receptor
TV	Tumor volume
WHO	World Health Organization
ZMG	Zentrum für Medizinische Grundlagenforschung

German Summary

Polymere Arzneistoffträgersysteme sind vielversprechende Werkzeuge um die Krebstherapie zu optimieren. Während sie den Arzneistoff gezielt in den Tumor befördern und folglich die Effektivität des Chemotherapeutikums erhöhen, vermindern sie durch die ausgeprägte Tumoranreicherung auch die toxischen Nebenwirkungen, welche aus einer Schädigung der gesunden Körperzellen resultieren. Darüber hinaus, können die positiven Eigenschaften dieser Systeme noch durch eine Stimulus-sensitive Arzneistofffreisetzung ergänzt werden. Die Stimuli, welche die Arzneistofffreisetzung induzieren, sind dabei vorzugsweise nur im Tumor besonders ausgeprägt. Dies bewirkt eine Tumor-selektive Anreicherung unter Vermeidung der peripheren Freisetzung des Chemotherapeutikums, wodurch Nebenwirkungen weiter reduziert werden und die Wirksamkeit der Therapie deutlich erhöht werden kann.

Im Zuge dieser Arbeit wurden drei verschiedene Stimulus-sensitive polymere Arzneistoffträgersysteme hinsichtlich ihrer Verteilung im Körper und der Tumor-spezifischen Arzneistofffreisetzung untersucht. Diese Systeme auf Basis von HPMA-Copolymeren wurden von den Kooperationspartnern bereitgestellt und unterschieden sich in der Art der Stimulus-sensitiven Verbindung zwischen Arzneistoff und Polymer, sowie in der Polymerarchitektur und hinsichtlich ihres Molekulargewichts. Es wurden Systeme mit reduktiver Arzneistofffreisetzung, Systeme mit einer Freisetzung, die durch lysosomale Enzyme induziert wird, wie auch pH-abhängig freisetzende Systeme untersucht. Um die Verteilung der Fluoreszenz-markierten Polymerkonjugate im Körper zu untersuchen, wurde die Methode der nicht-invasiven, nahinfraroten, multispektralen Fluoreszenztomographie angewendet.

Für alle drei Konjugate konnten sowohl eine ausgezeichnete Tumoranreicherung, als auch eine Tumor-spezifische Freisetzung des Arzneistoffmodells gezeigt werden. Darüber hinaus waren im Fall der reduktiv und der lysosomal spaltbaren Systeme, die Konjugate mit höherem Molekulargewicht nachteilig. Es ist anzunehmen, dass das höhere Molekulargewicht eine sterische Hinderung für die an der Spaltung der entsprechenden Bindung beteiligten Enzyme darstellte. Im Gegensatz dazu, zeigte sich bei dem pH-sensitiven System eine klare Überlegenheit des sternförmig aufgebauten Polymerkonjugates mit dem höheren Molekulargewicht, hinsichtlich Tumorakkumulation und Arzneistoffmodell-Freisetzung.

Aufgrund der vielversprechenden Resultate mit diesem System, wurde eine Therapiestudie an Tumor-Xenograft tragenden athymischen Nacktmäusen durchgeführt. Hierbei wurde das

Arzneistoffmodell durch das Chemotherapeutikum Doxorubicin ersetzt. Als Tumor-Xenograft wurden zwei multi-resistente Tumorzelllinien ausgewählt, um die Möglichkeit der Resistenzüberwindung mit dem Polymer-Arzneistoff-Konjugat zu prüfen. Tatsächlich konnte gezeigt werden, dass bei Applikation einer erhöhten Dosis des Konjugates, verglichen zu ungebundenem Doxorubicin, eine vollständige Tumorregression in der Therapiegruppe erreicht wurde.

In einem weiteren Versuch wurde dann untersucht, wie sich unterschiedliche Dosierungsschemata auf den Therapieerfolg auswirken. Es wurde ersichtlich, dass die Applikation einer 5- bis 6-fach erhöhten Gesamtdosis polymergebundenen Doxorubicins binnen 10 Tagen erfolgen muss, um eine Tumorregression zu erzielen. Dabei spielten die Anzahl der Injektionen und das angewendete Intervall keine Rolle bezüglich des zeitlichen Einsetzens der Regression, sehr wohl jedoch im Hinblick auf das Nebenwirkungsprofil. Das Dosierungsschema mit einer einwöchentlichen, hochdosierten Gabe des Konjugates, zeigte hier die beste Verträglichkeit bei maximalem Therapieerfolg.

Als vergleichende Studien mit einer zweiten multi-resistenten Tumorzelllinie durchgeführt wurden, fielen eine früher einsetzende Tumorantwort, wie auch ein schlechteres Nebenwirkungsprofil auf. Diese Unterschiede wurden auf ein unterschiedliches Mikromilieu im jeweiligen Tumor-Typ zurückgeführt. Vergleichende Untersuchungen des Tumormilieus beider Tumorzelllinien wurden durchgeführt, wobei das Vorhandensein und die Ausprägung von hypoxischen Arealen im Tumor zur Beurteilung des Milieus herangezogen wurden. Da Hypoxie in einem engen Zusammenhang mit der Azidifizierung des Tumorgewebes steht, wurde angenommen, dass ein hypoxisches Milieu die pH-sensitive Arzneistofffreisetzung fördert. Tatsächlich konnte gezeigt werden, dass ein hypoxisches Tumormilieu eine frühzeitige Arzneistofffreisetzung begünstigt, welche zwar zu einer früher einsetzenden Tumorantwort, jedoch auch zu erhöhten Nebenwirkungen führte.

Um eine Tumor-Typ abhängige Wirksamkeit des poly-HPMA-Doxorubicin Konjugates zu überprüfen, wurden zwei weitere, sich strukturell stark von den zuvor untersuchten Tumorzelllinien unterscheidende, Tumor-Xenograft-Modelle hinsichtlich ihres Mikromilieus untersucht. Beide wiesen, verglichen zu den zuvor untersuchten Tumorzelllinien, ein deutlich stärker hypoxisches Tumormilieu auf. Die Zelllinie mit dem stärker hypoxisch geprägten Tumormilieu, wurde für vergleichende Untersuchungen auf histologischer Ebene herangezogen. Für diese wurde die Methode der multispektralen Fluoreszenzmikroskopie eingesetzt, welche es ermöglichte, die Verteilung des polymeren Arzneistoffträgers und des Doxorubicins auf zellulärer Ebene zu visualisieren.

Während bei der Untersuchung von fixierten Zellen der drei Tumorzelllinien, keine Unterschiede hinsichtlich der Aufnahme des Konjugates und der Lokalisierung von Polymer und Arzneistoff beobachtet werden konnten, wurden bei den untersuchten Tumorschnitten selbiger Zelllinien, deutlich abweichende Verteilungsmuster ersichtlich. Damit wurde gezeigt, dass das unterschiedliche *in vivo* Verhalten des Konjugates auf Tumor-Xenograft spezifische Eigenschaften, wie etwa das Mikromilieu, zurückzuführen ist. Es konnte beobachtet werden, dass in Tumoren mit hypoxischem Mikromilieu, eine frühzeitige, interstitielle Freisetzung des Doxorubicins erfolgte, während in dem weniger hypoxischen Tumortyp, die endozytotische Aufnahme des intakten Konjugates in die Tumorzellen erfolgen konnte. Obwohl die frühe, interstitielle Freisetzung des Doxorubicins *in vivo* mit einem frühen Tumor-Ansprechen einherging, erschwerte diese die effektive Resistenzüberwindung, wie sie im Falle der Aufnahme des intakten Konjugates in die Tumorzellen möglich ist. Zwar konnten eine Anpassung der Dosis und der Anzahl der Injektionen eine Resistenzüberwindung erzielen, jedoch limitierten deutlich verstärkte Nebenwirkungen, im Falle der interstitiellen Freisetzung, die Gabe erhöhter Dosen. Es konnte demnach geschlussfolgert werden, dass ein hypoxisches Tumormilieu zwar die pH-sensitive Freisetzung begünstigt, jedoch den Therapieerfolg nachteilig beeinflussen kann. Ein angepasstes Dosisschema wäre in diesem Fall notwendig, um dennoch eine Tumorregression zu erreichen. Ferner wurde gezeigt, dass strukturelle Barrieren, wie etwa die Zusammensetzung und Menge der extrazellulären Matrix eines Tumors, die Verteilung und dadurch auch die Wirksamkeit des untersuchten Konjugates nachteilig beeinflussen.

Diese Untersuchungen haben gezeigt, dass das Mikromilieu und die strukturellen Eigenschaften eines Tumors den Therapieerfolg maßgeblich beeinflussen. Sie verdeutlichen die Wichtigkeit eines besseren Verständnisses der Zusammenhänge zwischen der Tumor-Heterogenität und der Wirksamkeit polymerer Arzneistoffträgersysteme *in vivo*. Um das Wissen dieser Zusammenhänge weiter auszubauen, sind weiterführende Studien notwendig, besonders auch mit orthotopen Tumormodellen, da diese die tatsächliche *in vivo* Situation besser repräsentieren können.

Weiterhin sollte für die Durchführung weiterführender Studien über eine Optimierung des verwendeten Konjugates nachgedacht werden. Bedingt durch den nicht bioabbaubaren

Charakter der angewendeten HPMA Copolymere, stellt die Elimination dieser Konjugate einen wichtigen Diskussionspunkt dar. Obwohl Studien von Hoffmann *et al.* eine Elimination des sternförmigen 200 kDa Konjugates binnen drei Monaten gezeigt haben, kann die stark eingeschränkte renale Elimination, bedingt durch das Molekulargewicht und den hydrodynamischen Radius, zur unerwünschten Langzeit-Akkumulation führen. Etrych *et al.* haben sternförmige HPMA Copolymere entwickelt, bei denen zwischen dem Dendrimer-Kern und den Seitenketten des Konjugates, enzymatisch spaltbare Bindungen eingefügt wurden. Diese ermöglichen, nach dem Eintritt in das Tumorgewebeeine, eine Spaltung in kleinere Bruchstücke, die dann renal eliminiert werden können. So kann die verbesserte Tumoranreicherung der hochmolekularen Konjugate ausgenutzt und deren Elimination dennoch gesichert werden. Vergleichende Studien zwischen den hier untersuchten und den optimierten, bioabbaubaren Konjugaten hinsichtlich Ihrer *in vivo* Verteilung und anti-Tumor Wirksamkeit wären von großem Interesse.

1. Introduction

1.1 Cancer and its therapeutic challenge

Excessive cell division, dedifferentiation, progressive, destructive, invasive and metastasizing behavior, these are only a few of the terrifying characteristics of cancer. Already in 460 – 375 BC the Greek physician Hippocrates used the term *carcinos* to describe malignant tumors because of their morphological appearance which reminded him of the body of a crab. Later, the Greek term was translated by the Roman physician Celsus (25 BC – AD 50) into the Latin word for crab: *cancer* (1, 2). Although this disease is as old as mankind itself, its successful therapy is undoubtedly still one of the biggest challenges in medicine. Scientists all over the world are focused on finding effective ways to beat cancer, as it is among the leading causes of death worldwide. The latest comprehensive evaluation in 2012 registered approximately 14 million of new cancer cases and about 8 million cancer related deaths. The number of annual cancer cases is expected to increase up to 22 million within the next 20 years (3). Although substantial progress has been made in cancer therapy and extensive research was done within this field in the last decades, there is still a big need to gain more knowledge about the pathogenesis of cancer, its reliable diagnosis and efficient treatment. Up to now, a variety of drugs has been developed and the number of anticancer agents on the market is still increasing. Various mechanisms of action of the chemotherapeutic agents enable combination therapies to treat cancer more efficiently and to avoid drug resistances. However, there are still numerous obstacles to overcome to make cancer lose its deadly fright. One of them is the existence of multi-drug resistance which leads to insufficient treatment of cancer and a progressive tumor growth. Despite several combination chemotherapies which should prevent the development of drug resistance, natural resistances and acquired, therapy induced resistances do still exist. Several mechanisms such as the expression of p-glycoprotein (the product of the MDR-1 gene), an efflux pump which expels e.g. chemotherapeutic drugs from the cytoplasm of the cancer cells, are responsible for lacking success in tumor treatment (4). Moreover, the safe administration of the chemotherapeutic drugs is a challenging process, as the danger of extravasates is ubiquitous. Beyond that, the severe and dose-limiting side effects of the most chemotherapeutic drugs are a huge problem. As the chemotherapeutic drugs kill all rapidly growing cells regardless of whether they are cancer cells or healthy cells, a variety of side effects can result, such as nausea and vomiting, blood disorders, pain and nervous system effects (5). Undoubtedly, these side effects strongly affect the therapeutic success and the patient's quality of life. Decreased side effects would allow higher total doses which would be beneficial for the therapeutic success. Additionally, the quality of life would be improved which is also advantageous for a successful cancer treatment. Besides the development of new anticancer drugs, the reduction of side effects is one of the main goals in cancer research. One very promising way to achieve this goal is the development of systems which allow a drug delivery to the tumor tissue more specifically.

1.2 Drug delivery systems

A prerequisite for a successful therapy is the safe and efficient delivery of the drug to its site of action within the body. For this purpose, a variety of drug delivery systems has been developed up to now. Especially in cancer treatment, drug delivery systems are of special importance. Related to the mechanism of action of the most cancer therapeutics, a tumor specific drug delivery is absolutely necessary to protect healthy cells and thereby decrease side effects. Furthermore, the total drug amount in the tumor tissue can be increased leading to a more efficient treatment (6).

The targeting of drug delivery systems specifically to the tumor tissue can be achieved by either passive or active mechanisms (6). Passive tumor targeting is based on the phenomenon of abnormal, leaky tumor vasculature which allows the entry of macromolecules to the tumor tissue. Furthermore, an insufficient lymphatic drainage which is present in most solid tumors, leads to the capture of the macromolecules within the tumor tissue. This effect is widely known as the enhanced permeability and retention (EPR) effect and was described already in 1986 by Matsumura and Maeda (7, 8). As most drug delivery systems are based on macromolecular compounds, they underlie EPR-effect mediated tumor accumulation. Multiple studies have already shown that the extent of the tumor accumulation can be modulated by the hydrodynamic radius, molecular weight, shape and surface characteristics of the respective drug delivery system, as these factors influence the circulation time within the blood stream and the tumor entrapment of the chemotherapeutic drug (9–12).

In contrast, active tumor targeting additionally makes use of special moieties which are necessary for a specific and direct tumor cell binding. A variety of targeting moieties exist, such as several receptor ligands, antibodies and peptides (10). One extensively used receptor ligand for active tumor targeting of drug delivery systems is folate. As the folate receptor (FR) is overexpressed in several tumor types such as ovarian, endometrial and colorectal carcinomas, folate is a suitable tool for the active tumor targeting of drug-delivery systems (13). Another widely used receptor ligand which can be applied for active targeting is transferrin, due to transferrin receptor (TfR) overexpression of various cancer types (14, 15).

Besides the group of receptor ligands a multitude of antibodies as targeting moieties has been investigated up to now. They are targeted to the respective antigen, represented predominantly on the surface of cancer cells. Thereby, they can deliver cytostatic drugs selectively to the tumor tissue or can act as cytostatic drugs themselves by blocking ligand-receptor interactions. For example, the monoclonal antibodies (mAb) rituximab and ofatumumab are targeted to the CD20 antigen which is expressed on the surface of B-cells. The binding of rituximab or ofatumumab induces apoptosis of CD-20 positive B-cells. Therefore, they are used for the treatment of lymphomas and forms of chronic lymphocytic leukemia (16, 17). Furthermore, drug-loaded nanoparticles with mAb on the particle surface, e.g. against the epidermal growth factor receptor (EGFR), which is overexpressed in a variety of solid tumors, are currently examined for active tumor targeting (18).

Beyond that, a peptide, such as cyclic RDG (cRDG, a cyclic pentapeptide containing the RDG sequence arginine-glycine-aspartic acid) can act as active targeting moiety due to its affinity to $\alpha v \beta 3$ integrin. As this integrin is involved in tumor angiogenesis, increased levels are present within tumor tissue. Thereby, it represents a promising tool for the tumor targeting of drugs. Furthermore, it has great potential for anticancer treatment itself as the binding of this peptide to this integrin inhibits the $\alpha v \beta 3$ integrin signaling pathway which hampers tumor angiogenesis (10, 19).

Although the methods of active tumor targeting are extensively studied and represent very promising tools for anticancer treatment, these systems also exhibit some limitations e.g. regarding the overall biodistribution, efficient tumor cell uptake and endosomal escape (10).

Besides the way of targeting, other contributing factors need to be addressed for the design of a successful drug delivery system. The "perfect drug delivery system" should be non-toxic, non-immunogenic, water-soluble, should show tumor specific accumulation and also a site-specific drug release, should exhibit elongated blood circulation, but should also be easily eliminable from the body. Unfortunately, until now this is an ambitious dream, as many pitfalls do exist.

Strong efforts regarding this purpose have been made and a variety of different drug delivery systems were developed (Fig. 1) such as nanoparticles, nanocapsules, liposomes, micelles and polymer-drug conjugates (6).

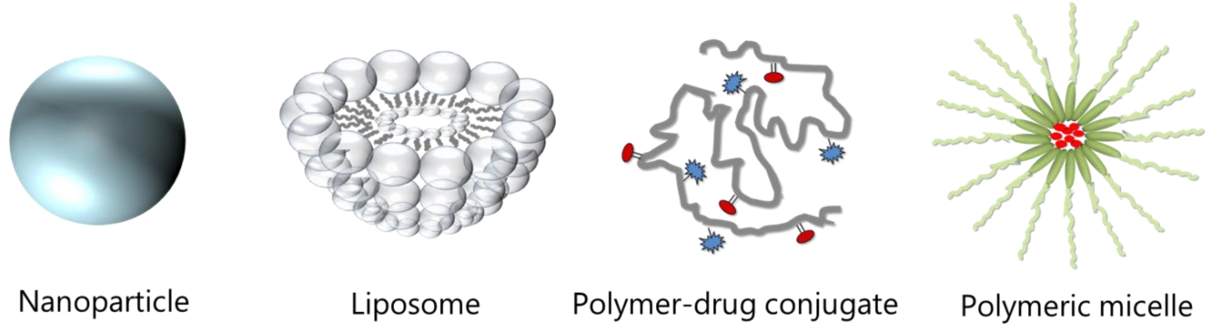

Fig. 1. Schematic structure of some nanoscaled drug delivery systems that are currently approved or at least in clinical development.

These systems are structurally completely different but all of them are able to improve the tumor specific drug delivery by either passive or additionally active targeting. Nevertheless, all of these systems have advantages but also disadvantages and they are still not "perfect". One still remaining problem is the peripheral drug release which can lead to severe side effects and an insufficient treatment. Therefore, another challenge becomes apparent: a controlled and tumor-site specific drug release. Short distances lead to a very quick diffusion of drugs from nano-scaled systems which would hamper a diffusion-controlled drug release. However, a controlled and site-specific drug release can be achieved by the design of stimulus-sensitive drug delivery systems. Here, the drug release should be triggered exclusively at the tumor site, avoiding a peripheral release. For this purpose, different stimuli can be used, such as pH, redox status, temperature or enzymes (20–23). Although a lot of work has been done within this field, the "perfect drug delivery system" still remains a dream up to now. Nevertheless, many nano-scaled drug delivery systems are currently investigated in academic research and clinical trials but despite all efforts, only a few cancer nanomedicines are approved yet.

1.3 Cancer nanomedicines

In 1995, the first cancer nanomedicine got FDA approval. It was liposomal encapsulated Doxorubicin well-known as Doxil™/Caelyx™ (9, 24, 25). Thenceforward, other nanomedicines for cancer therapy got FDA approval, such as Depocyt™ (liposomal cytarabine), Daunoxome™ (liposomal daunorubicin), Genexol-PM™ (paclitaxel polymeric micelles) and Abraxane™

(albumin-bound paclitaxel) (9). Another approved product is marketed as Oncaspar™ (26). It consists of the polyethyleneglycol (PEG)-bound enzyme asparaginase and is given to patients with acute lymphoblastic leukemia (ALL). The PEGylation led to decreased immunogenicity and prolonged half-life on the enzyme. This concept is well established today and is used for a variety of proteins such as enzymes and antibodies as well as for nano-sized formulations such as liposomes and nanoparticles (27). Another important group consists of antibody-drug conjugates (ADC's) such as Adcetris™ (brentuximab vedotin) and Kadcycla™ (trastuzumab emtansine) (28). The most recent approved cancer nanomedicine is Onivyde™, liposomal irinotecan, which got FDA approval in October 2015 (29) (Table 1).

Table 1. Examples of currently FDA-approved cancer nanomedicines

Formulation	Drug	Product name
Liposomes	Doxorubicin	Doxil™/Caelix™
	Cytarabine	Depocyt™
	Daunorubicin	Daunoxome™
	Vincristine	Marqibo™
	Irinotecan	Onivyde™
PEGylated Protein	Asparaginase	Oncaspar™
Polymeric micelles	Paclitaxel	Genexol-PM™
Nanoparticles of albumin-bound drug	Paclitaxel	Abraxane™
Antibody-drug conjugates	Monomethyl auristatin E	Adcetris™
	Emtansine (DM1)	Kadcycla™

Taking into account the extensive research regarding cancer nanomedicines, the list of approved products is quite short. The transfer from preclinical to clinical studies is a challenging process, as a lot of obstacles do exist. The scale-up can cause technical or financial challenges and clinical studies are extremely elaborated and implicate high costs and high risks. In addition, the understanding of the heterogeneous tumor pathophysiology and biology in patients and the behavior of nanomedicines is not always easily transferable from the preclinical used animal models to humans. Therefore, the clinical efficacy can be insufficient during clinical trials. Because of these obstacles, it can take a long time from the development of the system up to the approval and marketing (9, 30).

Despite the mentioned hurdles, several cancer nanomedicines already made their way to approval. The currently marketed cancer nanomedicines (examples in Table 1) comprise liposomal formulations, polymeric micelles, PEGylated proteins, nanoparticles of an albumin-bound drug and antibody-drug-conjugates (9). Regarding cancer nanomedicines in clinical development, there is a variety of further formulations such as polymeric nanoparticles- and capsules, other polymeric micelles, dendrimers and a multitude of polymer-drug conjugates. Especially the latter are very interesting, as they provided very promising results in anticancer treatment (31–34). Furthermore, they can act as theranostics due to the possibility to link imaging agents beside the drug, which allows the *in vivo* tracking of the polymer-drug conjugate with several methods. Unfortunately, no polymer-drug conjugate got approval up to now. However, several polymer-drug conjugates are currently investigated in academic research and clinical studies. Among them, a water-soluble, non-toxic and non-immunogenic synthetic polymer gained much attention: N-(2-hydroxypropyl)methacrylamide (HPMA) copolymer (Fig. 2).

1.4 HPMA

HPMA already has a quite long history. Originally developed as a plasma expander (35), Jindřich Kopeček and colleagues started to use HPMA based copolymers as drug carriers especially for low molecular weight anticancer drugs already in the mid 1970s.

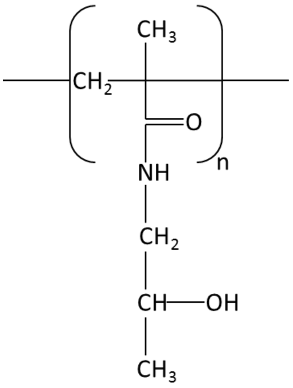

Fig. 2. Schematic structure of poly-N-(2-hydroxypropyl)methacrylamide (pHPMA)

They investigated several ways of functionalizing these copolymers and developed special linkers to induce a site-specific drug release from the polymer backbone (36, 37). Thereby, it was mainly focused on the tetrapeptide spacer GFLG, as it seemed to be suitable for a tumor specific drug release. Initially doxorubicin, a very important chemotherapeutic drug which can be found on the WHO Model List of Essential Medicines was chosen for the determination of therapeutic efficacy. In 1994, the first poly(HPMA-co-MA-GFLG-doxorubicin) conjugate entered clinical evaluation (36). Since then, several other pHPMA-drug conjugates were designed and entered clinical trials but unfortunately until now none of them got approval. The above mentioned problems of the transfer from preclinical to clinical studies are responsible for the lacking approval. Furthermore, the non-biodegradability of these polymers represents a problem which should not be neglected (38). Nevertheless, there are a lot of pHPMA-drug conjugates in academic and also in clinical research. Some are already in phase II clinical development such as ProLindac™ (AP5346), a diaminocyclohexane(DACH)platinum-pHPMA-conjugate and FCE 28068, a HPMA copolymer–GFLG–doxorubicin conjugate (39). The promising results lead to the confident hope that in near future one of these polymer-drug conjugates will take the step to approval.

However, there are still some questions to resolve especially regarding the *in vivo* behavior of these polymer-drug conjugates. Gaining more knowledge of the *in vivo* fate of the pHPMA-drug conjugates would facilitate the optimization of the conjugates and increase therapeutic success. As the visualization of nanomedicines is hampered due to their small size, special labeling techniques are necessary to allow their *in vivo* tracking. As already mentioned, polymer-drug conjugates can be labeled with different tracers additionally to the linked drug. There are several labeling methods such as radioactive or fluorescent labeling which enable the determination of the *in vivo* fate with the respective method.

1.5 Imaging procedures

One of the most important properties of an *in vivo* imaging procedure is non-invasiveness, as the *in vivo* fate of e. g. polymer-drug conjugates should be monitored over time within the same individual.

One considerable method is the positron-emission-tomography (PET). Here, radiolabeled tracers have to be injected which undergo radioactive decay within the body of the patient. The indirectly emitted gamma rays of the PET-tracers will be then detected by the PET system allowing the *in vivo* localization. A combination with computed tomography (CT) or magnetic resonance imaging (MRI) allows obtaining images giving both anatomical and metabolic information. Several metabolic processes in the body can be visualized dependent on the used

PET-tracer. ^{18}F-Fluorodeoxyglucose (FDG) is a glucose analog which is taken up by cells which usually show a high glucose uptake, a property of rapidly metabolizing cells such as cancer cells but also brain, kidneys and other tissues. Various other tracers are designed for different purposes such as $^{66/68}$Ga (gallium), $^{61/64}$Cu (copper), ^{89}Zr (zirconium), ^{82}Ru (rubidium) among many others (40). Furthermore, the radiolabeling of drug-delivery systems such as pHPMA conjugates with PET-tracers allows their *in vivo* tracking after administration (41, 42). Although PET is a highly sensitive method, it has some disadvantages such as a very complex and expensive instrumentation, the need of special safety standards due to radioactive compounds, the difficulties and high costs of tracer synthesis and their short half-lives (43). However, strong efforts are already made to improve the PET-tracers and facilitate their synthesis.

Another remarkable method for the *in vivo* tracking of drug-delivery systems is fluorescence imaging (FI). Fluorescence imaging is a non-invasive method based on measurements of the emitted light of an excited fluorophore which was previously injected into the body (44). Compared to the complex instrumentation and setting of PET, the instrumentation for the most fluorescence imaging systems is less complex and commonly available. Moreover, fluorescence imaging allows the performance of long-term observations up to several weeks to determine the *in vivo* fate of the respective drug delivery system. Due to short half-lives of the radioactive tracers, PET allows only short term studies of several hours up to days (41, 44, 45). In contrast to PET, no radioactive agents are necessary for fluorescence imaging, which simplifies the settings and safety precautions. Instead of radiolabeled tracers several fluorescence dyes can be used to track the *in vivo* fate of a nano-sized system. Therefore, the fluorescence dyes must be linked to the respective drug delivery system. A multitude of different fluorescence dyes for varying wavelength ranges are available. Usually, they are cleared rapidly from the body after i.v. administration due to renal elimination because of their low molecular weight. However, if targeted to certain tissues, they can visualize certain molecular processes or structures. Furthermore, they can be covalently linked to macromolecules such as polymeric drug delivery systems. In this case, the dye indicates their biodistribution. This can be of special interest in cancer research, as it allows the visualization of tumor accumulation of the administered drug-delivery system. Except the phenomenon of photobleaching, fluorescence dyes are comparatively stable. Nevertheless, the method of fluorescence imaging also has some limitations such as poor tissue penetration, light scattering and disturbing autofluorescence of the examined specimen. However, the development of red and NIR fluorescent dyes led to the improvement of the method as the autofluorescence at least within the NIR wavelength range, called NIR window, is nearly negligible (46). Furthermore, the development of multispectral fluorescence imaging (msFI) enabled the detection of two or more dyes simultaneously and subtraction of autofluorescence which enhanced the sensitivity of this method (44). Additionally, the simultaneous detection of two or more dyes allows statements regarding drug release which is a helpful tool to examine underlying mechanisms of action of the respective system (45). Taking everything into account, it can be concluded that msFI is eminently suitable for evaluation of the *in vivo* fate of several drug delivery systems (21, 22, 45, 47, 48).

Up to now, fluorescence imaging was predominantly used for this purpose in preclinical research especially for the *in vivo* imaging of small animals (e.g. CRi Maestro™ imaging system). However, strong efforts have been made to transfer this method to the clinic. Particularly, it is used for fluorescence image-guided surgery and for the detection of tumors. Several systems for fluorescence image-guided surgery have been developed and are currently tested in clinical trials. Moreover, some systems already got approval from FDA, EMA or both (49, 50). Most of these systems use NIR-light, as it is advantageous due to minimal autofluorescence of living tissue within this wavelength range. Furthermore, it is invisible for the human eye which is beneficial for the surgeon during surgical procedure. Novadaq SPY™ and the Photodynamic Eye (PDE™) from Hamamatsu are two examples for approved intraoperative imaging systems, which are used for a variety of surgical procedures. Amongst other important fields, fluorescence image-guided surgery systems are used for varying surgical treatments for cancer such as tumor resection or lymph node dissection (49, 50). Both Novadaq SPY™ and PDE™ make use of the fluorescent dye indocyanine green (ICG; Ex: 780 nm/Em: 810-830 nm), the predominantly used, FDA and EMA approved imaging agent for the NIR-fluorescence-image guided surgery. Once injected intravenously (i.v.), ICG interacts with plasma proteins. Thereby its NIR fluorescence is enhanced, its hydrodynamic diameter is increased and the circulation time in the blood is elongated (51). This allows the visualization of blood vessels. Furthermore, a tumor accumulation due to the EPR-effect can be achieved which helps identifying tumor tissue or lymph nodes during a surgery. Further imaging agents for this purpose can be amino acids and peptides e.g. 5-Aminolevulinic acid (5-ALA), synthetic macromolecules e.g. activatable cell-penetrating peptide (ACPP; not approved yet) or fluorescently labeled antibodies e.g. Anti-EGFR (not approved for this purpose) (50). Beside the above mentioned fluorescence image-guided surgery systems, several other are already approved or at least in clinical trials such as ArteMIS™ or fluorescence assisted resection and exploration (FLARE™) system and one multispectral system called SurgOptix T3 platform (49, 50). These and other systems in clinical development try to break through the existing hurdles like large and non-portable hardware, disturbance of the surgical workflow or poor sensitivity.

1.6 Multispectral fluorescence imaging of HPMA copolymers

As already mentioned above, msFI is extensively used in preclinical research especially for tracking the *in vivo* fate of drug delivery systems. Also pHPMA-based drug-delivery systems were investigated with this technique. By the use of msFI, the influence of molecular weight (M_w), hydrodynamic radius (R_H) and molecular architecture on the *in vivo* fate of the pHPMA conjugates linked with a NIR fluorescent dye was investigated in several biodistribution studies (11, 45). Furthermore, the influence of several linkers for the attachment of the drug to the polymer backbone was examined regarding their suitability for a tumor-site specific drug release (45, 52). The biodistribution was examined by msFI initially in healthy and later also in tumor-bearing mice. In the latter, the pHPMA conjugates exhibited excellent tumor accumulation dependent on their M_w, R_H and polymer architecture. In general, it was observable that an increased M_w led to an enhanced EPR-effect mediated tumor accumulation due to elongated circulation within the bloodstream (11, 45). It was shown that msFI is a helpful method to optimize the design of further pHPMA conjugates for the tumor-specific drug delivery. As the gathered results were very promising these systems seem to be eminently suitable for a tumor-site specific drug delivery and drug release. Furthermore, the development and comparison of further stimulus-sensitive pHPMA-drug conjugates differing in M_w, molecular architecture and drug linkers is a very interesting approach.

1.7 Aims and Objectives

Polymeric drug delivery systems are widely known to be effective tools to treat cancer. Although drug delivery to the tumor site can be increased by the use of a polymeric carrier, peripheral release of the drug can still lead to dose-limiting toxic side effects. This could be prevented by a tumor site specific drug release achieved by stimulus-sensitive polymeric drug delivery systems. The increased drug amount within the tumor and the decreased peripheral release is expected to decrease side effects and to improve the therapeutic effect. Furthermore, the use of stimulus-sensitive polymeric drug delivery systems can be very promising to overcome drug-resistance. It was one aim of this work to investigate different stimulus-sensitive drug delivery systems based on pHPMA for their potential to treat multi-drug resistant cancer effectively. Detailed investigations of influencing factors and underlying mechanisms of stimulus-sensitive polymeric drug delivery systems are rare. Therefore, it was another aim of this work to enlighten this subject. To achieve these aims, the following major objectives were addressed:

- Comparison of different stimulus-sensitive pHPMA-based drug delivery systems regarding their *in vivo* biodistribution and tumor accumulation by the use of *in vivo* msFI. In this regard, the comparison of pHPMA conjugates of different architecture and molecular weight with reduction-sensitive, enzymatic and pH-sensitive drug release was addressed. The most promising conjugate was selected for the performance of a therapy study.
- Determination of multi-drug resistance of several tumor cell lines to select a target model to demonstrate an overcoming of drug resistance by the use of the stimulus-sensitive pHPMA-drug conjugate.
- Evaluation of the impact of the applied treatment schedule on therapeutic success. Determination of an optimal balance between good tolerance and high efficacy of the pHPMA-drug conjugate.
- Investigation of several tumor xenograft models regarding their tumor microenvironment as a potential parameter for the therapeutic success.
- *In vitro* and *in vivo* examinations of the underlying mechanism of a possible tumor-type dependent therapy response. Application of multispectral fluorescence microscopy (msFM) to visualize the fate of the drug and the polymeric carrier on a cellular level.

2. Materials and Methods

In the following paragraphs all materials that were used for the experiments in this thesis are listed and the applied methods are described. Laboratory specific consumable materials like centrifuge tubes, disposable pipettes etc. were consistent with usual laboratory standards and are not listed separately.

2.1 Materials

2.1.1 Polymers and polymer-drug conjugates

The N-(2-hydroxypropyl)-methacrylamide (HPMA) copolymer precursors and HPMA-copolymer-drug conjugates were synthesized by cooperation partners of the Institute of Macromolecular Chemistry AS CR, v.v.i. in Prague, Czech Republic (Heyrovský Sq. 2, 162 06 Prague 6, Czech Republic; T. Etrych, L. Schindler (née Vystrčilová), P. Chytil, A. Koválik, R. Pola, L. Kostka, A. Hoferová, M. Studenovský).

Table 2. List of applied HPMA copolymers

Conjugate	**Description**	**Architecture**	M_w	**DY-782 (polymer label)**	**DY-676 (drug model)**	**CY-7 (polymer label)**	**Doxorubicin**
R*L*30	HPMA copolymer with reduction sensitive drug-release	Linear	30 kDa	2.6 % wt	0.7 % wt	-	-
R*L*104		Linear	104 kDa	2.8 % wt	0.7 % wt	-	-
E*L*35	HPMA copolymer with enzymatic drug-release	Linear	35 kDa	1.7 % wt	0.9 % wt	-	-
E*D*170		Dendritic	170 kDa	1.9 % wt	1.9 % wt	-	-
A*S*190DoxF	HPMA copolymer with pH-sensitive drug-release	Star-like	190 kDa	0.6 % wt	-	-	9.7 % wt
A*S*200Dox		Star-like	200 kDa	-	-	-	9.7 % wt
A*S*180DoxF		Star-like	180 kDa	-	-	0.76 % wt	10.6 % wt

The synthesis of the HPMA-copolymers and conjugation of fluorescence dyes and Doxorubicin was based on previously described methods and is not part of this thesis. For i.v. or intraperitoneal (i.p.) injection and *in vitro* experiments the lyophilized polymer conjugates were dissolved in PBS and sterile filtered (0.2 µm Millex, Millipore, U.S.A.). The pHPMA conjugates which were used within this thesis are summarized in Table 2. Detailed structures of the applied HPMA-copolymer-drug conjugates are displayed respectively in the beginning of the chapter where their investigation is described.

2.1.2 Fluorescence dyes

The fluorescence dyes DY-782 (NHS ester) and DY-676 (amine) used for polymer labelling were purchased from Dyomics GmbH, Germany. Furthermore the fluorescence dye CY®-7 (Cyanine 7 NHS ester), also used for polymer labelling, was obtained by Lumiprobe GmbH, Germany. Chemical structures of the applied dyes are displayed in Fig. 3.

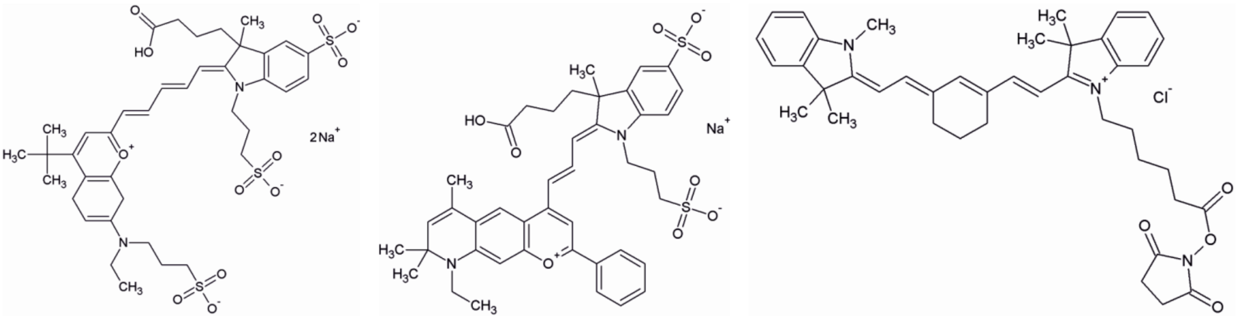

DY-782 DY-676 CY-7

Fig. 3. Fluorescence dyes which were used either for stable labeling of the pHPMA-backbone (DY-782, CY-7; NIR emission) or acting as a drug model (DY-676; far red emission).

These cyanine dyes possess absorbance and emission wavelengths in the far red up to near infrared (NIR) region. This allows the visualization in living tissues using the NIR window. Besides low autofluorescence of living tissue within this wavelength range, a deep tissue penetration can be achieved. Furthermore, for characterization of the tumor microenvironment, the fluorescent imaging agent Hypoxisense® (Perkin Elmer, U.S.A.) was used. It is targeted to carbonic anhydrase IX (CA IX) which is known to be a marker for hypoxia.

2.1.3 Cell lines and cell culture

The human germ cell tumor cell line 1411HP was chosen as a drug resistant model. This cell line was originally provided by Prof. P. W. Andrews (Centre for Stem Cell Biology, University of Sheffield, Sheffield, UK) in 1997. A2780cis is the drug resistant variant of the human ovarian carcinoma cell line A2780 - a drug sensitive model that was also used for comparative experiments. Both cell lines were provided by Prof. G. Bendas (Pharmaceutical Institute, Rheinische Friedrich-Wilhelms-University Bonn, Germany) in 2014. Originally, both cell lines were purchased from the European Collection of Authenticated Cell Cultures (ECACC). The acquired drug resistance of A2780cis was artificially established derived from the cell line A2780, whereas 1411HP represents a model of natural drug resistance. Therefore, these models are suitable for the development of methods to overcome drug resistance. As 1411HP and A2780cis show very similar tumor substructures, experiments were additionally performed with drug resistant tumor cell lines that exhibit different morphological properties. Therefore, the naturally multi-drug resistant human colorectal-carcinoma cell lines DLD-1 and HT-29 were chosen to evaluate a potential structure dependent efficacy of the therapies. The tumor cells were cultivated with RPMI 1640 medium containing stable L-Glutamine and Phenol Red (Sigma-Aldrich Chemie GmbH, Germany). Furthermore, 10 % Fetal Calf Serum (FCS; Biochrom AG, Berlin, Germany) and 10 % Penicillin/Streptomycin (100-fold stock solution; Merck Chemicals GmbH, Germany) were added. Incubation was conducted at 37 °C and 5 % CO_2. The detachment of adherent tumor cells was performed with Trypsin-EDTA (Sigma-Aldrich Chemie GmbH). Phosphate buffered saline (PBS; Sigma-Aldrich Chemie GmbH) was used for the washing steps during cell passage. The consumable materials for the cell culture (e.g. well plates, bottles etc.) were obtained by TTP Techno Plastic Products AG, Switzerland. For the microscopic examination of the cell cultures an inverted light microscope (Axiovert 40 CFL, Carl Zeiss Microscopy GmbH, Germany) was used.

2.1.4 Animal specification and origin

For the experiments in this thesis male athymic nude mice (Hsd:Athymic Nude-*Foxn1*^{nu}) were used. They were purchased either from Harlan Winkelmann GmbH, Germany or from the breeding of the ZMG of the Martin Luther University Halle-Wittenberg, Germany.

2.2 Methods

2.2.1 *In vitro* toxicity experiments

The sulforhodamine B (SRB) assay was used for determination of the *in vitro* toxicity. This assay, developed by Skehan *et al.* in 1990 (53), is a common method for cytotoxicity screening. SRB is able to bind cellular proteins in acidic milieu. Therefore, the colorimetric measurement of the cellular protein content allows determination of the cell density. To perform this assay, the respective cancer cells were seeded in 96-well plates. The optimal number of cells of the respective cell line per well was chosen in accordance to results of previous experiments. The cells were incubated at 37 °C and 5 % CO_2 for 24 h. Now serial dilutions (0.001-10 µM) of either free doxorubicin (Sigma-Aldrich Chemie GmbH) or pHPMA-doxorubicin conjugate stock solutions (1.44 mM) were prepared with RPMI-medium to replace the medium in the 96-well plates. For the determination of the pH-dependent cytotoxicity of the pH-sensitive pHPMA-doxorubicin conjugate the stock solutions (1.44 mM) were incubated with phosphate buffers of different pH values (5.5 to 7.4) and stored at 37 °C for 24 h. Then they were used to prepare the serial dilutions as described above and added to the cells. Each column (8 wells) was incubated with a certain concentration except one column which was incubated with drug-free RPMI-medium as a control. After a certain incubation time (2 or 96 h) the supernatant was removed and the cells were fixed by adding 10 % (wt/vol) trichloroacetic acid (TCA). The well plates were stored for at least 2 h at 4 °C. Afterwards the TCA was removed and plates were washed five times with distilled water using the Plate Washer 96 PW (Tecan, Switzerland). Now cells were stained with SRB-solution (0.4 % in 1 % (vol/vol) acetic acid) (Sigma-Aldrich Chemie GmbH) for 30 minutes at room temperature. The unbound dye was removed by washing the plates with 1 % (vol/vol) acetic acid using the plate washer again. The plates were allowed to dry at room temperature for at least 8 h. For the measurement of the optical density the protein-bound dye was dissolved by adding 100 µl of 10 mM TRIS buffer to each well. The dye quantification was performed at 570 nm using a microplate reader (SpectraFluor Plus, Tecan, Switzerland). For the determination of the IC_{50} values dose-response curves were evaluated using Excel® software (Microsoft®) showing the concentration dependent cell growth inhibition (%). Exact IC_{50} values were then calculated by linear interpolation.

2.2.2 Non-invasive multispectral fluorescence imaging

2.2.2.1 Instrumentation and settings

Non-invasive msFI was carried out on a Maestro™ *in vivo* imaging system from CRi (Cambridge Research and Instrumentation, U.S.A.). A 300 W xenon lamp was used as excitation light source. The light passed a narrow band excitation filter which only allows the passage of light of a certain wavelength range. The filtered light was transferred to the illumination module via fiber-optics. Inside the illumination module, the specimen was placed on a height adjustable table and was illuminated by four height adjustable illumination arms (Fig. 4).

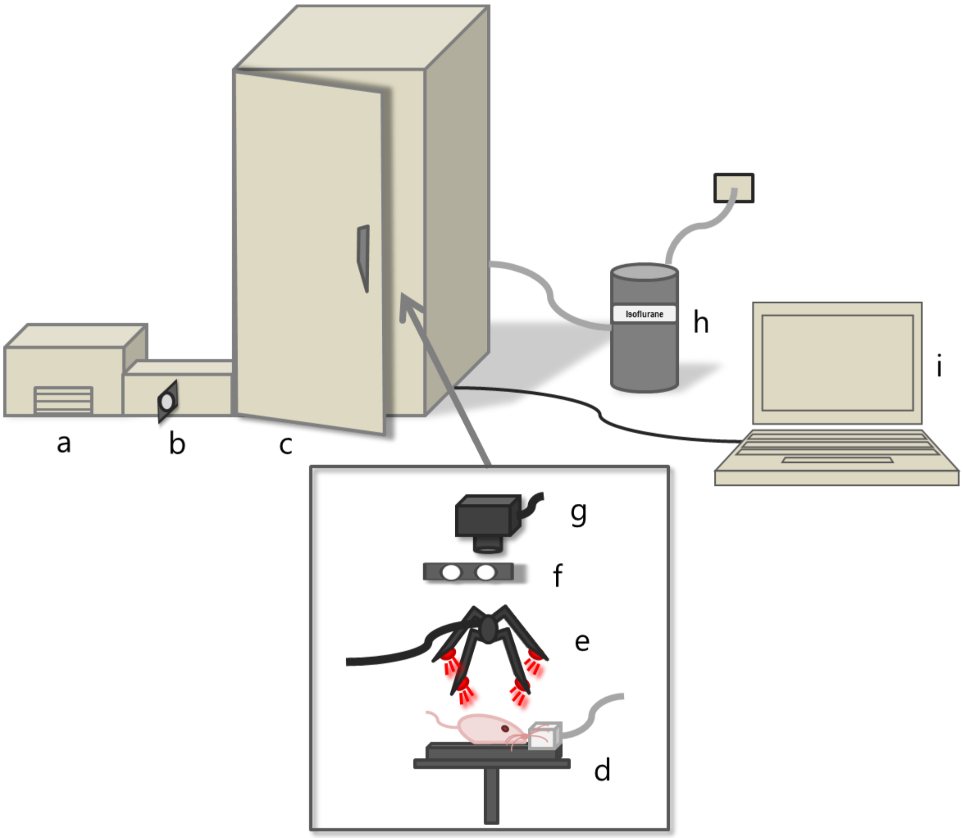

Fig. 4. Scheme of the Maestro™ *in vivo* imaging system. a – Xenon lamp (excitation light); b – Narrow band excitation filter; c – Imaging module; d – Height adjustable table with warming plate and anesthesia mask; e – Height adjustable illumination arms; f – Longpass emission filter; g – Liquid crystal tunable filter and 1.5 megapixel CCD camera; h – Anesthesia system for inhalation anesthesia; i – PC with Maestro™ software.

The emitted fluorescence light passed a longpass emission filter which excluded the excitation light. Dependent on the applied fluorophore different filter sets were used. Furthermore, it was possible to combine filter sets for measurements of two or more different dyes simultaneously.

They are summarized in Table 3. Following this pre-filtration step, the light passed a software controlled liquid crystal tunable filter (LCTF) which allowed the nm-precise scanning of the chosen wavelength range. The step-bandwidth was adjusted on 10 nm for all measurements. Afterwards the light was detected by a cooled (8 °C) 1.5 megapixel CCD camera. The software (Maestro™ software version 2.10.0.) was used to calculate a cube which consists of a series of images taken at specific wavelengths. It contains the complete spectral information for each pixel of the image. The binning was set 2 x 2 in order to find a balance between exposure time, signal intensity and resolution. This adjustment led to a decrease of resolution by a factor of 4 which is necessary to increase the signal intensity and to keep the file size manageable. The resulting cubes had an image size of 696 x 520 pixels. For the cube acquisition automatic exposure tool was used to avoid over- or underexposure.

Table 3. Applied filter sets for the Maestro™ *in vivo* imaging system

Filter Set	Excitation Filter	Emission Filter	Acquisition Settings
Blue	445 – 490 nm	515 nm longpass	500 – 720 nm (10 nm steps)
Red	615 – 665 nm	700 nm longpass	680 – 950 nm (10 nm steps)
NIR	710 – 760 nm	800 nm longpass	780 – 950 nm (10 nm steps)

2.2.2.2 Data evaluation and image processing

The analysis of an acquired cube was enabled by the use of a spectral library which was prepared in advance. It consists of the previously recorded reference emission spectra of the used dyes, background and mouse/cell autofluorescence (Fig. 5). The respective dyes were dissolved in PBS to detect the reference spectra. Additionally, an untreated mouse was imaged to detect the autofluorescence spectrum at the respective wavelength range. This enabled spectral unmixing, a tool of the Maestro™ software, to subtract autofluorescence and background signal from the signal of interest and to distinguish the fluorescence signals of the used dyes. The resulting single spectral components were displayed in a greyscale image which can be used for evaluation. Furthermore, the single greyscale images can be merged in a pseudo-colored composite image. This allows the visualization of the distribution of several signals within one image. A representative example for this process is displayed in Fig. 6.

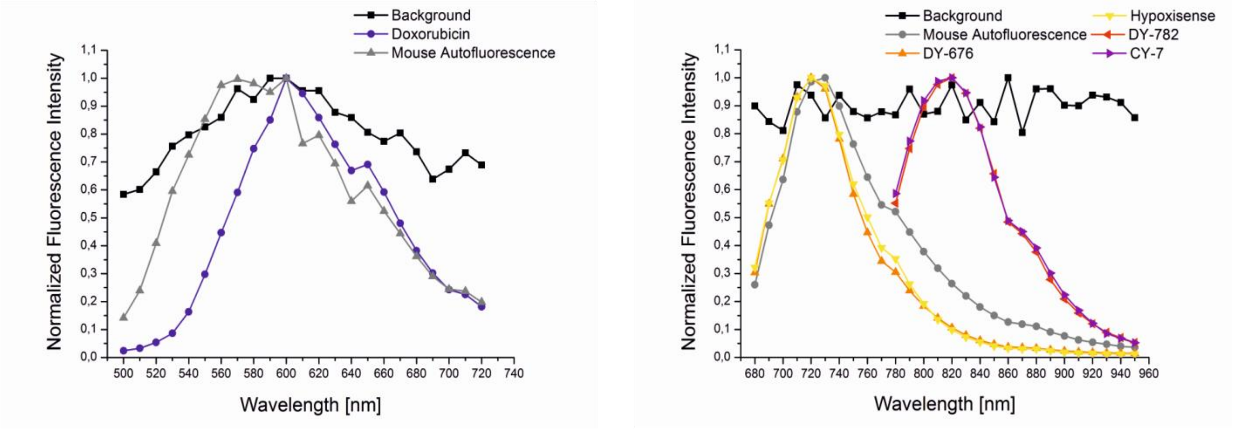

Fig. 5. Left plot – Emission spectra of doxorubicin, mouse autofluorescence and background in the blue wavelength range (blue filter set); right plot – Emission spectra of DY-676, DY-782, CY-7, Hypoxisense®, mouse autofluorescence and background in the red and NIR wavelength range (combined red and NIR filter sets).

The evaluation of the respective spectral component greyscale image was performed either by drawing a region of interest (ROI) or automatically by setting a threshold. As a result the software displayed a fluorescence intensity value normalized by exposure time, camera gain and binning. For the comparison of the greyscale component images the “compare image” tool of the software was used. It permits the visualization of different intensities over time. This tool displayed all greyscale images on the same scale, taking differences in exposure time into account. The images can be displayed with several color profiles to improve visualization. All images within this thesis are displayed in the “hot” color profile. Within this profile, white color indicates a strong signal whereas dark red indicates a weak signal.

The software also creates a scale bar for the compared images where fluorescence intensity is assigned to the respective color. The scale unit of the scale bars for the compared images and also for the displayed fluorescence intensity graphs is “scaled counts per second”. This value is calculated by the software from the fluorescence counts by the following formula:

$$\text{Scaled Counts/Second} = \frac{\text{counts}}{2^{\text{bit depth}}} \times \frac{1}{\text{exposure time (s)}} \times \frac{1}{\text{binning}^2} \times \frac{1}{\text{gain}}$$

For all experiments a fixed bit depth [12], camera gain [3] and binning [2x2] was used.

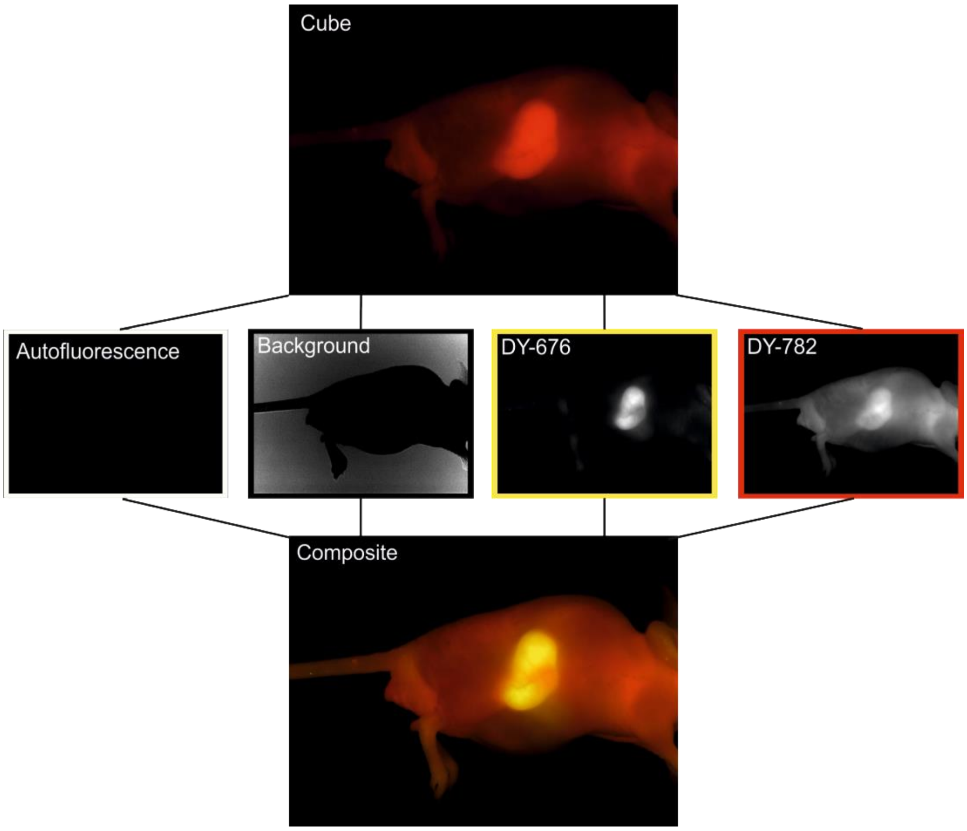

Fig. 6. Representative example for the unmixing procedure. A mouse received an injection of double labeled (DY-676 & DY-782) pHPMA conjugate. By msFI a cube (top) was acquired which contained the complete spectral information for a defined wavelength range. By using the unmixing tool, the spectral information was split in the single spectral species: autofluorescence (here negligible because of NIR wavelength range), background, DY-782 and DY-676 (middle). They can be evaluated and further combined to a composite image (bottom) which represents an overlay of the single spectral species and allows the localization of the signal of interest.

2.2.3 Animal care and *in vivo* experiments

All experiments complied with regional guidelines and regulations and were approved by the local authority in Saxony-Anhalt. Male athymic nude mice (from Harlan Winkelmann, Germany or from the breeding of the ZMG of the Martin Luther University Halle-Wittenberg, Germany) were kept under controlled conditions (12 h day/night cycle, 24 °C). After 2 weeks of setting in period, the mice were short-time anesthetized using isoflurane (Forane®, Abbott, Germany) for subcutaneous tumor cell injection. Tumor cells (either $1x10^7$ cells 1411HP, $5x10^6$ cells A2780, $5x10^6$ cells A2780cis, $5x10^6$ cells DLD-1 or $5x10^6$ cells HT-29), suspended in 150 µl of PBS were subcutaneously (s.c.) injected either to the right or to the left side of the respective mouse.

In some experiments two different tumor xenografts were established simultaneously at the right and left side of the mice. Mouse weight and tumor size were measured continuously. Furthermore tumor volume (V) was estimated after caliper measurement based on length (l) and width (w) by using the equation according to Tomayko *et al.* (54):

$$V = {}^{\pi}/_{6} \times l \times w^2$$

The increase of the tumor volume normalized to day 0 or 1st day of treatments (d1) was then plotted over time. Whenever it was possible, the results were calculated as means and standard deviation was used as error bars.

During the imaging process, mice were anesthetized with isoflurane in oxygen (2 L/min) using an initial dose of 2.5 % and a maintenance dose of 1-2 %. Furthermore, mice were placed on a warming plate (35 °C) during anesthesia to avoid a decrease of body temperature.

2.2.3.1 Biodistribution and tumor accumulation of HPMA copolymers with reduction sensitive drug release

The biodistribution and tumor accumulation of HPMA copolymers, stably labeled with a NIR dye (DY-782), and of the reduction sensitive cleavable drug model (DY-676) was investigated in 2 human colon carcinoma xenograft-bearing athymic nude mice. The DLD-1 tumor xenografts were established on the right side and HT-29 tumor xenografts on the left side of the mice. When the tumors reached an average size of 0.47 cm^3 ± 0.18 cm^3 treatments were started. The linear 30 kDa (**R***L*30) and 104 kDa (**R***L*104) HPMA copolymers (100 µL PBS solution containing 1.5 mg polymer) were i.v. injected into the tail vein of mice. The mice were observed for 3 days. MsFI was performed using the red and NIR-filter set directly, 24, 48 and 72 h after i.v. injection. Afterwards, the mice were sacrificed for *ex vivo* examination of organs and tumors.

2.2.3.2 Biodistribution and tumor accumulation of HPMA copolymers with enzymatic drug release

The distribution and tumor accumulation of HPMA copolymers, stably labeled with a NIR dye (DY-782), and of the enzymatically cleavable drug model (DY-676) were investigated in 4 human colon carcinoma xenograft-bearing athymic nude mice). The DLD-1 tumor xenografts were established on the right side and HT-29 tumor xenografts on the left side of the mice.

When the tumors reached an average size of 0.37 cm^3 ± 0.29 cm^3 in each group, treatments were started. The linear 35 kDa (**E***L*35) and the dendritic 170 kDa (**E***D*170) HPMA copolymers (100 µl PBS solution containing 1.5 mg polymer) were i.v. injected into the tail vein of mice (each n = 2). The mice were observed for 3 days and in a long-term experiment for 14 days. MsFI was performed using the red and NIR-filter set directly, 24, 48 and 72 h after i.v. injection. In case of the two weeks experiment fluorescence imaging was performed directly, 24, 48, 72, 144, 192, 240 and 312 h after i.v. injection. Afterwards, the mice were sacrificed for *ex vivo* examination of organs and tumors.

2.2.3.3 Biodistribution and tumor accumulation of HPMA copolymers with pH-sensitive drug release after i.v. and i.p. administration

The biodistribution and tumor accumulation of a HPMA copolymer, stably labeled with a NIR dye (DY-782) and loaded with doxorubicin linked via pH-sensitive cleavable hydrazone bond to the polymer backbone was investigated in 4 DLD-1 human xenograft colon carcinoma–bearing athymic nude mice. When the tumors reached an average size of 1.13 cm^3 ± 0.40 cm^3 in each group, treatments were started. The star-like structured 190 kDa HPMA copolymer **A***S*190DoxF (the concentration of the doxorubicin loaded HPMA copolymer was chosen according to a doxorubicin concentration of 1.25 mg/mL PBS) was injected either i.v. or i.p. into the respective mice according to a doxorubicin concentration of 5 mg/kg bodyweight (BW) (each n = 2). The mice were observed for 5 days. MsFI was performed using the red and NIR-filter set directly, 1, 24, 72 and 120 h after injection. Afterwards, the mice were sacrificed for *ex vivo* examination of organs and tumors.

2.2.3.4 Drug resistance study

To compare the *in vivo* doxorubicin sensitivity of the resistant models 1411HP and A2780cis with the sensitive ovarian carcinoma model A2780, respectively, 10 1411HP, A2780cis and A2780 tumor xenograft bearing athymic nude mice were examined. The mice were even subdivided into PBS-Control groups (each n = 5) and doxorubicin therapy groups (each n = 5). When the tumors reached an average size of 0.30 cm^3 ± 0.01 cm^3 in each group treatments were started. Mice received either PBS or doxorubicin (5 mg/kg BW) i.v. at day 1, 4 and 9

(A2780 at day 10 instead, A2780cis only day 1 & 4). Tumor volume and mice bodyweight were measured continuously until the mice needed to be sacrificed due to tumor burden.

2.2.3.5 Therapy study

To investigate therapeutic efficacy of the pHPMA-doxorubicin conjugate, 21 1411HP-tumor xenograft bearing athymic nude mice were examined. The mice were divided into 4 groups according to their tumor size (Mean tumor volume 0.25 cm^3 ± 0.02 cm^3) and received either injections of pHPMA-doxorubicin conjugate, free doxorubicin, pHPMA precursor or PBS. The pHPMA-doxorubicin conjugate and also pHPMA precursor were dissolved in PBS according to a doxorubicin concentration of 1.25 mg/mL for i.v. injection. Bodyweight and tumor volume was monitored continuously until mice needed to be sacrificed due to tumor burden or side effects (>20 % loss of bodyweight). Furthermore, 2 A2780cis tumor xenograft bearing athymic nude mice received injections of the pHPMA-doxorubicin conjugate according to the treatment schedule which was applied in 1411HP tumor type to investigate its efficacy and toxicity.

2.2.3.6 Treatment schedule determination and Doxorubicin accumulation

For the investigation of enhanced doxorubicin accumulation 10 1411HP tumor xenograft bearing athymic nude mice were examined. The mice were treated with either free doxorubicin (5 mg/kg BW), 1-, 2- and 3-fold doxorubicin equivalent dose of the pHPMA-doxorubicin conjugate or PBS as a control when tumors had an appropriate volume for imaging procedure (0.75 cm^3 ± 0.25 cm^3). 48 h after i.v. injection, mice were sacrificed, tumors necropsied and examined by msFI using the blue filter set to compare the extent of doxorubicin accumulation.

To determine the effect of different treatment schedules, 9 1411HP and 3 A2780cis tumor xenograft bearing athymic nude mice were examined. They were treated with either pHPMA-doxorubicin conjugate or PBS when tumors reached an average size of 0.28 cm^3 ± 0.05 cm^3. Bodyweight and tumor volume was monitored continuously until mice needed to be sacrificed due to tumor burden or side effects (>20 % loss of bodyweight).

2.2.3.7 Tumor microenvironment studies

For examinations of the tumor microenvironment, again 1411HP-tumor xenografts were established in 6 athymic nude mice. When tumor volume was appropriate (0.75 cm^3 ± 0.25 cm^3), different treatment schedules were tested. The schedules comprised injections of either a combination of pHPMA-Dox conjugates with following Hypoxisense® injection (100 µL in PBS; 2 nmol/100 µL) or only the Hypoxisense® injection as a control. 24 h after Hypoxisense® injection mice were sacrificed, tumors were necropsied and cross-sectioned to perform *ex vivo* msFI using the blue, red and NIR-filter set. Additionally a A2780cis tumor xenograft bearing mouse received a Hypoxisense® injection without any other previous treatment and was sacrificed 24 h after injection to perform *ex vivo* examination of the necropsied tumor by msFI using the red filter set.

2.2.4 *Ex vivo* experiments and histological examinations

The necropsied tumors and organs were examined to gather more information. Therefore, a certain time after the respective injection mice were sacrificed and tumors and organs were necropsied, placed on a 12-well plate and examined using the blue, red or NIR filter set depending on the previous injection. Furthermore, the tumors were cross-sectioned and examined individually by msFI. For the comparison, the measured fluorescence intensities were normalized by the tumor area and exposure time.

The hematoxylin and eosin (H & E) staining is one of the most commonly used staining methods. It consists of two dyes which are used to stain different cell components. This was necessary, as unstained tissue sections exhibited a lack of contrast. The staining with different dyes allows the distinction of different cell components. The dye hematoxylin stains acidic/basophilic structures like DNA or RNA containing cell components such as nucleus, ribosomes and the endoplasmic reticulum, in a deep purple color whereas the acidic dye eosin is used to stain basic/acidophilic structures, e.g. the cytoplasm, pink. Erythrocytes appear in bold red. For the H & E staining, necropsied tumors were cross-sectioned, fixed in 4 % formalin, embedded in paraffin, sliced with a Leica RM 2245 microtome (3 - 4 µm), dewaxed and rehydrated by decreasing alcohol series from xylene up to bi-distilled water. Afterwards the slices were stained with hematoxylin (Dako, Germany), followed by several washing steps with tap water and bi-distilled water. Subsequently, the slices were stained with eosin (Merck

Chemicals GmbH, Germany). After staining, the slices were de-hydrated by ascending alcohol series and fixed with Roti®-Histokitt (Carl Roth GmbH & Co. KG, Germany). A representative example is displayed in Fig. 7.

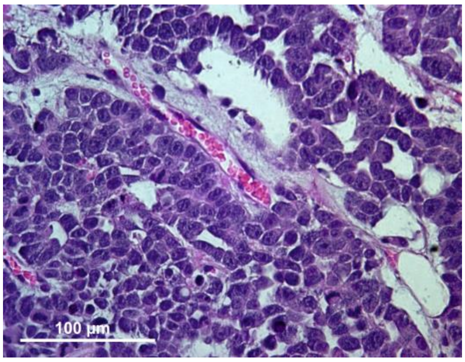

Fig. 7. Microscopic image (400x magnification) of an H & E stained 1411HP tumor section. Cell nuclei appear in deep purple, cytoplasm in light purple/pink and erythrocytes in bold red.

For the azan staining, the dewaxed and rehydrated tissue slices were initially stained with an azocarmine (Morphisto®, Germany) solution. After some washing steps with bi-distilled water and the nuclei differentiation with aniline (Baacklab®, Germany) in 95 % ethanol, the slices were treated with 5 % phosphomolybdic acid (Baacklab®, Germany). Subsequently, they were rinsed with bi-distilled water and stained with a solution of aniline blue and Orange G (Baacklab®, Germany). Afterwards, the slices were washed with bi-distilled water, dehydrated by ascending alcohol series and fixed with Roti®-Histokitt (Carl Roth GmbH & Co. KG, Germany). A representative example is displayed in Fig. 8.

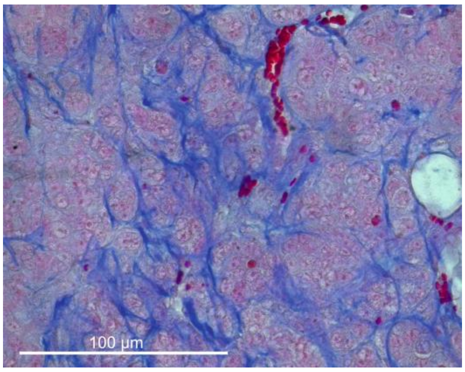

Fig. 8. Microscopic image (400x magnification) of an azan stained HT-29 tumor section. Cell nuclei appear in dark red and collagen appears blue.

2.2.5 Multispectral fluorescence microscopy

For the examination of fixed tumor cells or fixed tumor sections an upright Leica DM4000B transmitted-light microscope combined with a Nuance® Ex multispectral imaging system from PerkinElmer (U.S.A.) (containing software controlled liquid crystal tunable filter (LCTF) and CCD Chip, Sony ICX285) was used (Fig. 9).

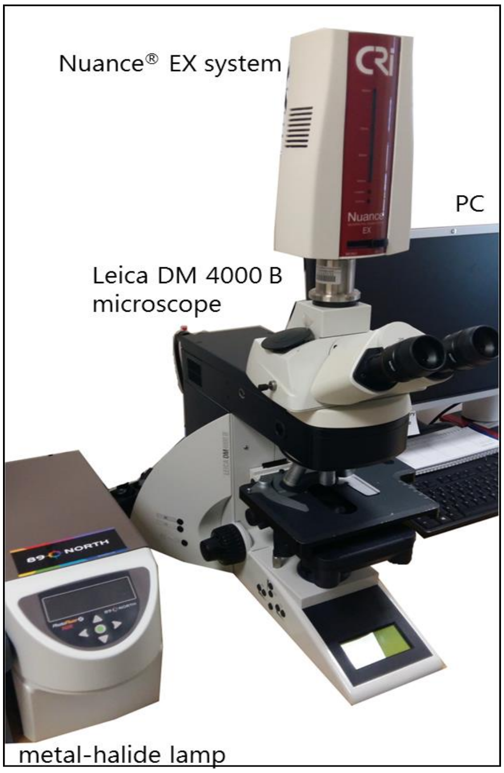

Fig. 9. Leica DM4000B transmitted-light microscope containing different excitation and emission filter sets combined with a Nuance® Ex multispectral imaging system containing a liquid crystal tunable filter and a CCD chip. On the left side the metal-halide lamps is displayed which represents the excitation light source. At the PC the data were evaluated by Nuance® Software.

This system allows the multispectral analysis of fixed tumor cells and tissue sections and enables the detection of several dyes or molecular markers simultaneously. Both the device setup and the software (Nuance® 3.0.2) are very similar to the Maestro™ system which was used for the msFI. For all experiments a fixed bit depth [12], camera gain [1] and binning [2x2] was used. As light source a 200 W self-aligning metal-halide lamp (PhotoFluor® II NIR; 360 – 800 nm) from 89 NORTH™ (U.S.A.) was used. Several filter sets containing each a narrow band excitation filter and a longpass emission filter were used for the microscopic examination depending on the used dye. They are summarized in Table 4. When the specimen was irradiated with the filtered excitation light, the emitted fluorescence light was filtered by the respective longpass emission filter.

Table 4. Applied filter sets for the Nuance® Ex multispectral imaging system

Filter Set	Excitation Filter	Emission Filter	Acquisition Settings
UV	340 – 380 nm	425 nm longpass	450 – 650 nm (10 nm steps)
Blue	450 – 490 nm	515 nm longpass	520 – 720 nm (10 nm steps)
Red	620 – 660 nm	665 nm longpass	670 – 850 nm (10 nm steps)
NIR	710 – 775 nm	780 nm longpass	785 – 950 nm (10 nm steps)

Afterwards, the light passed a software controlled liquid crystal tunable filter (LCTF) which allows the nm-precise scanning of the chosen wavelength range. The step-bandwidth was adjusted on 10 nm for all measurements. Next, the light was detected by a cooled (8 °C) 1.4 megapixel CCD camera. The software (Nuance® 3.0.2) was used to calculate a cube which consists of a series of images taken at specific wavelengths. It contains the complete spectral information for each pixel of the image. The resulting cubes had an image size of 696 x 520 pixels. For the cube acquisition automatic exposure tool was used to avoid over- or underexposure. The data evaluation and image processing by the Nuance® 3.0.2 software was done similar to the procedure of msFI data evaluation with the Maestro™ system described in chapter 2.2.2.2. However, the autofluorescence signal for the preparation of a spectral library here was obtained by extracting the signal from the respective untreated (no staining was applied), fixed cancer cell line. For the observation of fixed tumor cells, the respective cells were seeded and cultivated in chamberslides. Within the chambers, they were incubated with the agent of interest for a certain period of time. Afterwards, the supernatant and the chambers were removed and the cells remained on the microscopic slide. Thereby, they could be examined by fluorescence microscopy. For fluorescence microscopic examination of tumor tissue, the tumors were necropsied, formalin fixed, paraffin embedded, sliced and embedded in mounting medium (Dako® Fluorescence Mounting Medium, Agilent Technologies, U.S.A) on a microscopic slide.

Besides the treatment with the fluorescent labeled pHPMA conjugates, cells and tumor tissue sections were stained with different dyes to visualize certain cellular compartments. The DNA-binding dye 4',6-diamidino-2-phenylindole (DAPI; Ex: 358 nm/Em: 461 nm; Sigma-Aldrich

Chemie GmbH) was used to stain the cell nuclei, while the F-actin binding agent Alexa Fluor® 488 Phalloidin (Ex: 495 nm/Em: 518 nm; Thermo Fisher Scientific Inc., U.S.A.) was used to stain the actin cytoskeleton of the cells. For the staining process, cells were fixed with 4 % formalin, washed with PBS, permeabilized with a 0.1 % solution of Triton X-100 in PBS, washed again with PBS and subsequently stained with the respective dye. Microscopic images of DAPI or Alexa Fluor® 488 Phalloidin stained 1411HP cells are shown in Fig. 10.

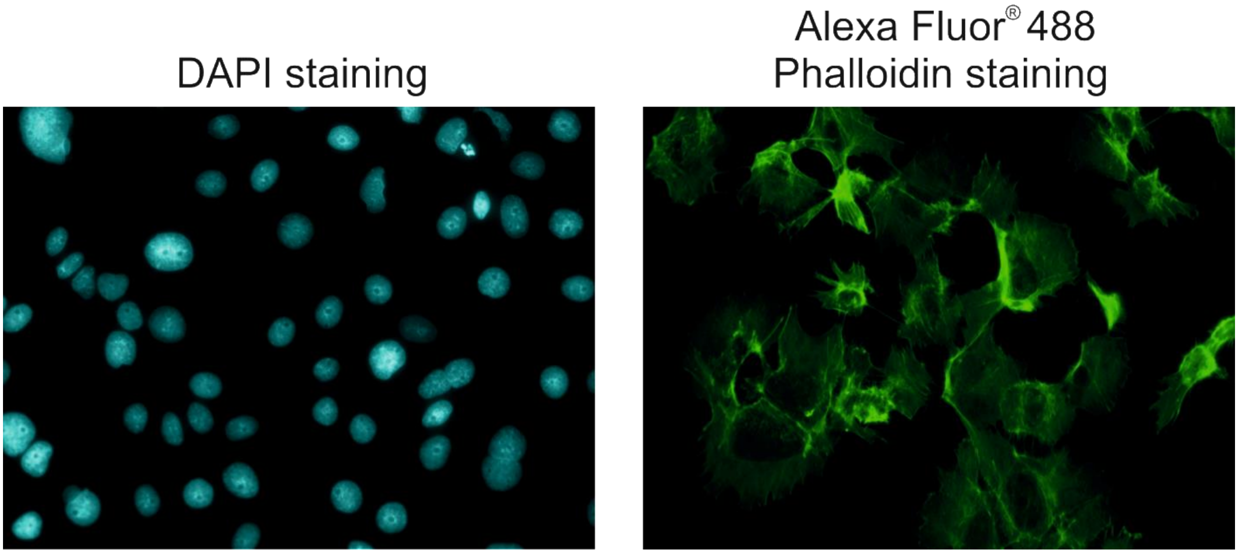

Fig. 10. Formalin fixed 1411HP cells after staining with DAPI (left) to visualize the cell nuclei or with Alexa Fluor® 488 Phalloidin (right) to visualize the actin cytoskeleton.

3. Results and Discussion

3.1 Comparison of different stimulus-sensitive drug delivery systems

It is widely known that a site specific drug release can result in higher drug concentrations exclusively in tumor tissue and thereby reduce toxic side effects. By the use of a specific linker between drug and carrier system, the drug release can be triggered by different stimuli like temperature, redox status, pH or enzymes (20, 55, 56). In this thesis, the stimuli redox status, lysosomal enzymes and pH were taken into consideration. A disulfide bond was used to link a drug model to the polymer carrier enabling a reduction sensitive tumor site specific drug release. An enzymatically triggered drug release was investigated by the use of an enzymatically cleavable tetrapeptide spacer Gly-Phe-Leu-Gly (GFLG) acting as a linker for the drug model. The linkage of a drug model via a pH-sensitive cleavable hydrazone bond to the polymer carrier represented a system for the pH-triggered drug release. In the following sections the results of the experiments with the respective linker will be presented and discussed.

3.1.1 HPMA copolymers with reduction-sensitive drug release[1]

First, the *in vivo* fate of N-(2-hydroxypropyl)methacrylamide-based copolymer (pHPMA) conjugates containing a drug model bound via a disulfide bond, which is frequently cited (57, 58) in the literature as being stable in the bloodstream but readily cleavable after cell internalization, was investigated. The underlying condition for the site specific drug release was the assumed higher intracellular reduction capacity compared to the extracellular milieu, which is much more pronounced in tumor tissue due to a lack of oxygen, at least in sparsely vascularized tumors. Amongst others, the glutathione pathway has a significant influence on redox state of the cells and the respective enzymes are very likely involved in the reductive cleavage of the disulfide bond. Here, the concept was based on the dual labeling of HPMA copolymers with two different fluorescent dyes. One dye (DY-676) was linked via disulfide bond to the polymer backbone, thereby representing a drug model mimicking the reductively releasable drug. The second dye (DY-782) was covalently attached as a non-cleavable amide and served as a label for the polymer carrier. Simultaneous tracking of both the polymer carrier and the drug model by msFI was then possible. The schematic structure of the double labeled pHPMA conjugate with reduction sensitive drug release is displayed in Fig. 11.

---

[1] These results have been published:
Studenovsky M, Heinrich A-K, Lucas H, Mueller T, Mäder K, Etrych T. Dual fluorescent N-(2-hydroxypropyl) methacrylamide-based conjugates for passive tumor targeting with reduction-sensitive drug release: Proof of the concept, tumor accumulation, and biodistribution. Journal of Bioactive and Compatible Polymers 2016; 31(4):348–60.

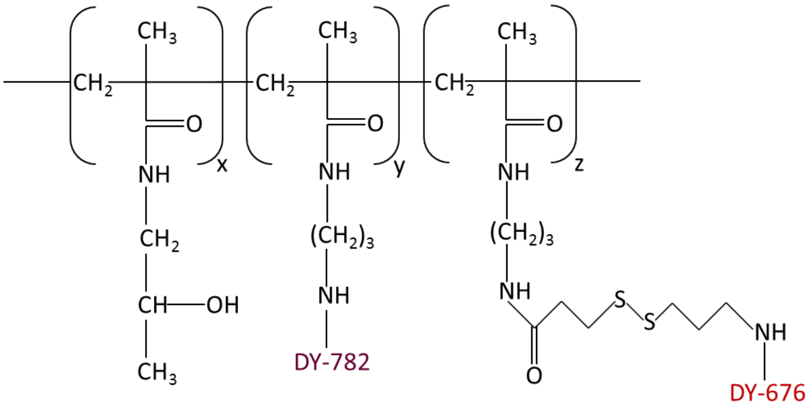

Fig. 11. Schematic structure of the double labeled pHPMA conjugate with reduction sensitive drug release. The covalently linked dye DY-782 served as a polymer label whereas DY-676, linked via disulfide bond to the polymer backbone, served as a drug model which is releasable under reductive conditions.

As the far-red dye DY-676 and the NIR dye DY-782 are well detectable even in deep tissues due to their spectral properties the biodistribution in mice could be entirely monitored over time. Two conjugates, differing in their M_w (30 and 104 kDa), were investigated in HT-29 and DLD-1 human colon carcinoma xenograft-bearing athymic nude mice. Additionally, necropsied organs and tumors were examined *ex vivo* by msFI to obtain more detailed information about polymer and drug model biodistribution. Thereby, the suitability of the disulfide bond as a potential linker for the achievement of tumor site specific reduction-sensitive drug release from HPMA copolymers was determined.

3.1.1.1 Investigation of the biodistribution and tumor accumulation by multispectral fluorescence imaging

For determining the biodistribution of the polymer conjugates and the release of the drug model, DLD-1 and HT-29 human colon carcinoma xenograft-bearing athymic nude mice were treated with an i.v. injection of either the linear 30 kDa (**R***L*30) or the linear 104 kDa (**R***L*104) pHPMA conjugate. Usually, the pHPMA conjugates with a higher M_w are designed with branched, dendritic or star-like architecture but in case of the reduction sensitive linker only the design of a linear high M_w conjugate was possible due to the chemical properties of the used disulfide bond. After administration of the respective conjugate, the mice were observed by msFI immediately and also 1, 24, 48 and 72 h after i.v. injection. The distribution and tumor accumulation of the linear HPMA copolymers exhibiting different molecular weights could be observed by the fluorescence signal of DY-782 which was covalently linked to the polymer backbone, whereas the drug model was detectable via the fluorescence signal of the reductively cleavable drug model DY-676.

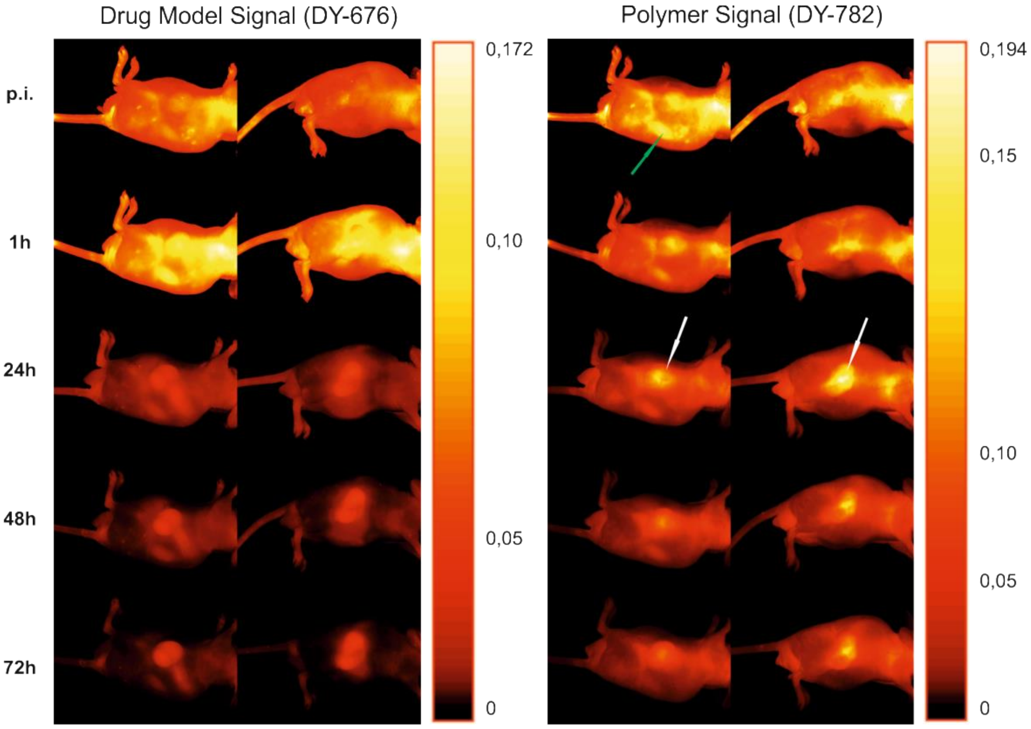

Fig. 12. Polymer and drug model distribution after i.v. injection of conjugate **R***L*30 (left side of mice - HT-29 tumor, right side - DLD-1 tumor: white arrows). Green arrow: kidneys. Drug model signal increased up to 1 h post injection. Afterwards the intensity decreased while the signal was more and more confined to the tumor region. In contrast the polymer signal increased up to 24 h. Although a good tumor accumulation was visible, the strong signal of the residual mouse indicated the enduring circulation of the polymer. The non-congruent distribution patterns indicated a successful tumor-site specific release of the drug model.

The disulfide bond is assumed to be stable during circulation in the bloodstream, thereby avoiding peripheral drug model release, but is rapidly cleavable under reductive conditions which are given predominantly in the tumor tissue. After the injection of the polymer conjugate solutions, the total fluorescence signals of both polymer and drug model increased up to 24 and 1 h, respectively. Afterwards, the signals were increasingly confined to the tumor region, indicating tumor-specific accumulation (Fig. 12) due to the EPR effect. Furthermore, it was observable that the drug model signal decreased much faster in the residual mouse body compared to the tumor region, suggesting a tumor site-specific accumulation and release of the drug model. This was much more pronounced after 48 and 72 h when the tumor region still exhibited a strong signal of the drug model while the residual mouse exhibited only low fluorescence intensity (Fig. 12, left). The polymer signal showed a different distribution pattern (Fig. 12, right). Although a quite good tumor accumulation was visible, the whole mouse still gave a strong signal after 72 h indicating the enduring circulation of the polymer. The different distribution patterns of both signals indicated a tumor site specific drug release, at least from the lower M_w conjugate.

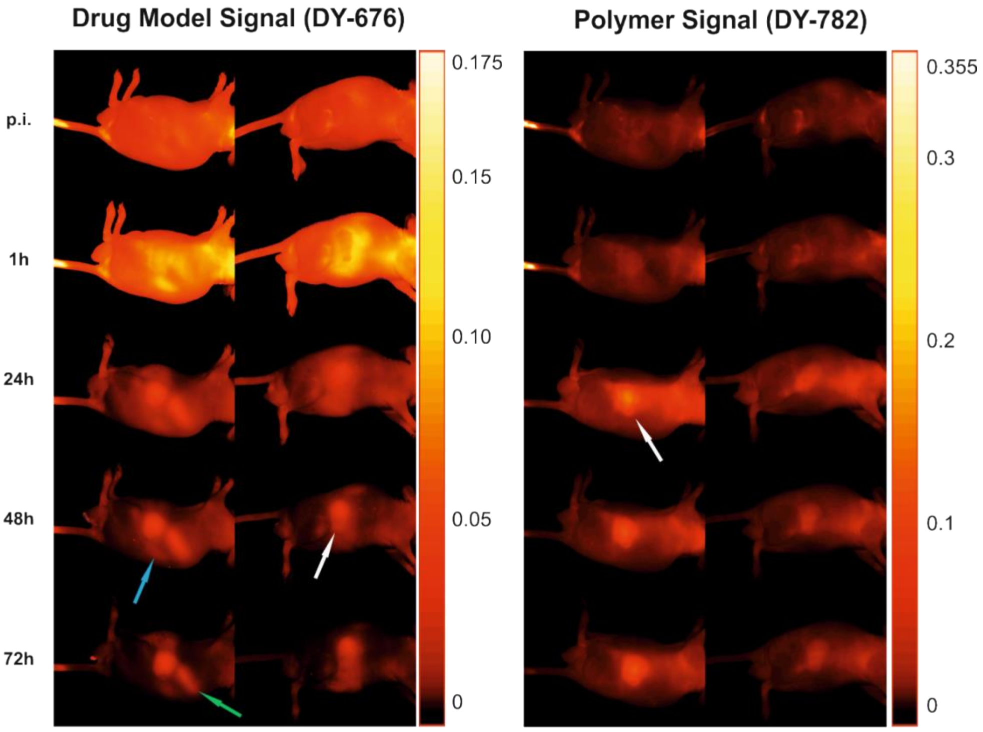

Fig. 13. Polymer and drug model distribution after i.v. injection of conjugate **R***L*104 (left side of mice - HT-29 tumor, right side - DLD-1 tumor: white arrows). Drug model signal increased up to 1 h post injection while the polymer signal increased up to 24 h. The comparable distribution patterns of drug model and polymer signal led to the assumption of an insufficient release of the drug model within the given time period. Nevertheless, it can be assumed that at least a small amount of the drug model has been released due to the detected signal in kidneys (blue arrow) and spleen (green arrow) independent from the polymer signal.

For the higher M_w conjugate **R***L*104, a more similar pattern for the polymer and the drug model signal was observable even after 72 h (Fig. 13). Therefore, it was assumed that the drug model release was insufficient within that time period. A polymer independent signal of the drug model was detected in spleen and kidneys which would indicate that at least a small amount of the drug model was released (Fig. 13). However, the missing polymer signal in kidneys and spleen must be considered critically as the strong fluorescence intensity of the whole mouse, due to elongated circulation time in case of the high M_w conjugate, could have covered the fluorescence signal of the organs.

A detailed analysis of tumor-specific accumulation was then performed by calculation of the tumor accumulation value (TAV), developed by Hoffmann *et al.* (45). The TAV expresses the ratio of the polymer-derived fluorescence signal (I_{tumor}) detected in the tumor region ($area_{tumor}$) to the polymer-derived signal (I_{mouse}) detected in the residual mouse body ($area_{mouse}$).

$$\mathrm{TAV} = \frac{I_{tumor} \times (area_{mouse} - area_{tumor})}{area_{tumor} \times (I_{mouse} - I_{tumor})}$$

The tumor region is thereby defined by drawing a region of interest (ROI) within a grayscale image around the tumor region, which is clearly visible because of the used subcutaneous tumor model. Therefore, the fluorescence intensity detected in the ROI can be clearly assigned to the tumor and is used for the TAV calculation. A TAV higher than 1 already indicates enhanced tumor accumulation. Fig. 14 shows the TAVs of 30 kDa and 104 kDa copolymers and the respective drug model in both xenograft types (DLD-1 and HT-29) over time. For both polymers, an increasing TAV up to 24 h after injection was observed in both xenograft types, which can be attributed to the EPR effect. After 24 h, no further increase in TAV was observed for the 30 kDa polymer. This might be caused on the one hand by an equilibration of polymer tumor accumulation and elimination and on the other hand by an equal decrease in fluorescence intensity in tumor tissue and residual mouse body, driven by the urine excretion of the polymer with a M_w under the limit of the renal threshold. In contrast, a slight but continuous increase in TAV of the 104 kDa polymer was observable. This was caused by the elongated circulation in the mouse body due to the higher M_w and thereby restricted renal elimination. In regard to the TAVs of the drug model, it was observable that they were continuously increasing, suggesting permanent release of the drug model in tumor tissue.

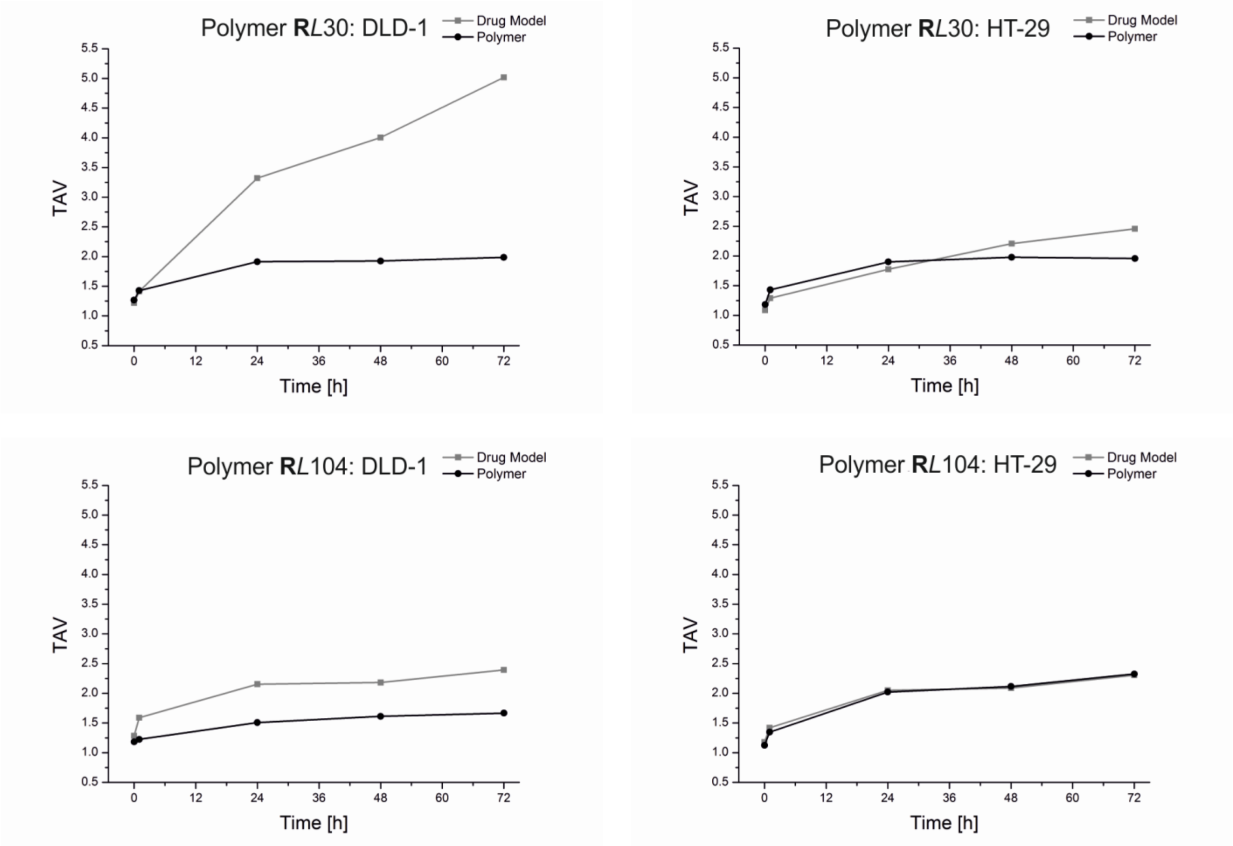

Fig. 14. Tumor accumulation values (TAVs) over time of **R***L*30 and **R***L*104 and TAVs of the drug model (DY-676) respectively in a DLD-1 and HT-29 xenograft tumor bearing mouse.

It was noticeable that this process occurred to a different extent depending on the polymer type as well as the xenograft type. For the 30 kDa copolymer, an increasing drug model TAV could be observed over the complete time course, whereas the corresponding polymer TAV showed a plateau after 24 h. This pattern was much more pronounced in the DLD-1 tumor compared to the HT-29 tumor. In contrast, the drug model TAV curve of the 104 kDa copolymer showed a similar slope as the polymer TAV curve, although it was shifted to higher values in the DLD-1 tumor. Based on these data, a higher site-specific reduction-sensitive drug release could be assumed for the 30 kDa copolymer. It is hypothesized that this phenomenon is associated with the complex system of the cellular redox state, which is a crucial mediator of multiple metabolic, signaling, and transcriptional processes in cells. The cellular redox state is mainly maintained by enzymes such as thioredoxins, glutaredoxins and thiol-disulfide oxidoreductases, which are also probably involved in the reduction of disulfide bonds between drug model and polymers. Recently, it was reported that enzymatic activity is strongly dependent on the molecular structure of the polymer conjugates and the accessibility of enzyme substrate for the lysosomal enzymes (59). It was shown that the steric hindrance increased with the M_w of the polymer conjugates. Thus, it can be assumed that steric hindrance led to an inhibition of the accessibility of thiol-disulfide oxidoreductases to the disulfide-containing substrate. This could explain the decreased rate of *in vivo* drug model release with increasing M_w of the used polymeric conjugate. Another aspect which should be considered is the restricted diffusion through the tumor tissue of the high M_w copolymer due to its increased size. It can be assumed that the smaller conjugate can diffuse much more easily, resulting in a more homogeneous distribution within the tumor tissue and thereby in a more efficient release of the drug model.

Regarding the different xenograft types, it was observable that the polymer accumulation of **R***L*30 was higher for the DLD-1 tumor, whereas **R***L*104 accumulation was higher in HT-29 which can be seen in the graph of **R***L*104 TAV (Fig. 14). This might be explained by different tumor sizes as the tumors were established simultaneously on the left and right side of the mice. However, the drug model release from both polymers was higher in DLD-1 tumors. This difference might be caused by the different substructure of both xenograft types. The higher growth rates of DLD-1 tumors compared to HT-29 are associated with the occurrence of large necrotic and fibrotic areas which might have led to a more hypoxic microenvironment, offering enhanced reductive conditions. This probably led to a more efficient release of the drug model. It can be concluded that the efficiency of the reduction-sensitive drug release is strongly dependent on the tumor type and its microenvironment. Nevertheless, drug release was observable in both tumor types, although to a different extend.

To gather more information about biodistribution and tumor accumulation of the polymer and drug model, necropsied organs and tumors were examined via *ex vivo* fluorescence imaging. Both polymer types showed nearly similar organ distribution patterns but the tumor-associated drug model signals were more intensive in the case of the 30 kDa polymer. Fig. 15 shows the distinct patterns of polymer and drug model distribution of both polymers. A high fluorescence intensity of the 30 kDa polymer (Fig. 15, top, DY-782) was detectable in both tumors, in the kidneys and, to a lesser extent, in the liver. As the 30 kDa copolymer underlies renal excretion the strong kidney signal could be explained.

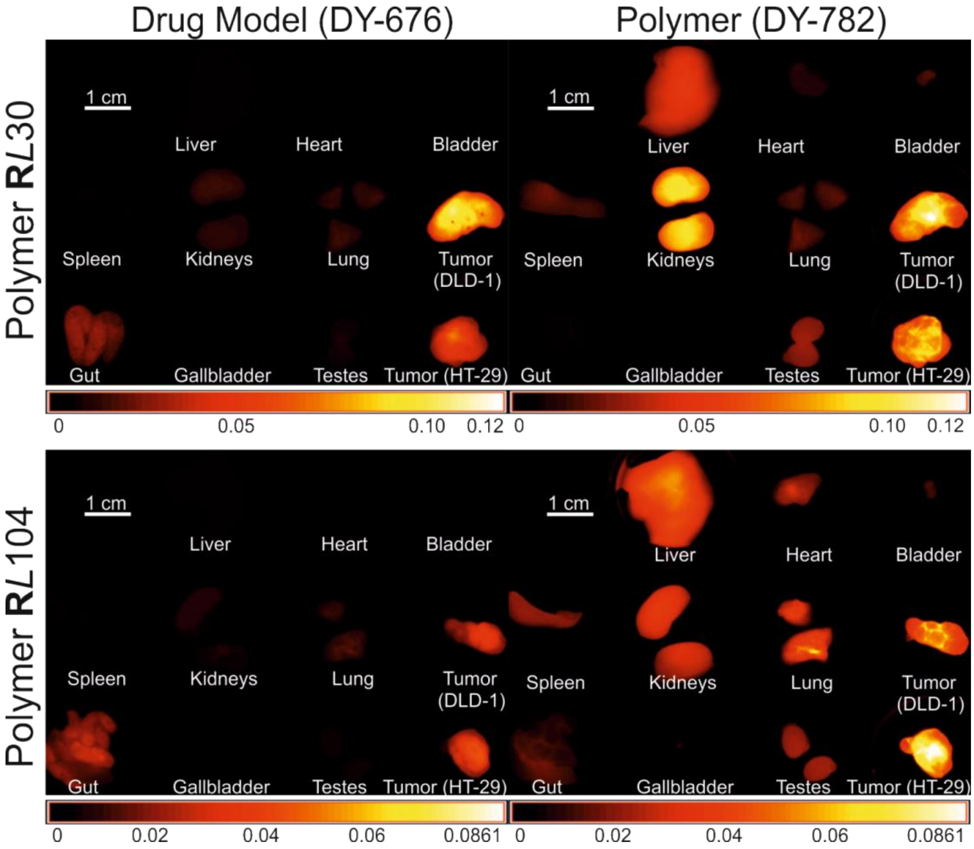
Drug Model (DY-676)
Polymer (DY-782)
Polymer **R***L*30
Polymer **R***L*104
1 cm
Liver
Heart
Bladder
Spleen
Kidneys
Lung
Tumor (DLD-1)
Gut
Gallbladder
Testes
Tumor (HT-29)
0
0.05
0.10
0.12
0.02
0.04
0.06
0.0861

Fig. 15. Fluorescence images of organs and tumors excised from 2 mice 72 h after treatment with either **R***L*30 or **R***L*104. Polymer (DY-782) and drug model (DY-676) signals are displayed to visualize their different distribution.

The kidney accumulation of HPMA copolymers has already been described (45, 60) including the higher M_w HPMA copolymers such as the 104 kDa polymer used in this study. In the case of the high M_w copolymers, no signal in the bladders of mice was detectable. A specific interaction between the polymer and kidneys could be assumed and has already been discussed in previous studies (45). Despite kidney accumulation, no acute nephrotoxic effects were observed within this time period. Furthermore, no noticeable drug model release in the kidneys was observable (Fig. 15, top, DY-676). Therefore, no acute nephrotoxic effects will be expected, even if the drug model will be replaced by a cytotoxic drug. Nevertheless, only histological examination and determination of the glomerular filtration rate (GFR) would allow reliable statements. The fluorescence signal in the liver resulted most likely from the circulating polymer carrier, which strongly influences the pattern of the highly blood-perfused liver. Regarding the drug model signal (Fig. 15, top, DY-676), which almost exclusively was detected in both tumors, a site-specific drug release could be proved.

The distribution pattern of the 104 kDa polymer (Fig. 15, bottom, DY-782) was very similar to the 30 kDa polymer, but higher fluorescence intensity was measured in HT-29 tumor compared to DLD-1 tumor, which was already expected due to the results determined by TAV calculation. Furthermore, a higher polymer-derived fluorescence signal was detected in the liver, lungs, heart, and spleen. It can be assumed that the prolonged body circulation of the 104 kDa polymer, which was also indicated by the continuously increasing TAV observed for this conjugate (Fig. 14), caused the higher signals from all organs with high perfusion. Additionally, the reticuloendothelial system (RES) could have been stimulated by an increased M_w and a bigger R_H. This would also explain the increased fluorescence intensity detected in liver and spleen and should not be neglected when evaluating the optimal M_w of the conjugates for further studies. The drug model was observed exclusively in the tumors. However, a much lower overall fluorescence intensity of the drug model was detectable in case of the **R***L*104. This indicated a lower release and accumulation of the drug model in both tumors compared to the **R***L*30. Although enzymes are not imperatively necessary for the reductive cleavage of the disulfide bond, a lower enzymatically driven reduction in the case of the more complex structure of the 104 kDa polymer is very likely the reason for the lower drug model release.

Detailed analyses of the tumors are shown in Fig. 16, where composite images of the excised and cross-sectioned tumors 72 h after the treatment with either conjugate **R***L*30 or **R***L*104 are displayed. The green color shows the polymer signal (DY-782), red color shows the drug model signal (DY-676) and the yellow areas indicate an overlay of both signals. As already expected from *in vivo* and *ex vivo* results, a much more pronounced clear drug model signal could be observed for the **R***L*30 compared to the **R***L*104. In the **R***L*104 group, the DLD-1 tumor showed higher drug model accumulation than HT-29, although the polymer accumulation was higher for the HT-29. This indicated the increased reduction sensitive drug model release in the DLD-1 tumor xenograft. These results support the assumptions made by TAV calculation and *ex vivo* imaging.

Taking everything into account, it can be concluded, that the usage of a disulfide bond, as a potential linker for chemotherapeutic drugs to the pHPMA backbone, represents a promising system to achieve a tumor site-specific drug release. Moreover, the M_w as well as the chosen tumor model play an important role regarding a sufficient, enzymatically triggered drug release.

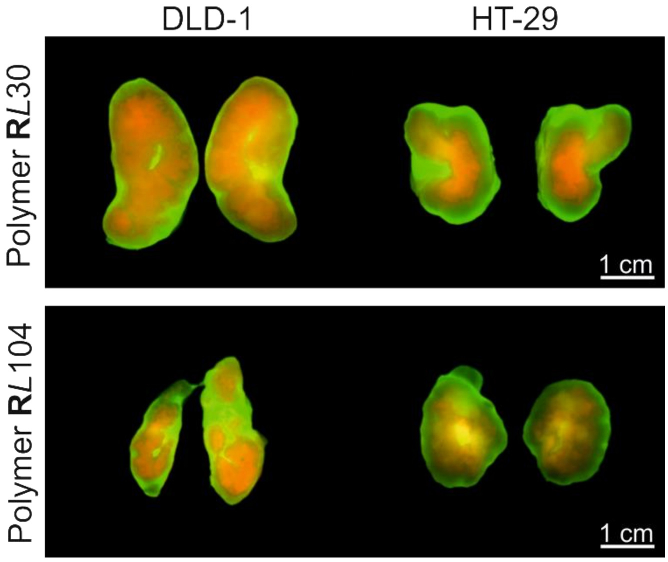

Fig. 16. Composite images of excised and cross-sectioned DLD-1 and HT-29 tumors 72 h after treatment with either **R***L*30 or **R***L*104. Polymer (DY-782): green; Drug model (DY-676): red; merge: yellow. Green and red signals indicated a successful release of the drug model within the tumor.

3.1.1.2 Summary

In this study, the use of a disulfide linker for the construction of polymer-drug conjugates for specific cancer therapy was examined. For this purpose, two double labeled HPMA-based copolymers, differing in their M_w, were designed and tested in DLD-1 and HT-29 tumor-bearing mice using msFI. Two different fluorescent labels were used. One was attached to the polymer via a non-degradable amide bond and the other via a reductively cleavable disulfide linker. Both *in vivo* and *ex vivo* experiments showed strong fluorescence signals in tumors due to accumulation of the carriers. The time-dependent distribution patterns of the polymer carriers significantly differed from those of the drug models. Evaluation of the TAVs of both polymer carriers and drug models indicated a tumor-site specific drug release that was much more pronounced for the 30 kDa conjugate and furthermore more efficient in the DLD-1 xenograft model. This observation was also supported by the images obtained from necropsied organs 72 h after treatment, where the drug model was detectable almost exclusively in tumors and the distribution patterns of the drug model and polymer label were completely different, demonstrating reductive release of the drug model. On the basis of these findings, the disulfide bond was shown to be specifically cleaved inside the tumors and can thus serve as a suitable linker between the drug and polymer in conjugates for cancer therapy. Therefore, further studies where the drug model should be replaced by a real chemotherapeutic drug are needed to prove the concept and to determine the efficacy compared to the respective unbound drug.

3.1.2 HPMA copolymers with enzymatic drug release[2]

Now, a second stimulus-sensitive linker was tested to determine its suitability for a site-specific drug release. HPMA copolymers were double labeled with the two fluorescent dyes DY-676 acting as a drug model and DY-782 as a covalently linked polymer label. This time, the drug model was attached to the polymer backbone via an enzymatically cleavable tetrapeptide spacer Gly-Phe-Leu-Gly (GFLG). After cell internalization this bond is expected to be cleaved by lysosomal proteases such as Cathepsin B. As the most malignant tumors exhibit increased Cathepsin B activity (61), a tumor-site specific drug release can be achieved.

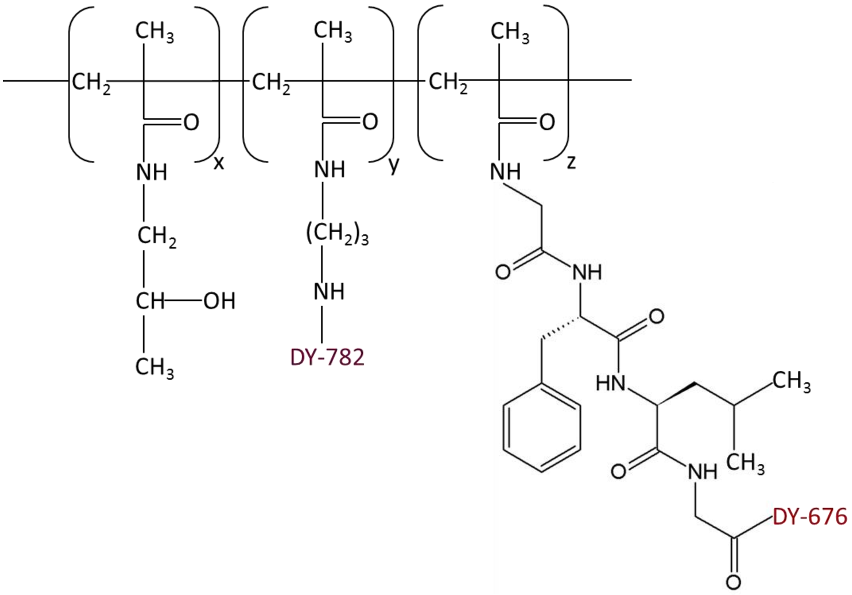

Fig. 17. Schematic structure of the linear, double labeled pHPMA conjugate with enzymatic drug release. The covalently linked dye DY-782 served as a polymer label whereas DY-676, linked via an enzymatically cleavable tetrapeptide spacer Gly-Phe-Leu-Gly (GFLG) to the polymer backbone, served as a drug model.

---

[2] These results have been published:
Pola R, Heinrich A-K, Mueller T, Kostka L, Mäder K, Pechar M *et al.* Passive Tumor Targeting of Polymer Therapeutics: *In Vivo* Imaging of Both the Polymer Carrier and the Enzymatically Cleavable Drug Model. Macromolecular bioscience 2016; 16(11):1577–82.

Here, also the dual fluorescent labeling of the conjugates allowed the *in vivo* monitoring of the biodistribution of both the drug model and the polymer by msFI. The schematic structure of the linear, double labeled pHPMA conjugate is displayed in Fig. 17. Two conjugates, differing in their architecture and M_w, were investigated in HT-29 and DLD-1 human colon carcinoma xenograft-bearing athymic nude mice: a linear HPMA copolymer conjugate exhibiting a M_w about 35 kDa (**E***L*35) and a dendritic conjugate with M_w about 170 kDa (**E***D*170).

Necropsied organs and tumors were examined by *ex vivo* msFI to obtain more detailed information about polymer and drug model biodistribution. Thereby, the suitability of the GFLG spacer as a potential linker for the achievement of tumor site specific enzymatic drug release from HPMA copolymers was determined.

3.1.2.1 Investigation of the biodistribution and tumor accumulation by multispectral fluorescence imaging

The determination of the biodistribution of the polymer conjugates and the release of the drug model was performed in DLD-1 and HT-29 human colon carcinoma xenograft-bearing athymic nude mice. They were treated with an i.v. injection of the respective polymer and were observed by msFI immediately and also 1, 24, 48 and 72 h after the injection. Afterwards, the distribution patterns of the drug model and polymer signal were compared. It was observable that both signals were initially congruent (Fig. 18). While the distribution over the whole mouse body indicated the expected circulation of the conjugates after i.v. injection, the signal detected in kidneys and bladder in case of the linear **E***L*35 arose from renal elimination. As the renal elimination of the **E***D*170 conjugate was restricted, no signal in bladder and only a faint signal in the kidneys was observable. 24 h after the injection, a clear EPR-effect mediated tumor accumulation was visible for both polymer and drug model which was in accordance to previous studies with the reduction-sensitive pHPMA conjugate. In case of **E***L*35, it was observable that the signal of the drug model was strongly confined to the tumor region. This effect was much more pronounced after 72 h. Regarding the polymer signal, it was observable that after 72 h the whole mouse still showed an intense fluorescence signal despite good tumor accumulation, indicating the enduring circulation and elimination of the polymer.

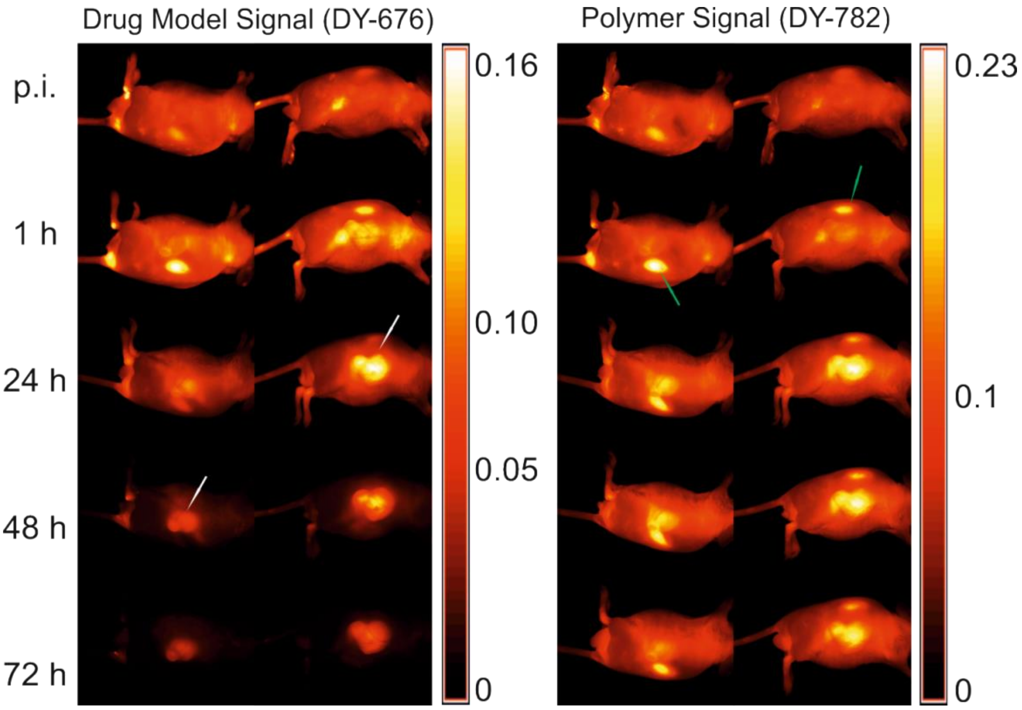

Fig. 18. Polymer and drug model distribution after i.v. injection of the **E***L*35 conjugate (left side of mice - HT-29 tumor, right side - DLD-1 tumor: white arrows). Green arrows: kidneys. Drug model signal increased up to 24 h post injection. Afterwards, the intensity decreased while the signal was more and more confined to the tumor region. The polymer signal also increased up to 24 h. Although a good tumor accumulation was visible, the strong signal of the residual mouse indicated the enduring circulation of the polymer. The non-congruent distribution patterns indicated a successful tumor-site specific release of the drug model.

A tumor-site specific drug model release was shown, as the signals of polymer and drug model were no longer congruent (Fig. 18).

Considering the fluorescence images of **E***D*170, another distribution pattern became apparent. Indeed, a clear tumor accumulation of the polymer and the drug model was observable but both signals were nearly congruent even after 72 h (Fig. 19). This indicated a lack of drug model release and was comparable to the results of the conjugate **R***L*104.

Further evaluation of the fluorescence images allowed the calculation of the TAV as already described in section 3.1.1.1. For both conjugates, the pattern of the polymer TAV curves was similar (Fig. 20). After an initial increase of the TAV up to 24 h the curve reached a plateau.

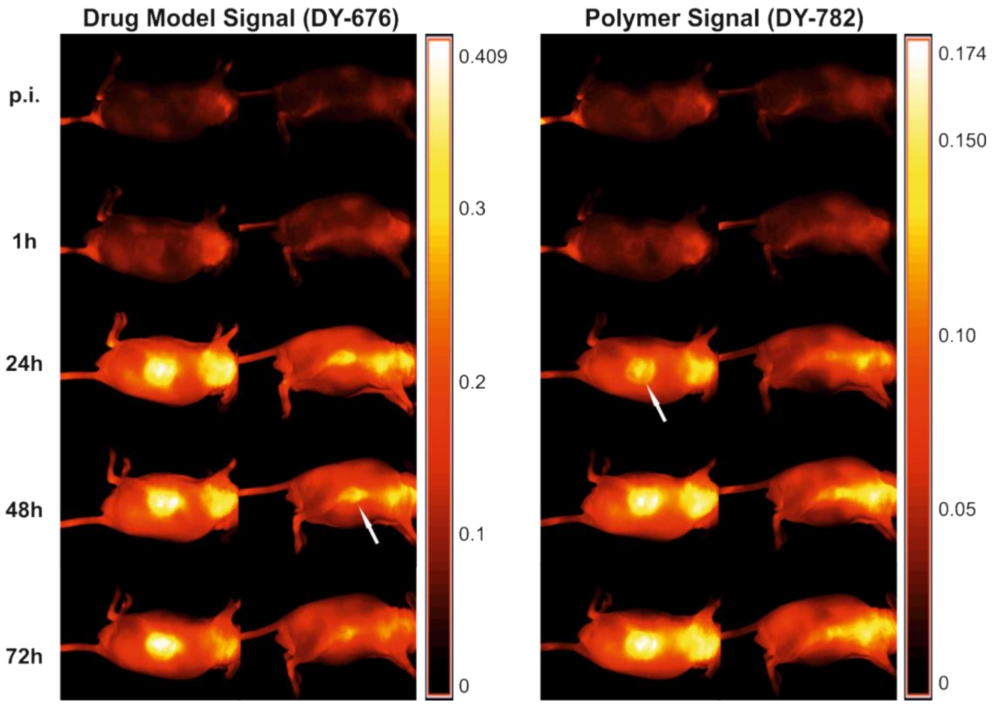

Fig. 19. Polymer and drug model distribution after i.v. injection of conjugate **E***D*170 (left side of mice - HT-29 tumor, right side - DLD-1 tumor: white arrows). Drug model signal increased up to 24 h post injection while the polymer signal increased up to 48 h. The similar distribution patterns indicated an insufficient release of the drug model.

The equal decrease of fluorescence intensity in the tumor region and the whole mouse body, as well as a balance of transport to and elimination out of the tumor, very likely led again to the constant TAV. This was quite contrary to the drug model TAV in case of the **E***L*35 conjugate. Here, the TAV increased continuously up to comparatively high values, supporting the assumption of an effective tumor-site restricted release of the drug model. The remarkable higher TAV of the drug model of the low M_w conjugate in the DLD-1 tumor probably arose from the bigger tumor volume, which led to enhanced EPR-effect mediated accumulation of the whole conjugate. In contrast to conjugate **E***L*35, the drug model TAV curves of conjugate **E***D*170 had a similar pattern as the respective polymer TAV curves. This was comparable to the results gathered from the study with the reduction-sensitive pHPMA conjugate and corroborated the assumption of lacking release of the drug model.

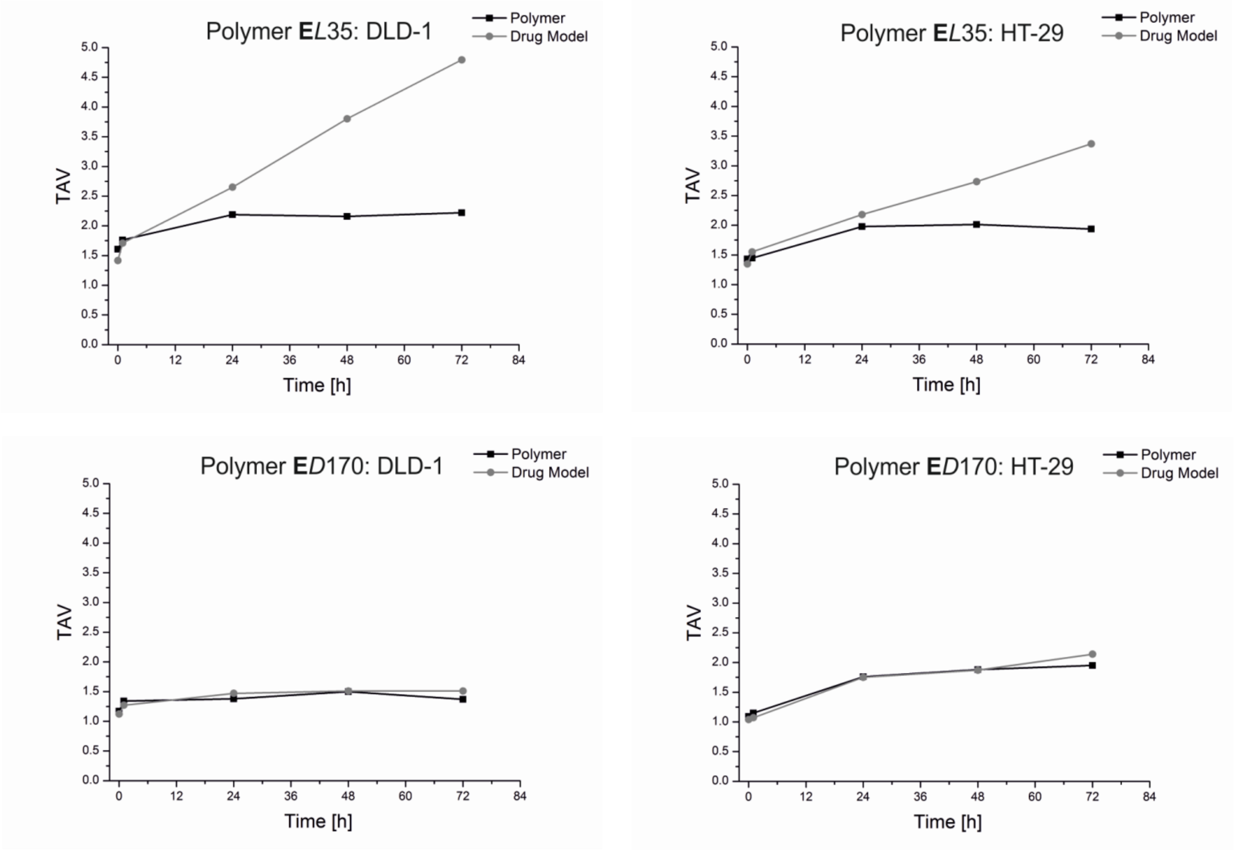

Fig. 20. TAVs over time of **E***L*35 and **E***D*170 release and TAVs of the drug model (DY-676) respectively in one DLD-1 and HT-29 xenograft tumor bearing mouse.

To gather further information about the distribution of polymers and drug model, the necropsied organs and tumors were examined 72 h after the injection by *ex vivo* msFI. The strong polymer derived signal detected in the kidneys (Fig. 21, right) indicated again the renal clearance of the **E***L*35 conjugate. A fluorescence signal was further detected to a lesser extend in tumors and liver, which was already expected after evaluation of the *in vivo* fluorescence images. The drug model signal (Fig. 21, left) was predominantly detectable in both tumors. Thereby, a selective drug model release and accumulation at the tumor site was confirmed. The drug model was also detectable in liver, gallbladder and gut, as a result of the hepatobiliary elimination of the cleaved dye (DY-676). Overall, a tumor site specific drug release of **E***L*35, which was already assumed by evaluation of the *in vivo* images, was confirmed *ex vivo*.

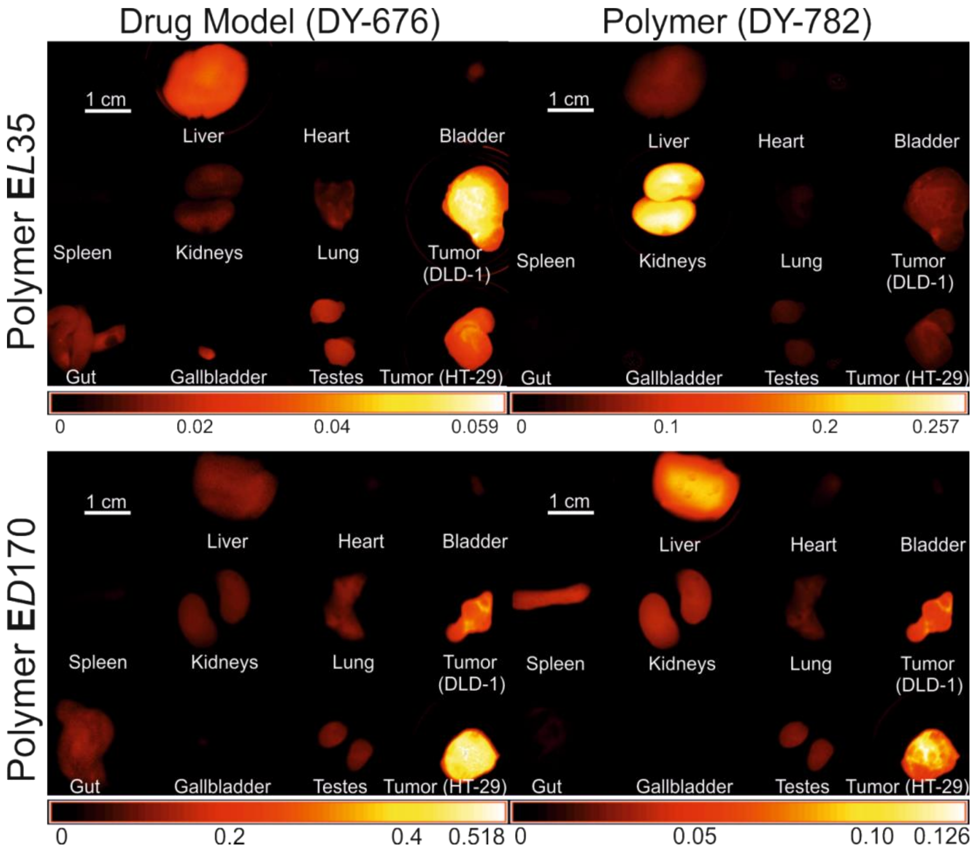
Drug Model (DY-676)
Polymer (DY-782)
Polymer **E***L*35
Polymer **E***D*170
1 cm
Liver
Heart
Bladder
Spleen
Kidneys
Lung
Tumor (DLD-1)
Gut
Gallbladder
Testes
Tumor (HT-29)
0
0.02
0.04
0.059
0
0.1
0.2
0.257
0
0.2
0.4
0.518
0
0.05
0.10
0.126

Fig. 21. Fluorescence images of organs and tumors excised from 2 mice 72 h after treatment with either **E***L*35 or **E***D*170. Polymer (DY-782) and drug model (DY-676) signals are displayed to visualize their different distribution.

Regarding the *ex vivo* imaging results of the necropsied tumors and organs after administration of the **E***D*170 conjugate, it was observable that drug model and polymer signal showed a similar distribution pattern again. This was comparable to the *in vivo* results and confirmed the assumption of insufficient cleavage of the stimulus-sensitive linkage.

The necropsied tumors were cross-sectioned and individually examined by msFI. The simultaneous detection of drug model and polymer signal allowed the creation of a composite image, displaying both signals side by side (Fig. 22). Green color indicated the polymer derived signal, whereas red indicated the drug model signal. Therefore, yellow displayed an overlay of both signals. Observing green and red signals would indicate a successful release of the drug model.

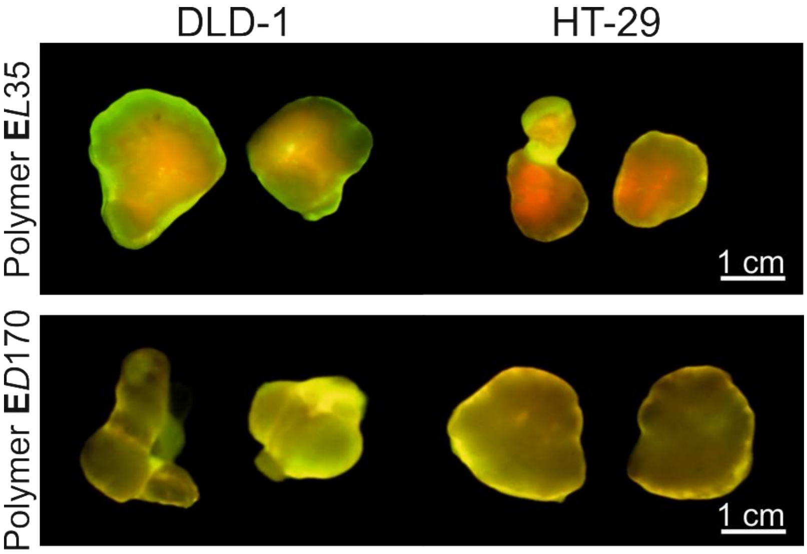

Fig. 22. Composite image of excised and cross-sectioned DLD-1 and HT-29 tumors 72 h after treatment with either **E***L*35 or **E***D*170. Polymer (DY-782): green; drug model (DY-676): red; merge: yellow. Green and red signals indicated a successful release of the drug model within the tumor.

Comparing the necropsied and cross-sectioned tumors of conjugate **E***L*35 and **E***D*170 groups, only in the tumors of **E***L*35 green and red signals were detectable. This corroborated the *in vivo* findings and the results of *ex vivo* organ examination. Comparable to the discussed phenomenon of steric hindrance in case of the **R***L*104 conjugate, the hampered drug model release of higher M_w pHPMA conjugates with enzymatic drug release was also assumed to be a result of steric hindrance. The increased M_w and thereby also increased R_H restricted very likely the accessibility of the respective proteases to the substrate. Furthermore, the restricted diffusion through the tumor tissue might be responsible for the lower drug model release, as it was already assumed for the reduction-sensitive pHPMA conjugate. It can be concluded, that the **E***L*35 conjugate will be more advantageous for further studies.

As msFI is a suitable method for long-term observations, additionally a long-term experiment was performed, to determine the *in vivo* behavior of both pHPMA conjugates with enzymatic drug model release. The experiment was conducted similar to the short term study. This time the mice were observed by msFI immediately and also 1, 24, 48, 72, 144, 192, 240 and 312 h after the i.v. injection of the respective polymer. Again, the distribution patterns of drug model and polymer were compared. In case of the lower M_w conjugate **E***L*35, it was shown that an observation for this long time period is not reasonable, as the fluorescence intensity of the drug model and polymer strongly decreased after 72 h due to renal elimination (Fig. 23).

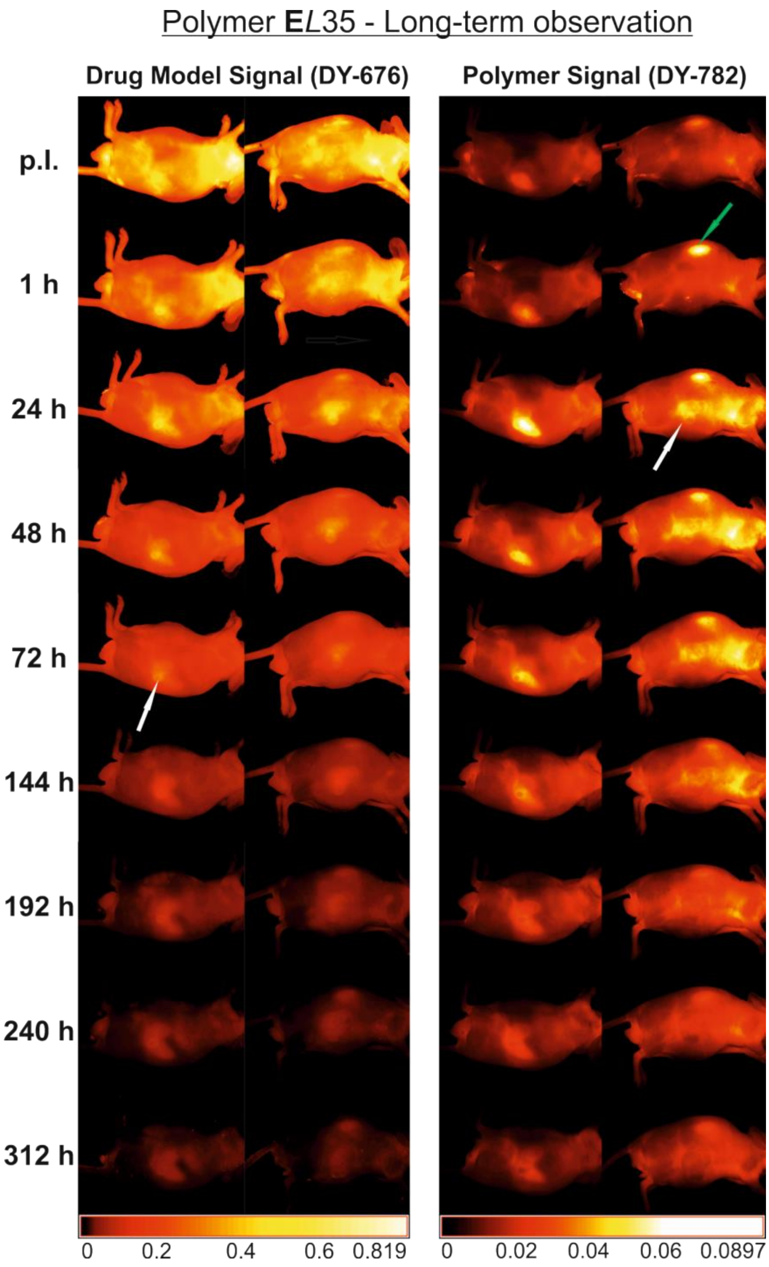
Polymer **E***L*35 - Long-term observation
Drug Model Signal (DY-676)
Polymer Signal (DY-782)
p.I.
1 h
24 h
48 h
72 h
144 h
192 h
240 h
312 h
0
0.2
0.4
0.6
0.819
0
0.02
0.04
0.06
0.0897

Fig. 23. Polymer and drug model distribution after i.v. injection of conjugate **E***L*35 (left side of mice - HT-29 tumor, right side - DLD-1 tumor: white arrows). Drug model signal increased up to 24 h post injection and the signal was mainly confined to the tumor region. Afterwards the intensity decreased quickly. The polymer signal increased up to 48 h and showed good tumor accumulation. The fluorescence intensity decreased afterwards due to the renal elimination of the conjugate which is also indicated by the strong fluorescence signal detected in the kidneys (green arrow).

In case of the high M_w conjugate **E***D*170, the long-term observation revealed interesting data. 144 h after injection the distribution patterns of drug model and polymer started to be less congruent and the drug model signal was strictly confined to the tumor region (Fig. 24).

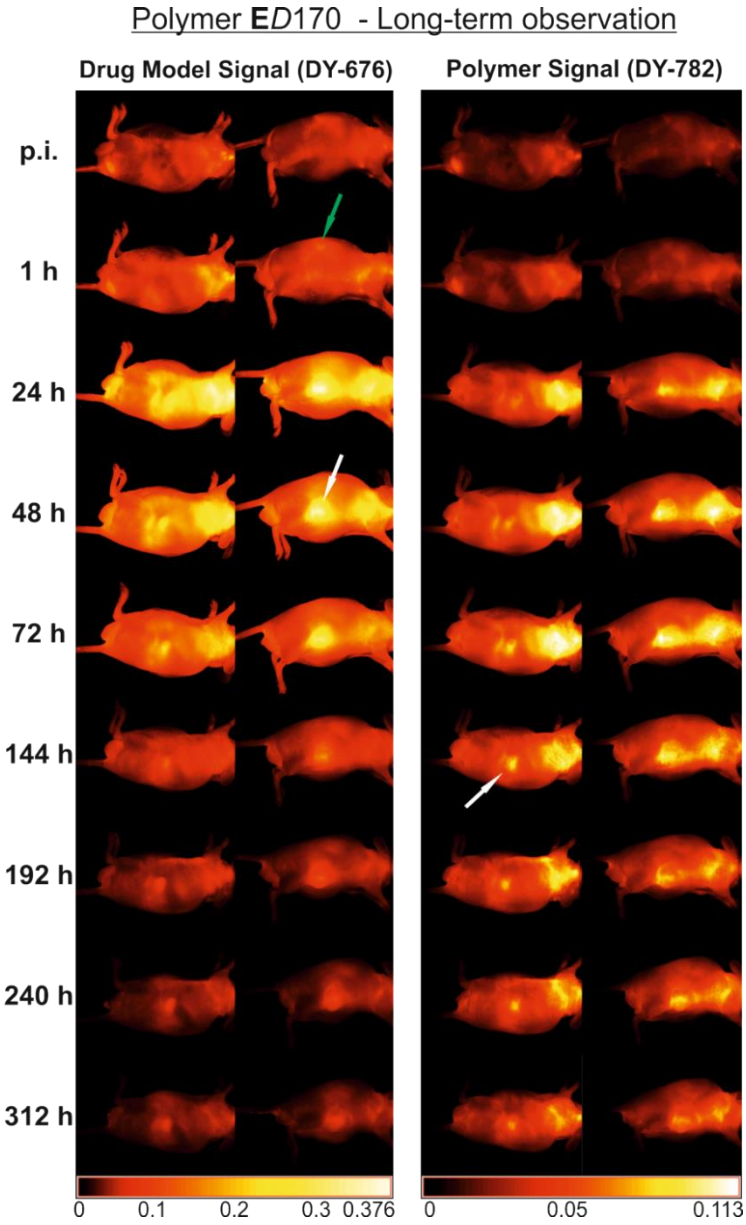
Polymer **E***D*170 - Long-term observation
Drug Model Signal (DY-676)
Polymer Signal (DY-782)
p.i.
1 h
24 h
48 h
72 h
144 h
192 h
240 h
312 h
0
0.1
0.2
0.3
0.376
0
0.05
0.113

Fig. 24. Polymer and drug model distribution after i.v. injection of conjugate **E***D*170 (left side of mice - HT-29 tumor, right side - DLD-1 tumor, white arrows: tumors). Green arrow: kidneys. Drug model signal increased up to 24 h post injection. Afterwards the intensity decreased but the signal was more and more confined to the tumor region. The polymer signal increased up to 72 h. Although a good tumor accumulation was visible, the strong signal of the residual mouse indicated the enduring circulation of the polymer. The distribution patterns of drug model and polymer started to be less congruent after 144 h. This indicated a delayed but existent tumor-site specific release of the drug model.

The overall intensity of the drug model signal decreased quickly after 144 h, whereas the fluorescence intensity of the polymer remained nearly constant. This indicated the enduring circulation of the polymer but stepwise renal elimination of the released low M_w drug model (Fig. 24). Taking these results into account, it can be anticipated that a tumor-site specific drug model release from the high M_w conjugate happened after this longer time period. Unfortunately, the results of the performed TAV calculation were not convincing (Fig. 25). The drug model TAV of conjugate **E***D*170 was increasing up to 144 h in the DLD-1 xenograft and was at least slightly higher than the respective polymer TAV. The decreasing TAVs for the drug model after 144 h arose from renal elimination of the released low M_w drug model. The data for the HT-29 xenograft are only displayed for the sake of completeness, as they must be considered critically due to a very small tumor size. As the HT-29 tumor xenografts are growing much slower compared to the DLD-1 tumor xenografts, the establishment of these two tumor models in one mouse simultaneously can be difficult. The respective mice were s.c. inoculated with the HT-29 tumor cell suspension already one week before they received the s.c. DLD-1 tumor cell injection. Normally, thereby comparable tumor sizes of the HT-29 and DLD-1 tumors in one mouse were achieved. Unfortunately, in this case the HT-29 tumor was very slow-growing and did not reach the size of the DLD-1 tumor within this time period. Although it is known from histological examinations that the typical tumor substructure of HT-29 tumors is already distinct in such small tumor xenografts, a reliable comparison of the fluorescence intensities was not possible.

In case of conjugate **E***L*35, the results were comparable with the short-term trial although the overall TAVs were lower. This can be contributed to the decreased EPR-effect mediated tumor accumulation of the conjugate due to a lower tumor volume of both tumors. For this trial, mice with smaller tumors were chosen to allow a long-term observation without unethical tumor burden for these mice.

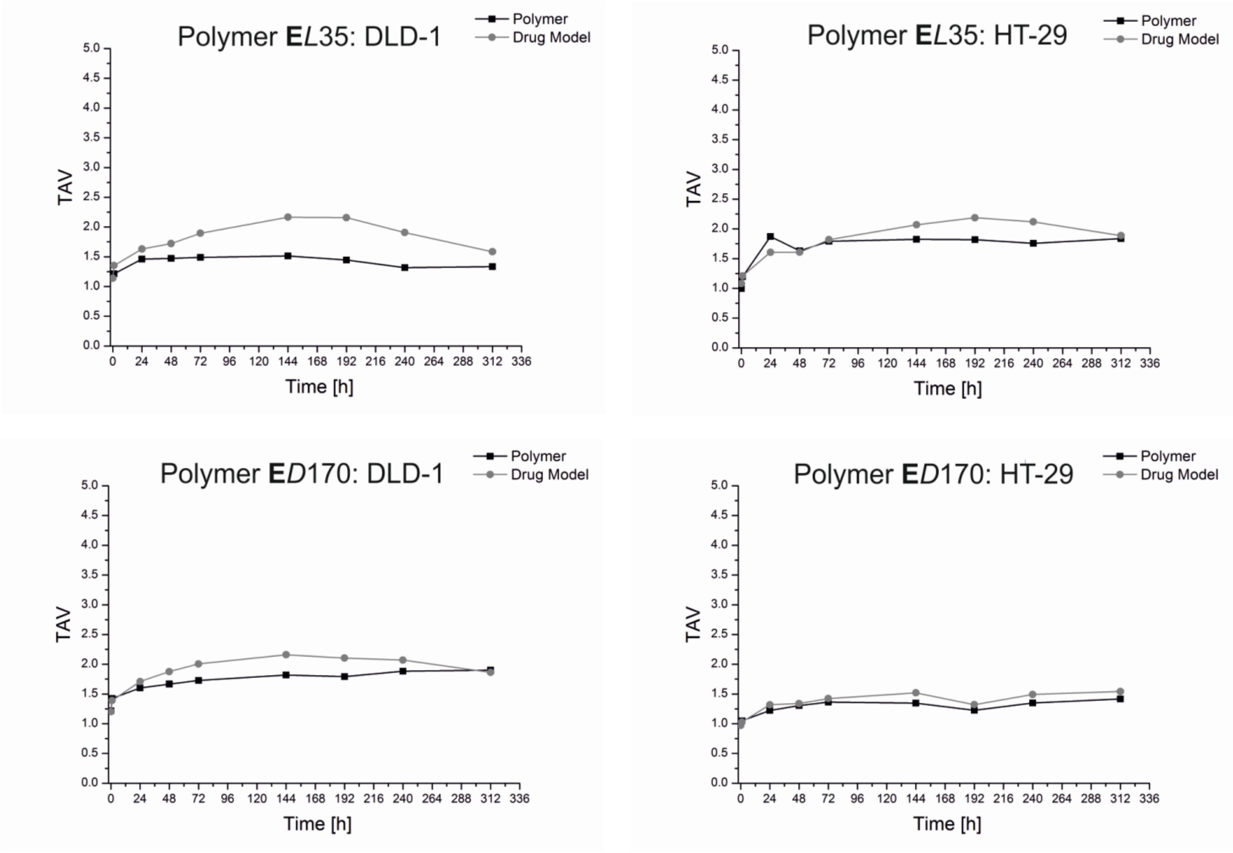

Fig. 25. TAVs over time of **E***L*35 and **E***D*170 and TAVs of the drug model (DY-676) respectively in one DLD-1 and HT-29 xenograft tumor bearing mouse (long-term observation).

Interestingly, the results of the *ex vivo* fluorescence analysis of the necropsied tumors 312 h after injection confirmed the anticipated drug model release also for the high M_w conjugate, at least in case of the DLD-1 xenograft (Fig. 26). The green and red signals in the composite images of the necropsied and cross-sectioned tumors clearly demonstrated different distribution of polymer and drug model within the tumor mass. A successful release of the drug model was verified. Although the long-term experiment has shown that the enzymatically triggered drug model release is also possible for the branched high M_w conjugate, it was again confirmed that the drug release is strongly affected due to the existence of steric hindrance for the lysosomal enzymes. Despite the dendritic structure, the side chains of this conjugate exhibit certain flexibility. This might have enabled the slow enzymatic release of the drug model, at least within two weeks. Nevertheless, the low M_w conjugate is much more advantageous as the tumor-site specific drug model release happened more efficiently and within an acceptable time period.

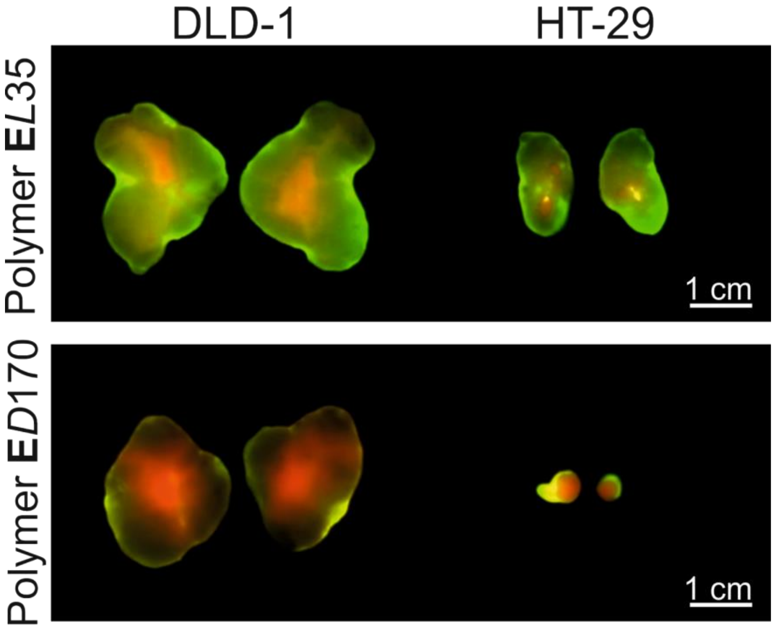

Fig. 26. Composite image of excised and cross-sectioned DLD-1 and HT-29 tumors 312 h after treatment with either **E***L*35 or **E***D*170. Polymer (DY-782): green; drug model (DY-676): red; merge: yellow. Green and red signals indicated a successful release of the drug model within the tumor.

Altogether, the comparison of the GFLG- with the disulfide-linker showed no remarkable differences regarding the suitability for a tumor site-specific drug release. Both systems showed excellent tumor accumulation and a tumor-site specific release of the drug model. In both cases, the lower M_w conjugate was superior regarding the drug model release, which should be considered for the design of further conjugates.

3.1.2.2 Summary

Here, the use of an enzymatically cleavable tetrapeptide linker (GFLG) was investigated for its ability to achieve a tumor-site specific drug model release. Therefore, two double labeled HPMA-based copolymers, differing in their architecture and M_w, were designed and tested in DLD-1 and HT-29 tumor-bearing mice using msFI. Two different fluorescent labels were used. One was attached to the polymer via a non-degradable amide bond and the other via an enzymatically degradable GFLG-linker. Both *in vivo* and *ex vivo* experiments showed strong fluorescence signals in tumors due to accumulation of the carriers. Furthermore, different patterns of drug model and polymer distribution *in vivo* and also *ex vivo* indicated an efficient release of the drug model at least for the **E***L*35 conjugate. The TAV evaluation of both polymer carriers and drug models confirmed the assumed tumor-site specific drug release. This effect was much more pronounced for **E***L*35. Regarding the different xenograft types, no remarkable differences in the extent of drug model release between DLD-1 and HT-29 tumors were observable. The clear advantage of the lower M_w conjugate was comparable to the results with the pHPMA conjugate with reductive cleavable disulfide bond. As enzymes are involved in the cleavage of the linker between drug model and polymer carrier, steric hindrance needs to be considered also here. In case of the bulky high M_w conjugate, the accessibility for the lysosomal enzymes is restricted, resulting in a decreased efficiency of drug model release. A performed long-term observation for two weeks revealed that a release of the drug model from the high M_w conjugate is possible. Nevertheless, it can be stated that in case of enzymatically cleavable linkers the lower M_w conjugates are more advantageous, although tumor accumulation of the higher M_w conjugates is enhanced due to elongated circulation time in the mouse body. The enzymatically degradable GFLG spacer was shown to be specifically cleaved inside the tumors. Consequently, it can serve as a suitable linker between the drug and polymer carrier in conjugates for cancer therapy. This was already confirmed in several therapy studies by the groups of Kopeček and Etrych where the drug model was replaced by a real chemotherapeutic drug such as doxorubicin to determine the therapeutic efficacy in the treatment of cancer (33, 55, 62). The results confirm the suitability of this linker to achieve a site-specific drug release and thereby a highly successful cancer treatment.

3.1.3 HPMA copolymers with pH-sensitive drug release

In addition to reductive and enzyme triggered systems, it was now very interesting to compare the gathered results with a pH-dependent system. Therefore, pHPMA conjugates with pH-sensitive drug release were investigated. Again, two conjugates that differed in architecture and M_w were compared regarding their biodistribution and tumor accumulation. These studies were performed by Hoffmann *et al.* and were already published in 2012 (45). A linear 30 kDa and a star-like shaped 200 kDa pHPMA conjugate were respectively labeled with the covalently bound NIR dye DY-782 as a polymer label and the red dye DY-676 which was linked via a pH-sensitive cleavable hydrazone bond, thereby acting as a drug model. The hydrazone bond is rather stable under physiologic conditions (pH 7.4) and cleavable in slight acidic milieu (63), as it is assumable in most solid tumors (64–66). A pH gradient between intra- and extracellular compartments of tumor tissue arises amongst other contributing factors from the high glycolysis rates of cancer cells (67, 68). The resulting slightly acidic microenvironment should enable a drug release preferentially in the tumor, whereas the toxic side effects are decreased because of negligible peripheral release. In the study of Hoffmann *et al.* the EPR-effect mediated tumor accumulation and a tumor-site specific drug release was proven for both conjugates. Thereby, the suitability of the hydrazone bond as a potential linker for the achievement of tumor site specific pH-triggered drug release from HPMA copolymers was determined. Due to the higher M_w and thereby restricted renal elimination, the star-like conjugate showed prolonged circulation in the mouse body. As a consequence, a much higher accumulation of the conjugate itself and also of the drug model was observed for the star-like high M_w conjugate (45). Compared with the enzymatically cleavable GFLG-linker and the reduction-sensitive disulfide linker, the pH-sensitive hydrazone bond showed comparable tumor-site specific drug release and the conjugates exhibited also excellent tumor accumulation. One advantage of this linker was the independency of enzymes, in contrast to the GFLG linker and partly also the disulfide bond. As a result, steric hindrance did not hamper the pH-sensitive drug model release from the higher M_w conjugate but increased drug model accumulation could be achieved due to the elongated circulation time within the blood stream. As the thereby increased drug delivery to the tumor site would be beneficial for the anticancer treatment, it was focused on the star-like pHPMA conjugate for the further studies.

The experiments were continued with a star-like 200 kDa pHPMA conjugate (**A***S*200Dox) which was composed of linear pHPMA side chains linked via an amide bond to a poly-amidoamine (PAMAM) dendrimer core. These side chains were stably labeled with the NIR dye DY-782 to track the *in vivo* fate and additionally with the chemotherapeutic agent doxorubicin, attached via pH-dependent cleavable hydrazone bond to the polymer backbone (Fig. 27). Doxorubicin was chosen for its importance as an anticancer agent. In addition, its intrinsic fluorescence can permit the analyses of the intratumoral drug accumulation by the use of msFI at least *ex vivo*. In a small trial this pHPMA-drug conjugate was investigated regarding its biodistribution and tumor accumulation. Further, it was checked whether both biodistribution and tumor accumulation are affected by the way of conjugate administration.

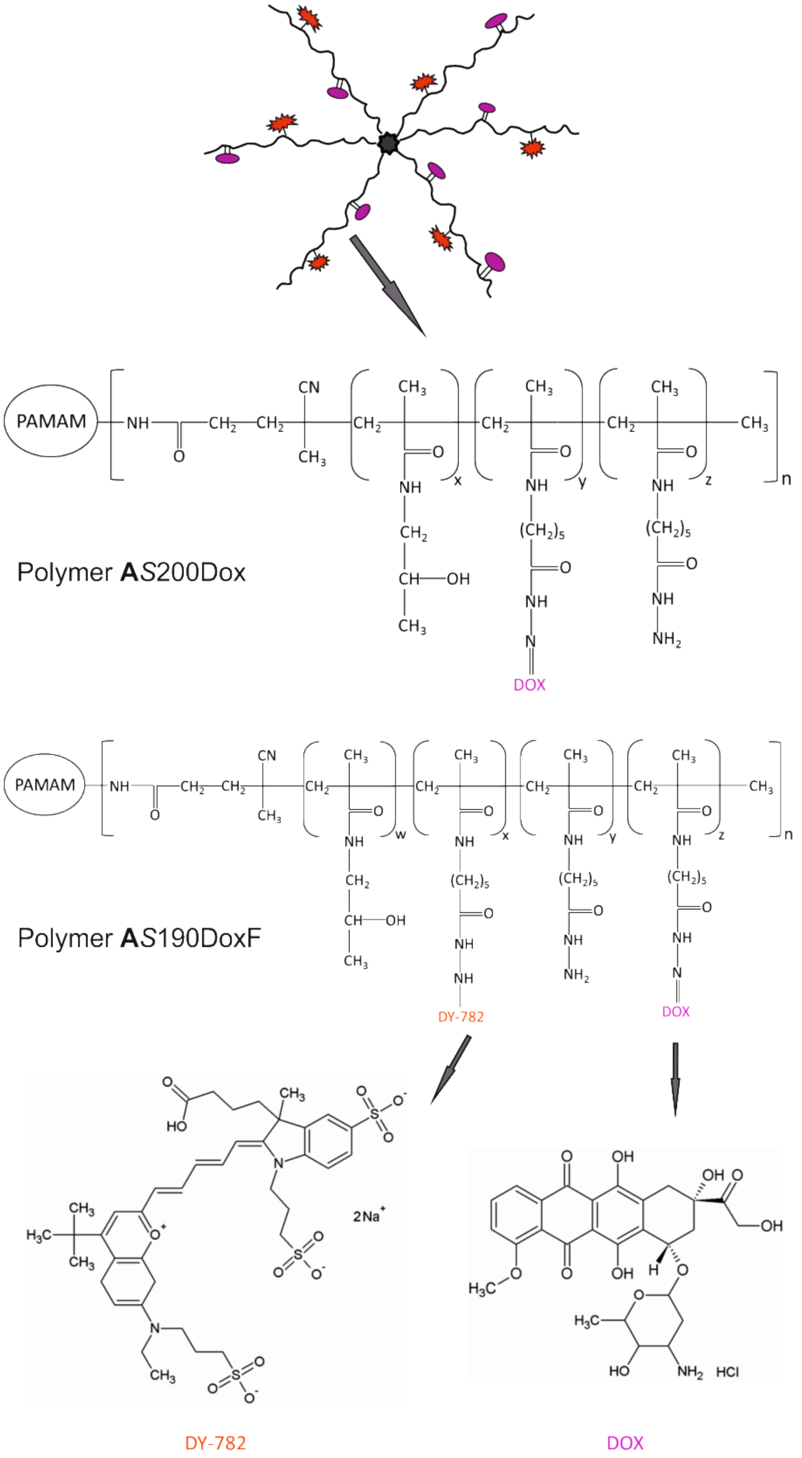
PAMAM
Polymer **A**S200Dox
DOX
PAMAM
Polymer **A**S190DoxF
DY-782
DOX
2Na+
HCl
DY-782
DOX

Fig. 27. Schematic structure of the star-like 200 kDa pHPMA-Dox conjugates with pH-sensitive drug release. The star-like conjugate is composed of several linear chains which are linked via an amide bond to the PAMAM dendrimer core. The conjugate **A***S*200Dox contains only the pH-sensitive linked drug doxorubicin. The conjugate **A***S*190DoxF instead contains a covalently linked fluorescent label DY-782 (-red) and the cleavable, pH-sensitive linked drug doxorubicin (=purple).

Here, the same amount of the fluorescently labeled star-like 190 kDa pHPMA-doxorubicin conjugate (**A***S*190DoxF) was administered either i.v. or i.p. to DLD-1 human colon carcinoma xenograft-bearing athymic nude mice. The *in vivo* fate of the conjugate was then determined by msFI. Additionally, the necropsied tumors were investigated by *ex vivo* msFI. The comparison of these two ways of application was very interesting, as the predominant method of i.v. injection causes a lot of stress for the mice, which might influence therapeutic results and furthermore the veins could get damaged due to small extravasates, especially after repetitive treatments. As further studies were planned to consider higher animal numbers per group and repetitive treatments, this study provided very important information.

3.1.3.1 Comparison of the biodistribution and tumor accumulation after i.v. and i.p. administration

The determination of the biodistribution and tumor accumulation of the **A***S*190DoxF conjugate was performed in DLD-1 human colon carcinoma xenograft-bearing athymic nude mice. They received respectively either an i.v. or i.p. injection of the conjugate according to a doxorubicin concentration of 5 mg/kg bodyweight and were observed by msFI immediately and also 1, 24, 72 and 120 h after injection. Afterwards, the distribution patterns of the polymer signal were compared (Fig. 28). Immediately and 1 h after the respective injection the distribution patterns of the conjugate were different. In case of the mouse which was treated by i.v. injection, the whole mouse gave a strong polymer signal indicating the circulation of the conjugate through the blood stream of the mice, whereas the i.p. injected mice only exhibited a strong fluorescence signal in the peritoneal region. The residual body and especially the tumor region appeared dark. One hour after injection, there was already a slight tumor accumulation visible in case of the i.v. injected mice. Also in the i.p. injected mice a slight distribution of the polymer away from the peritoneal region was observable. After 24 h the distribution patterns were similar. The i.v. injected mice as well as the i.p. injected mice exhibited a strong polymer derived fluorescence signal in the tumor region proving excellent EPR-effect mediated tumor accumulation of the conjugate. Henceforth, no differences regarding biodistribution or tumor accumulation were noticeable independent of the way of previous administration of the conjugate. The highest fluorescence intensity was measured after 72 h indicating maximal accumulation of the conjugate. Afterwards, the fluorescence intensity decreased (Fig. 28).

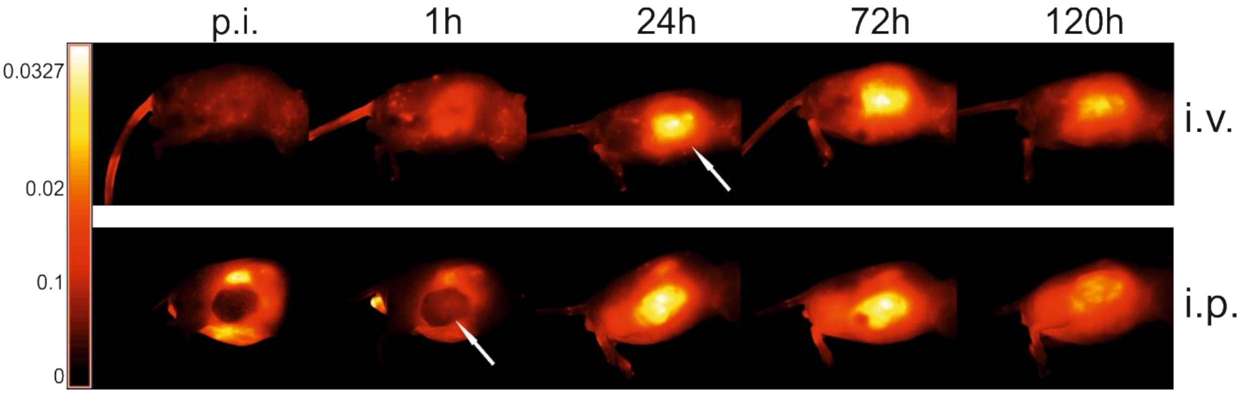

Fig. 28. The *in vivo* fluorescence signal of the polymer label DY-782 is displayed to visualize the biodistribution of the conjugate **A***S*190DoxF after either i.v. or i.p. injection. Initially, the distribution patterns differed but after 24 h a comparable biodistribution and excellent tumor (white arrows) accumulation of the conjugate was visible for both application ways.

These results showed that despite the different distribution behavior during the first hours after the respective administration, the achieved tumor accumulation after 24 h was equivalent. The stress for the mice during the injection procedure was remarkably decreased during i.p. injection compared to i.v. injection. As there were no acute toxic side effects noticeable, neither after a single i.p. nor after i.v. injection, it was concluded that both ways of application are suitable for the administration of the pHPMA-doxorubicin conjugate. Nevertheless, the conjugates were administered i.v. whenever possible, as it is much more comparable with the actual way of administration in the clinic.

Investigations of the biodistribution of these pHPMA conjugates raised the question of the *in vivo* fate of the polymer carrier beyond tumor accumulation. The non-biodegradability of HPMA copolymers is an undesirable property which should not be neglected. The renal clearance of pHPMA conjugates is strongly dependent on their M_w, R_H and on their architecture. Several previous studies have shown that the renal threshold for macromolecules exhibiting R_H below 5 nm ranges from 30 kDa up to 50 kDa and is further influenced by the polymer architecture. It was shown that the limit for renal filtration is much higher for linear HPMA copolymers than for star-like conjugates. Due to their linear shape and thereby increased flexibility, pHPMA conjugates with M_w up to 70 kDa could have been filtrated by the kidneys, although this process took a longer time than simple filtration of smaller molecules. Star-like shaped pHPMA conjugates instead are highly branched and less flexible which affects their renal elimination. The renal threshold for those star-like pHPMA conjugates was found to be around 50 kDa but it is also strongly dependent on the R_H of the polymer coil in solution which can range from 5 to 14 nm. The diameter of glomerular pores was found to be in a range of 4 to 14 nm in rats and mice, whereas in humans smaller pores were found to be 4 – 5 nm and larger pores 8 – 10 nm in diameter (11, 69, 70). Therefore, it is assumable that the renal elimination of pHPMA conjugates with R_H above 5 nm is limited. Furthermore, it becomes obvious that the renal elimination of the applied 200 kDa star-like pHPMA conjugate, which exhibits a highly branched structure, a M_w above the renal threshold and a R_H of approximately 13 nm, is strongly restricted. This leads to prolonged blood circulation and thereby enhanced EPR-effect mediated tumor accumulation. Despite the restricted renal elimination, previous biodistribution studies performed in our laboratory showed that after 3 months the amount of the star-like 200 kDa pHPMA-conjugate was below detection threshold, indicating elimination by comparatively slow processes via liver and bile (11, 45). Nevertheless, to avoid undesirable long-term accumulation of these conjugates, the elimination should be allowed within a shorter time due to renal excretion. For this purpose, high molecular weight HPMA copolymers that are degradable into lower M_w units lying below renal threshold were already developed. The presence of the already described enzymatically cleavable amino acid sequence GFLG between the core and the side chains of the star-like polymer conjugates enables the disassembly of the structure (71, 72) after its intratumoral arrival. This might be a suitable way to optimize the current pHPMA–doxorubicin conjugates which should be considered in further studies.

After the comparative investigation of i.v. and i.p. administration, the necropsied organs and tumors were examined (Fig. 29). Besides the strong polymer signal detected in the tumor, a comparatively strong polymer signal was also detected in the kidneys. As the renal elimination of the 200 kDa conjugate is restricted and no signal in the bladder was detected, most probably an interaction between the pHPMA conjugate and the glomerular basement membrane in the kidneys can be assumed. This was already observed and discussed in previous studies (45, 60, 73). No acute toxic side effects have been observed despite the accumulation. The doxorubicin signal detected in the testes indicated the presence of doxorubicin. The undesirable testicular toxicity of doxorubicin is well known (74, 75) but should be decreased due to the enhanced tumor specific accumulation of the pHPMA-doxorubicin conjugate compared to unbound doxorubicin. Nevertheless, toxic side effects cannot be prevented completely, as a slight peripheral release over time as well as a recirculation of the released doxorubicin from the tumor site can occur. However, doxorubicin was predominantly detectable in the tumor. The results confirmed the excellent tumor accumulation of the pHPMA-doxorubicin conjugate and a tumor site-specific drug release.

The necropsied tumors were cross-sectioned and also examined individually by msFI. The NIR filter set was used to detect the polymer signal (DY-782) and the blue filter set was used to detect doxorubicin. As this drug exhibits an intrinsic fluorescence with an emission maximum in the blue wavelength range (approx. 560-630 nm), it was possible to determine the doxorubicin localization in organs and tumors. Unfortunately, the detection of the doxorubicin signal was not possible *in vivo*, as the mice showed very strong autofluorescence within the blue wavelength range. Furthermore, the penetration depth of the excitation and emission light is strongly limited within this wavelength range. Using *ex vivo* imaging, it was possible to subtract the autofluorescence by the unmixing tool of Maestro™ software and to determine the doxorubicin derived fluorescence signal. As the doxorubicin signal was detected predominantly in the tumors, a site-specific pH-triggered drug release was confirmed.

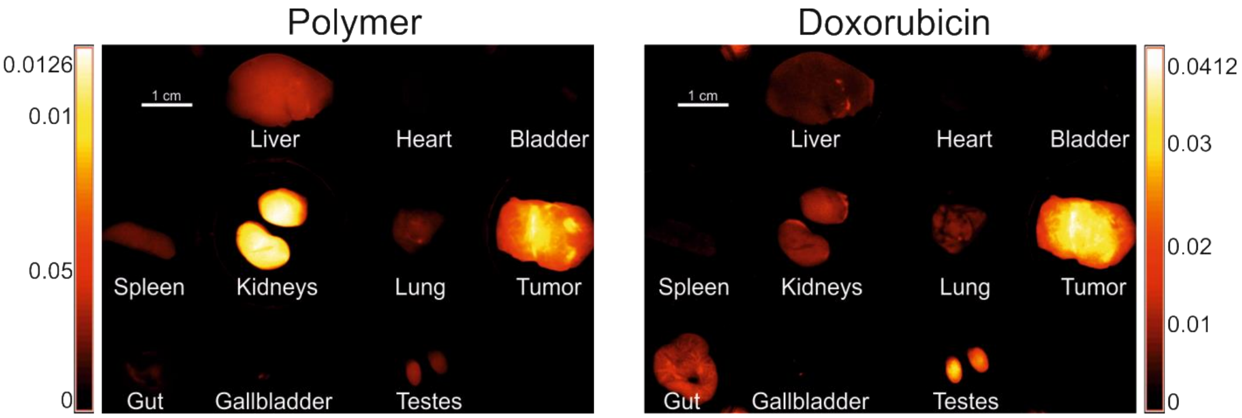

Fig. 29. Fluorescence images of organs and tumors excised from a mouse 72 h after treatment with the conjugate **A***S*190DoxF. Polymer (DY-782) and doxorubicin signals are displayed to visualize their different distribution and to confirm a tumor-site specific drug release.

Comparing the distribution pattern of the polymer and the doxorubicin derived fluorescence signal in the examined tumor cross-sections (Fig. 30), it was observable that doxorubicin was found preferentially in the tumor center, while the polymer was distributed homogeneously over the whole tumor area. As the patterns of both signals were not congruent, a site-specific drug release was confirmed. The inhomogeneous distribution of doxorubicin within the tumor could be explained by the specific substructure of the DLD-1 xenograft model. This tumor type is characterized by large necrotic and fibrotic areas especially in the tumor center. Furthermore, these tumors exhibit only a very marginal vascularization. Vital tumor cells are mainly localized around these few blood vessels and in the rim zone of the tumor. It can be assumed that the microenvironment in the vicinity of the large necrotic areas is more acidic compared to the areas of vital tumor cells. Therefore, the pH-sensitive drug release is supposed to be increased in the proximity of necrotic regions. This phenomenon was already discussed in previous studies (45). Furthermore, the removal of the cleaved drug out of these necrotic/fibrotic regions is restricted due to lacking blood vessels and lymphatic system. This effect also leads to the enhanced accumulation of the drug within these areas. This is not necessarily advantageous, as the vital tumor cells are the target for doxorubicin. If doxorubicin cannot be delivered to these cells but is rather trapped in the necrotic/fibrotic regions where it was predominantly released, the therapeutic success might be decreased. As it is a very important subject, the problem of tumor structure dependent therapeutic efficacy will be further addressed in section 3.3.5.

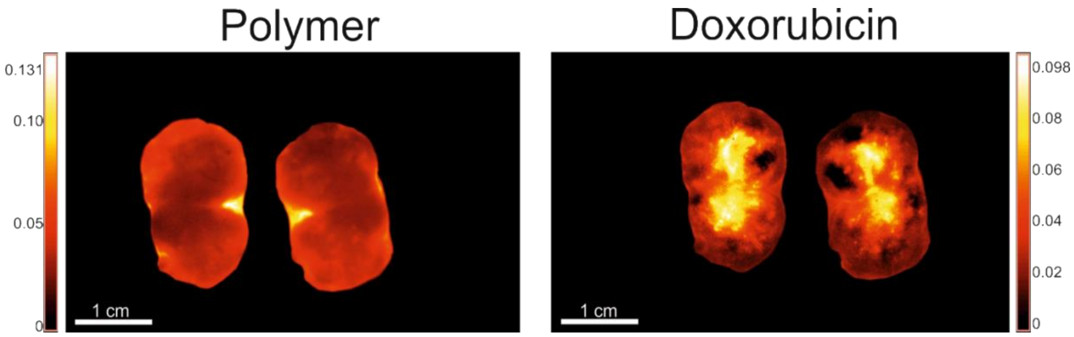

Fig. 30. Fluorescence images of a necropsied and cross-sectioned DLD-1 tumor 72 h after treatment with the conjugate **A***S*190DoxF. Polymer (DY-782) and doxorubicin signals are displayed to visualize their different tumor distribution which confirmed a tumor-site specific drug release.

3.1.3.2 Summary

Previous studies have already shown that linking a drug model via hydrazone bond to the polymeric carrier represents a promising system to achieve a pH-triggered tumor-site specific drug release. Hoffmann *et al.* confirmed the concept by using a double labeled star-like 200 kDa pHPMA conjugate. While the polymer carrier was covalently labeled, the drug model was attached via pH-dependent cleavable hydrazone bond. As a clear tumor-site specific release of the drug model was observed, further studies regarding biodistribution and tumor accumulation were conducted with a star-like 190 kDa pHPMA-doxorubicin conjugate. Here, the excellent tumor accumulation even of the doxorubicin-loaded conjugate was proven by msFI and also a site-specific drug release was confirmed when tumor cross-sections were examined. Furthermore, the i.p. administration of the pHPMA-doxorubicin conjugate was compared to the usual i.v. administration to check the suitability of this administration type for further studies with a higher number of animals and repetitive treatments. After the i.v. and i.p. administration the distribution patterns differed initially. However, after 24 h the tumor accumulation was comparable indicating complete redistribution from the injection site to the solid tumors even after i.p. administration. Neither toxic side effects, nor differences in the extent of tumor accumulation were visible comparing both application types. Therefore, it can be assumed that the i.p. administration is a suitable way of administration in case of hindered i.v. injection. As the results for the tumor accumulation and tumor-site specific drug release of the pHPMA-doxorubicin conjugate were very promising, its therapeutic efficacy compared to the unbound drug was determined. The results of this study will be described in the next chapter.

3.2 Therapy study with HPMA copolymers with pH-sensitive drug-release[3]

In this work, three different pHPMA conjugates with stimulus-sensitive drug release were examined. The conjugate with the reductive cleavable linker as well as the conjugates with enzymatic and pH-dependent drug release were all promising systems for cancer therapy and it would be interesting to determine their efficacy by the performance of a therapy study. As the synthesis of the reduction-sensitive conjugate loaded with a chemotherapeutic drug was comparatively difficult and systems with the enzymatically cleavable linker (GFLG) were already examined by the group of Kopeček, it was focused on the conjugate with the pH-sensitive drug release. To be more precise, a star-like shaped 200 kDa pHPMA conjugate loaded with doxorubicin via pH-dependent cleavable hydrazone bond (**A***S*200Dox) was examined regarding its therapeutic efficacy in drug resistant tumor bearing mice. In the following sections the results will be presented and discussed.

3.2.1 Evaluation of a drug resistant tumor model

First, a doxorubicin-resistant tumor model was determined, as this was an important prerequisite for proving the potential of the pHPMA conjugates to overcome chemotherapy resistance. Therefore, *in vitro* cytotoxicity tests (SRB-assays) with doxorubicin were performed with cell lines from different entities. For this cytotoxicity test, the cells of the respective cell line were seeded in 96-well plates and incubated with serial dilutions of doxorubicin for 96 h. The application of the protein binding dye SRB then allowed the evaluation of the assay. As the protein binding of SRB is proportional to the cell mass, it was possible to determine the cell mass by optical density measurements of the extracted dye amount. Thereby, the cell growth dependent on the applied doxorubicin concentration was determined. Furthermore, the respective IC_{50} value, which represents the half maximal inhibitory concentration of the respective drug, was determined for each cell line and was chosen to evaluate the sensitivity to doxorubicin. Among the examined cell lines only one, the A2780 human ovarian carcinoma cell line, showed an apparent sensitivity to doxorubicin with an IC_{50} value of 3 nM. The other cell lines had distinctly higher IC_{50} values ranging from 15 nM to 35 nM. As potential doxorubicin resistant tumor models, the multi-drug resistant human germ cell tumor cell line 1411HP with an IC_{50} of 35 nM and the cell line A2780cis, a cisplatin resistant human ovarian carcinoma cell line which was also cross-resistant to doxorubicin and had an IC_{50} of 17 nM, were selected. The dose-response curves of the chosen cell lines are displayed in Fig. 31.

---

[3] These results have been published:
Heinrich A-K, Lucas H, Schindler L, Chytil P, Etrych T, Mäder K *et al.* Improved Tumor-Specific Drug Accumulation by Polymer Therapeutics with pH-Sensitive Drug Release Overcomes Chemotherapy Resistance. Molecular cancer therapeutics 2016; 15(5):998–1007.

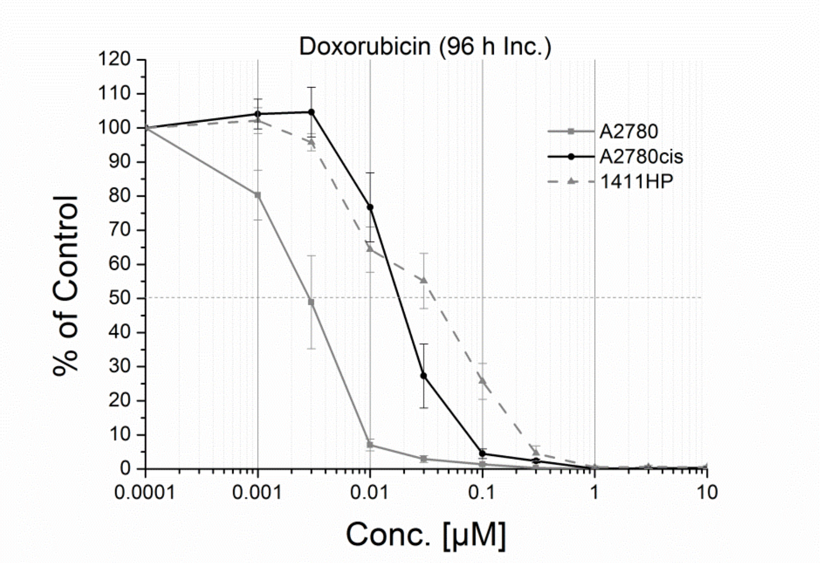

Fig. 31. Dose-response curves of 1411HP, A2780 and A2780cis cell line (Means ± SD; n = 3) determined after SRB-assay performance with doxorubicin (incubation time 96 h). Distinct doxorubicin resistance of A2780cis and 1411HP was visible compared to A2780, which is a doxorubicin sensitive cell line. Dotted line indicates half maximal inhibitory concentration (IC_{50}).

The cell line 1411HP represents a model of natural drug resistance since these cells were derived from a tumor of a patient with refractory disease after chemotherapy (76, 77), whereas the acquired drug resistance of A2780cis was artificially established, derived from its parental cell line A2780 (78). Moreover, the established xenograft tumors of both cell lines typically show very similar morphological characteristics. A tumor-structure independent comparison of these two tumor types seemed to be very promising.

In Fig. 32 H & E stained tumor sections from a 1411HP and an A2780cis xenograft are displayed. Analyzing these H & E stained tumor sections, it was visible that 1411HP and A2780cis xenograft tumors are characterized by a loose structured and highly vascularized tumor tissue. Many vital cells and a lack of necrotic/fibrotic areas, at least in smaller tumors, are also distinctive. Furthermore, they exhibit only a low amount of extracellular matrix (ECM) and show high growth rates *in vivo*.

Based on the results obtained *in vitro*, it was now important to confirm their doxorubicin resistance also *in vivo*.

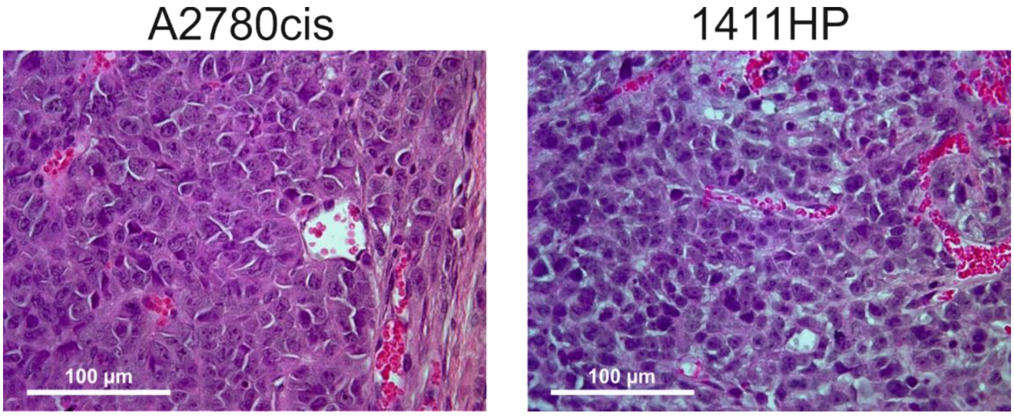

Fig. 32. H & E stained sections of necropsied 1411HP and A2780cis tumor xenografts. Cell nuclei appear purple, cytoplasm in pale pink and the erythrocytes in bold red. Both tumor xenografts exhibited a comparable morphological structure.

3.2.2 Verification of drug resistance *in vivo*

For the performance of a therapy study with the pHPMA-doxorubicin conjugate, it was interesting whether the differences observed *in vitro* can be reproduced *in vivo* in derived xenograft tumors. Therefore, respectively 10 A2780, A2780cis or 1411HP tumor xenograft bearing athymic nude mice were treated with either doxorubicin (5 mg/kg BW; n = 5) or phosphate buffered saline (PBS; n= 5) as a control. As shown in Fig. 33, treatment with doxorubicin on day 1 and day 4 induced regressions in sensitive A2780 tumors, which however turned into regrowth within few days. Due to the occurrence of treatment related toxic side effects, especially a loss of bodyweight, the next injection was possible on day 10 (1411HP and A2780cis at day 9 instead). The third doxorubicin application induced no further tumor regression and resulted in a pronounced toxicity (loss of bodyweight, atypical behavior), in some cases allowing no further treatment. Nevertheless, doxorubicin treatment resulted in a clear tumor growth inhibition compared to control treatment in doxorubicin sensitive A2780 tumors and a further control of tumor growth by treatment with doxorubicin seemed possible, at least in mice showing a higher tolerance of doxorubicin. In the resistant 1411HP tumors, the same treatment schedule induced only little growth retardations (Fig. 33) but also similar treatment related toxic effects with severe toxicity (loss of more than 20 % of initial bodyweight) in one mouse after the third injection of doxorubicin. In a comparative experiment with A2780cis tumor bearing mice, similar negligible growth retardation effects in response to doxorubicin treatment were observed (Fig. 34). This time only two injections (day 1 and 4) were administered due to pronounced toxic side effects after the second injection. Moreover, it was known from the previous trials that the third injection had no further impact on tumor growth but caused enhanced toxicity.

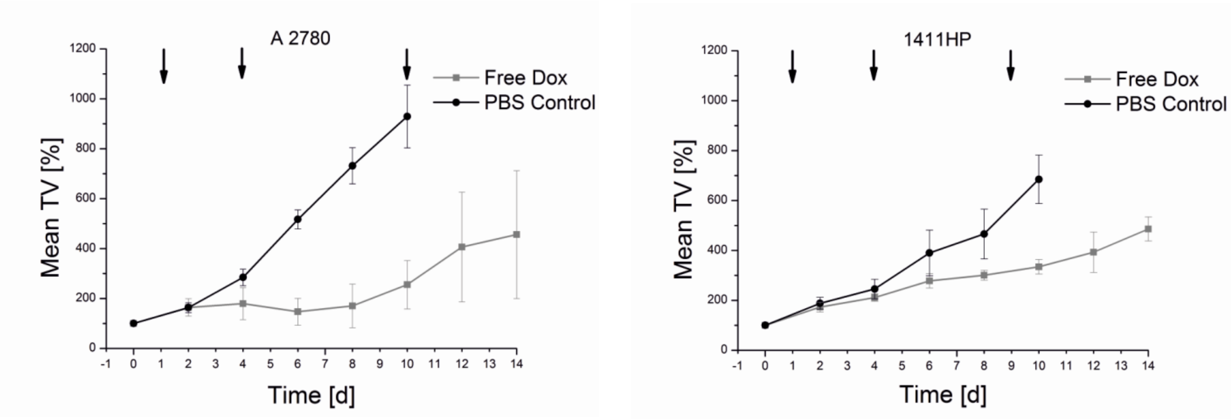

Fig. 33. Tumor volume (TV) increase over time normalized to day 0. PBS control groups (Means ± SD; each n = 5) and doxorubicin therapy groups (Means ± SD; each n = 5). Mice received either PBS or doxorubicin (5 mg/kg BW) i.v. at day 1, 4 and 9 (A2780 at day 10 instead). In each therapy group one mouse needed to be sacrificed due to severe toxicity already at day 9 (1411HP) and day 10 (A2780). Arrows point to treatments.

These analyses demonstrated that doxorubicin treatment, with dosages around the maximal tolerated dose, resulted in a clear but not prolonged response of a supposed doxorubicin sensitive tumor in the used nude mouse model. Notably, a very different extend of doxorubicin related toxicity among the mice was observed, ranging from good tolerability to severe side effects. The clear *in vitro* doxorubicin resistance of 1411HP and A2780cis was confirmed *in vivo*. Taking these results into account, it was finally decided to choose the 1411HP tumor cell line for the performance of a therapy study with the star-like 200 kDa pHPMA-doxorubicin conjugate (**A***S*200Dox). The A2780cis cell line was chosen as a comparative tumor model to determine the existence of a tumor-type-dependency regarding the applied treatment.

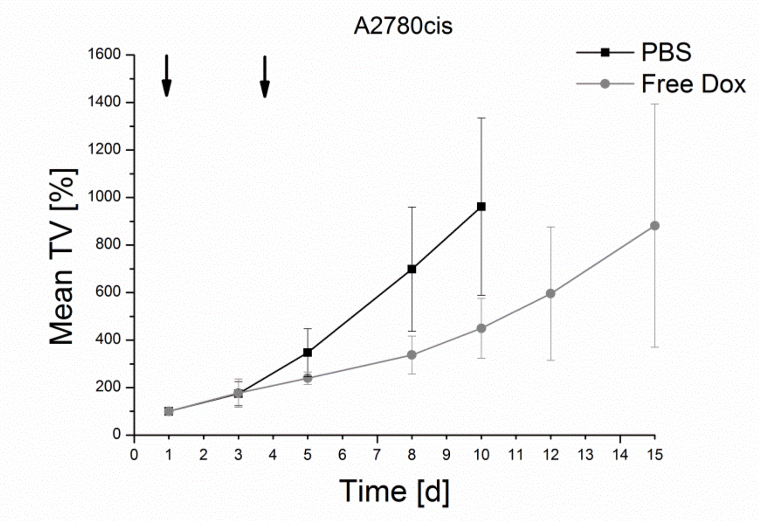

Fig. 34. TV increase over time normalized to day 1. PBS control group (Means ± SD; n = 5) and doxorubicin therapy group (Means ± SD; n = 5). Mice received either PBS or doxorubicin (5 mg/kg BW) i.v. at day 1 and 4. Arrows point to treatments.

3.2.3 Determination of efficacy: Therapy study with pHPMA-doxorubicin conjugates in drug resistant tumor bearing mice

For the performance of a therapy study with the **A***S*200Dox conjugate in comparison to the unbound drug (free doxorubicin), initially 21 drug resistant 1411HP tumor bearing athymic nude mice were subdivided into 4 groups according to their tumor sizes. Thereby, it was achieved that all treatment groups had a similar mean tumor volume at the beginning of the therapy. The mice received either i.v. injections of pHPMA-doxorubicin (according to a doxorubicin concentration of 5 mg/kg BW; n=6), free doxorubicin (5 mg/kg BW; n=6), unloaded star-like 200 kDa pHPMA-precursor (polymer concentration was chosen equally to polymer content of the pHPMA-doxorubicin injection; n=6) or PBS (n=3). The same treatment schedule was applied as it was used in the drug resistance verification study described above, which included injections on day 1, 4 and 9. After the first injection, it was observable that the treatment with free doxorubicin induced first signs of toxicity (slight bodyweight loss) but hardly any tumor inhibiting effects, as it was already expected from the previous trial (Fig. 35, A). As supposed, the treatment with both PBS and pHPMA precursor had no impact on tumor growth and was shown to be completely non-toxic (Fig. 35, A). Furthermore, the pHPMA-doxorubicin treatment induced no obvious tumor response and negligible toxic side effects after the first injection. As the drug carrier was expected to release the drug predominantly in the tumor avoiding systemic toxicity, now the 3-fold dose of the **A***S*200Dox conjugate (equivalent to 15 mg/kg BW doxorubicin) was administered on day 4 and 9. As this high dose of free doxorubicin would not have been tolerable for the mice, the dosage was kept constant at 5 mg/kg BW. The mouse monitoring was completed when at least two mice had reached maximal tolerated tumor volume or body weight loss of more than 20 % of the initial value. While the mice of the PBS group and the pHPMA precursor group needed to be sacrificed already at day 8 (PBS group) or respectively at day 12 (pHPMA-precusor group) due to tumor burden, only one mouse needed to be sacrificed in the free doxorubicin group at day 13 due to tumor burden and toxic side effects.

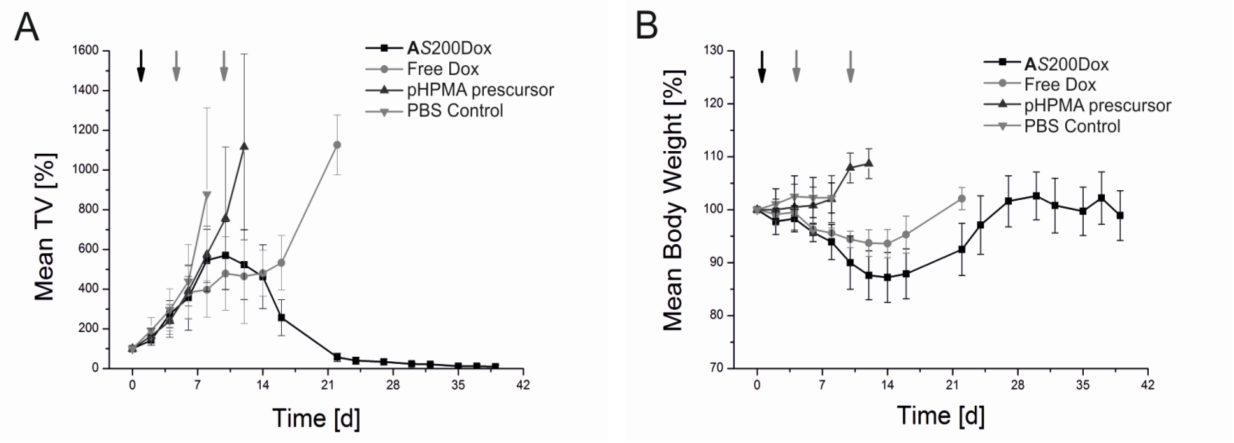

Fig. 35. (A) Tumor volume (TV) increase over time normalized to day 0 of 1411HP tumor-bearing mice. PBS control group (Means ± SD; n = 3) and pHPMA precursor, doxorubicin and pHPMA-doxorubicin conjugate group (Means ± SD; each n = 6). Mice received either PBS, pHPMA precursor, free doxorubicin or **A***S*200Dox conjugate (black arrow: 5 mg/kg BW, grey arrow: 15 mg/kg BW) i.v. at day 1, 4 and 9. Monitoring was completed when at least 2 mice within a group had reached maximal tolerated TV. In the doxorubicin group, one mouse needed to be sacrificed already at day 12 whereas the remaining mice were followed until day 16 when next 3 mice had reached maximal tolerated TV. Arrows point to treatments.

(B) Mean bodyweight (BW) over time normalized to day 0 of 1411HP tumor-bearing mice. PBS control group (Means ± SD; n = 3) and pHPMA precursor, doxorubicin and **A***S*200Dox group (Means ± SD; each n = 6). Mice received PBS, pHPMA precursor, free doxorubicin or **A***S*200Dox (black arrow: 5 mg/kg BW, grey arrow: 15 mg/kg BW) i.v. at day 1, 4 and 9. A loss of more than 20 % of the initial BW (day 0) was set as a termination criterion. Furthermore, monitoring was completed when at least 2 mice within a group had reached maximal tolerated tumor volume (TV). In the doxorubicin group one mouse needed to be sacrificed already at day 12 due to tumor burden and increased toxic side effects (bodyweight loss) whereas the remaining mice were followed until day 16 when next 3 mice had reached maximal tolerated TV and an increased loss of bodyweight.

The remaining mice of this group were further monitored, to determine if there will be a clear difference in tumor response compared to pHPMA-doxorubicin treatment over time. However, already at day 16 the next 3 mice needed to be sacrificed due to increased toxic side effects such as bodyweight loss and atypical behavior. The remaining two mice were observed up to day 22 when they needed to be sacrificed as well. The changed treatment schedule in the **A***S*200Dox group induced some signs of toxicity associated with weight loss up to 13 % of the initial bodyweight (Fig. 35, B) but unfortunately no clear tumor response could be noticed. Unexpectedly, after the third injection (day 9) the tumors started to continuously regress, they finally reached a non-measurable stage (from day 21) for 80 days and even completely disappeared in 3 mice (Fig. 35, A). This delayed but strong tumor response was quite surprising and the clear superiority of the pHPMA-doxorubicin treatment compared to free doxorubicin could be visualized by the tumor volume curves and by the Kaplan-Meier plot (Fig. 36). This plot showed the cumulative survival of the mice of each group over time. While the mice of all other groups needed to be sacrificed due to tumor burden and toxic side effects, all mice of the pHPMA-doxorubicin group survived. Furthermore, the mice of the pHPMA-Dox conjugate group regained the lost weight during the tumor regression stage and recovered quickly.

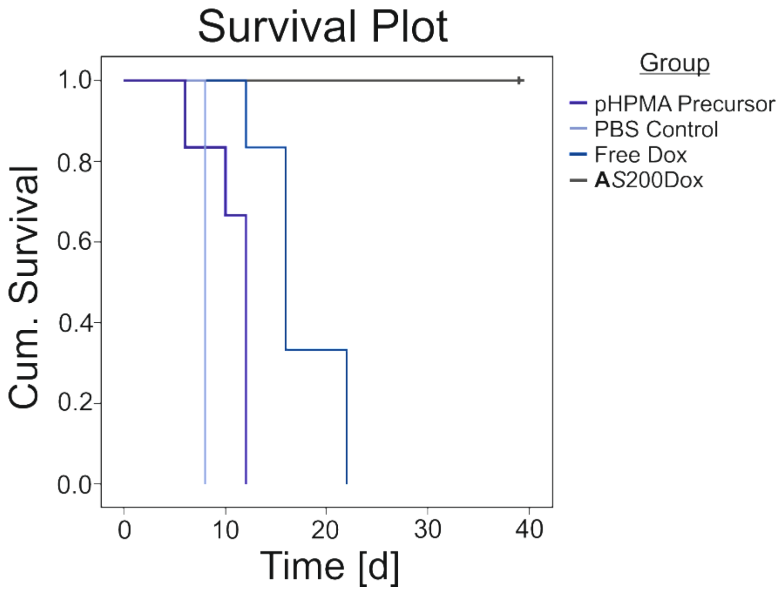

Fig. 36. Cumulative survival of mice under respective therapy (PBS, free doxorubicin, **A***S*200Dox conjugate and pHPMA precursor) is displayed (Kaplan-Meier plot). The advantage of the polymeric treatment is clearly visible. All mice of **A***S*200Dox group are still alive on day 40 whereas all mice of the control groups and free doxorubicin group needed to be sacrificed.

The question arises why the tumor response of the 1411HP tumors occurred not until day 10. The most reasonable assumption was that the microenvironment in this tumor type was initially not sufficient for an effective drug release. As the drug was bound via hydrazone bond, which is supposed to be stable in blood stream but cleavable under slight acidic conditions, an effective tumor-site specific drug release was expected due to the mild acidic conditions. As already mentioned above, it is commonly known that most solid tumors exhibit a slightly acidic microenvironment compared to normal tissues (64–66), resulting amongst other contributing factors from the high glycolysis rates of cancer cells (6). Furthermore, the occurrence of hypoxia within tumor tissue also supports the acidification of the microenvironment due to the hypoxia induced cascade which leads to an upregulation of carbonic anhydrase IX (79). It was assumed that the 1411HP tumor exhibited a microenvironment which was less acidic compared to other solid tumors, resulting in a non-effective drug release in the beginning. This xenograft model is extensively vascularized and exhibits only a very low amount of necrotic areas. This could be one possible explanation for the inappropriate microenvironment in the beginning of the therapy. Although the treatment with the **A***S*200Dox conjugate induced no tumor regression until day 10, it was assumed that a therapy induced switch of the tumor microenvironment happened over time, resulting in a sudden drug release of the strongly accumulated pHPMA-doxorubicin conjugate. The presence of a very high dose of doxorubicin within the tumor tissue could have induced the strong regression of the 1411HP tumors. Further trials to confirm this assumption were performed later and are described in the following sections.

With the aim to visualize changes within the 1411HP tumors under the respective therapy, histological examinations were performed. 1411HP tumor xenograft bearing mice were either treated once with PBS or once or twice (day 1 & 4) with a 3-fold dose of **A***S*200Dox. After the confirmation of lacking tumor response of the PBS and once **A***S*200Dox treated mice they were sacrificed and tumors necropsied. In case of the mouse which was treated with two 3-fold **A***S*200Dox conjugate injections, tumor necropsy was performed after the first signs of tumor response were recognized. Subsequently, the necropsied 1411HP tumors were formalin fixed, paraffin embedded and sliced. The obtained tumor sections were then microscopically examined after H & E staining. Interestingly, a clear difference between the untreated, still non-responding and responding tumors was observed. The overall tissue structure of responding tumors (2x 3-fold dose administered at day 1 & 4) was characterized by stressed, more loosely structured, swollen cells (Fig. 37, right) accompanied by many apoptotic areas. In contrast, the non-responding tumors (1x 3-fold dose administered) rather resembled to untreated tumors (Fig. 37, middle and left) but they already exhibited some apoptotic areas. These analyses confirmed the observation of a delayed tumor response on a histological level.

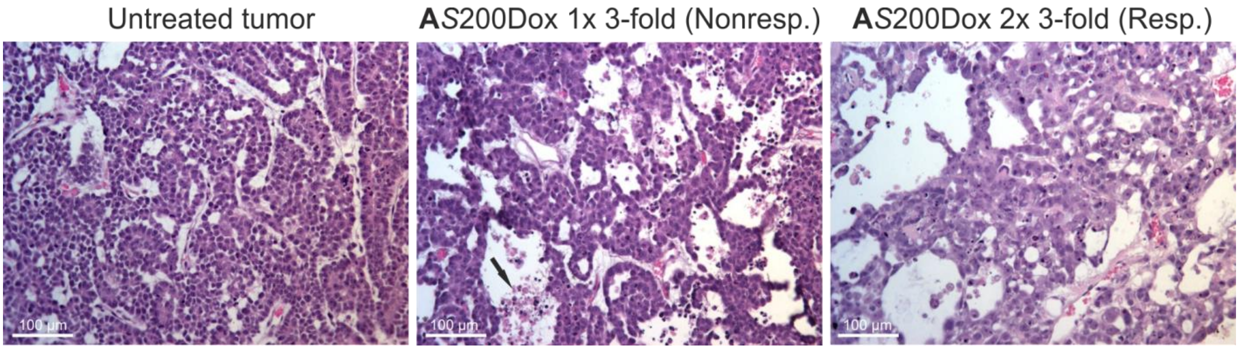
Untreated tumor
A*S*200Dox 1x 3-fold (Nonresp.)
A*S*200Dox 2x 3-fold (Resp.)
100 µm
100 µm
100 µm

Fig. 37. H & E stained slices of untreated, still non-responding and responding tumors after necropsy. Tissue structure of responding tumors is characterized by stressed, more loosely structured, swollen cells (right) accompanied by many apoptotic areas. The non-responding tumor (middle) rather resembled to untreated tumors (left) but already exhibited some apoptotic areas (black arrow) White bars display 100 µm.

Next, it was interesting to compare the results gathered from the therapy study with 1411HP-tumor bearing mice with the A2780cis tumor model to check whether they show a comparable tumor response to the treatment. Because of the similar morphologic tumor substructure, an equal tumor response compared with 1411HP tumors was expected. To verify this assumption, A2780cis tumor bearing mice received **A***S*200Dox injections. The same treatment schedule as it was used in the therapy study above was applied. This schedule also induced slight tumor regressions already after the second and complete tumor regression after the third injection. Surprisingly, it induced a much higher treatment related toxicity or, more specifically, a higher body weight loss already after the first injection. One mouse needed to be sacrificed due to body weight loss of more than 20 % of the initial weight already after the second injection. The other mouse was monitored until day 18 when the tumor was nearly completely disappeared. But the increased body weight loss hampered the correct tumor measurements. Thus, the efficacy was determined in another trial with lower total doses later. It can be assumed, that the toxic side effects occur when the doxorubicin is cleaved from the polymer backbone very early, resulting in a recirculation of the free doxorubicin out of the tumor tissue, providing that it was not already internalized into the cells or was pumped out via efflux pumps like MDR-1. This efflux pump is expressed by these multi-drug resistant tumor cells and represents one of their multiple resistance mechanisms (80, 81). Presumably, compared to 1411HP tumors, this tumor type offers a more sufficient microenvironment for the pH-dependent drug release already before the treatment has been started, despite the similar substructure. This might have led to a quicker release of doxorubicin from the accumulated pHPMA-doxorubicin conjugate. Therefore, a quicker tumor response would be expectable but it needs to be considered that the doxorubicin amount after the first injection is obviously lower compared to the accumulated doxorubicin amount after the triple injection. As a result, further injections in the A2780cis tumor-bearing mice were needed despite the early doxorubicin release to achieve an effective tumor response. It can be supposed that only the high local dose of doxorubicin, achieved by the applied therapy schedule, is able to overcome the chemotherapy resistance of both tumor types. Probably, the overall dose could have been reduced in the A2780cis tumor because of the more sufficient micro milieu within the tumor. This would also prevent the much more pronounced toxic side effects. To determine the efficacy and toxicity of different treatment schedules, several studies were performed and the results are described in the following sections.

3.2.4 Summary

For the determination of the suitability of the pHPMA-doxorubicin conjugate with pH-sensitive drug release for a highly effective cancer therapy, doxorubicin resistant tumor models were applied, to consider the most challenging case. Therefore, *in vitro* cytotoxicity tests with several tumor cell lines were performed to evaluate their respective sensitivity against doxorubicin. Two cell lines were chosen as appropriate candidates for further studies. The multi-drug resistant human germ cell tumor cell line 1411HP and the human ovarian carcinoma cell line A2780cis, a cisplatin resistant variant of the parental cell line A2780 which exhibited also a distinct cross-resistance to doxorubicin. The xenograft tumors of both cell lines exhibited comparable tumor substructures and their doxorubicin resistance was confirmed *in vivo* in comparison to sensitive A2780 tumor xenografts. As the 1411HP cell line exhibited still higher IC_{50} values for doxorubicin compared to A2780cis and was shown to be resistant *in vivo* as well, a therapy study with the **A***S*200Dox conjugate was conducted in 1411HP tumor xenograft bearing mice first. The results were astonishing. After an initial tumor non-response to the applied treatment, finally a complete tumor regression was achieved in the **A***S*200Dox treatment group. An increased dose up to a threefold doxorubicin equivalent dose (15 mg/kg BW) and 3 consecutive injections led to the overcoming of chemotherapy resistance. It was assumed that a treatment-related switch of the tumor microenvironment, which was initially insufficient for the pH-triggered drug release, induced the delayed tumor-response. While the **A***S*200Dox conjugate was increasingly accumulating in the tumor due to consecutive injections, doxorubicin was not cleaved efficiently but probably a small amount of released doxorubicin already induced some changes in the tumor microenvironment. When the changing milieu triggered the drug release of the strongly accumulated conjugate later, a very high doxorubicin amount was released within the tumor. This might have induced the subsequent tumor regression. Afterwards, it was checked whether the same treatment schedule induced a tumor regression in A2780cis tumor xenograft bearing mice as well. Here, besides a much more pronounced toxicity, also a tumor regression was observable but it seemed like the onset of tumor response occurred already after the second injection although the following injection was still needed to achieve a complete regression. It was concluded that despite similar substructures of the tumor xenografts, the microenvironment in the A2780cis tumors was different and more efficient for the pH-triggered drug release. Nevertheless, the quicker drug release probably also increased the toxic side effects. It was noticeable that despite the improved drug release a total dose of 25 mg/kg BW of doxorubicin must be delivered to the tumor to overcome the drug resistance.

It can be summarized that the **A***S*200Dox conjugate is a suitable system to overcome chemotherapy resistance, as it was possible to achieve complete tumor regressions in two multi-drug resistant tumor xenograft models. Furthermore, it can be noticed that the tumor response to the treatment is dependent on the respective tumor type. Further investigations regarding the influence of the applied treatment schedule, tumor microenvironment and the tumor type dependency were performed and will be described in the following sections.

3.3 Investigation of the underlying mechanism of action

3.3.1 Influence of the treatment schedule

For determining the influence of the applied treatment schedule on therapeutic success it was assessed, whether there was a specific total dose or number of injections that has to be administered to induce a tumor regression. Different treatment schedules were tested initially in 1411HP tumor xenograft bearing mice to disclose the impact of possible key parameters as number, interval and single dose of injections as well as the total dose within the therapy schedule.

The results revealed that an application of three 2-fold doses (10 mg/kg BW doxorubicin equivalent) on days 1, 4 and 9 resulted in the characteristic pattern of delayed but strong response, as observed in the initial trial (Fig. 38, B). Interestingly, treatment with 2-fold doses using the narrower interval on days 1, 3 and 5 resulted in no obvious differences in the pattern of response although it was expected that the tumor response might have started earlier, as the same total drug amount was already administered at day 5 instead of day 9. But tumor regression also started not before day 10 (Fig. 38, B).

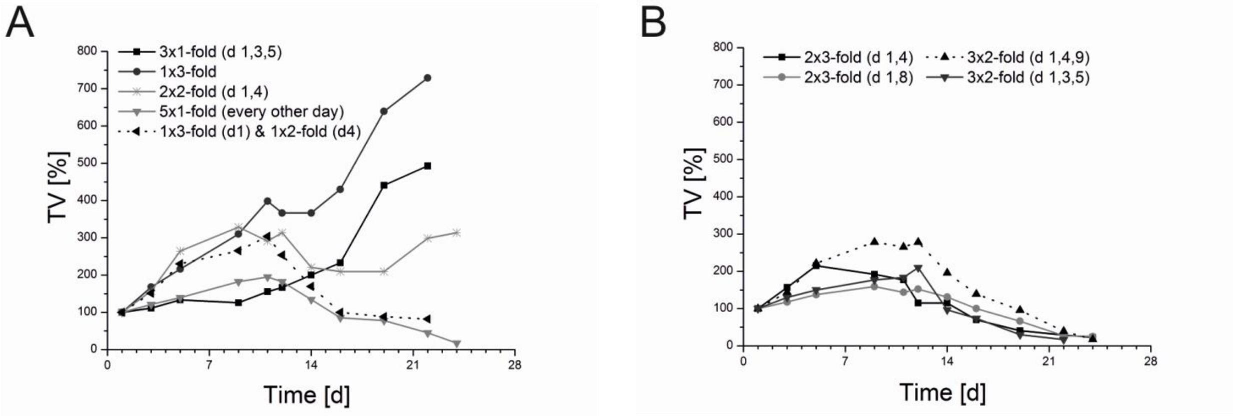

Fig. 38. Impact of treatment schedule and total dose on tumor response. Tumor volume (1411HP tumors) increase over time normalized to 1st day of treatment (d1). Different doses (A: 3- to 5-fold overall doxorubicin equivalent dose (each n=1); B: 6-fold overall doxorubicin equivalent dose (each n=1)) of **A***S*200Dox conjugate were administered in different time intervals (see legend). At least an overall dose of 5 to 6-fold doxorubicin equivalent dose of the pHPMA-doxorubicin conjugate was necessary to be administered within 10 days for achieving a tumor regression.

However, this schedule induced more toxic effects. Therefore, it exhibited no advantages compared to the treatment schedule with the longer interval. It was also very interesting to proof a possible necessity of a third injection for the achievement of a tumor response. The respective mice were treated only two times with 3-fold (15 mg/kg BW doxorubicin equivalent) doses on days 1 and 4 avoiding third injection while administering the same total drug dose. The process of clear tumor regression was observed again after day 10 independent of a third injection on day 9 (Fig. 38, B). This specific pattern could also be observed using a larger interval with injection of two 3-fold doses on days 1 and 8 (Fig. 38, B). Besides, this weekly treatment schedule seemed to be better tolerated. In a second set of treatments, the total dose was reduced. Application of an overall 5-fold dose, given as either 2 or 5 single injections, induced the characteristic pattern of response but total doses below that (3- & 4-fold total dose) resulted in an incomplete tumor response with early tumor regrowth after a first reaction (Fig. 38, A). These data suggest that the characteristic response of the resistant 1411HP tumors is not primarily dependent on dose interval but a sufficient high total dose (5- to 6-fold total dose) has to be administered within 10 days to induce a complete response.

Comparable examinations were performed in A2780cis tumor xenograft bearing mice. An application of a 5-fold total dose was sufficient to induce an effective response too, whereas 3- and 4-fold doses resulted in an incomplete tumor response (Fig. 39).

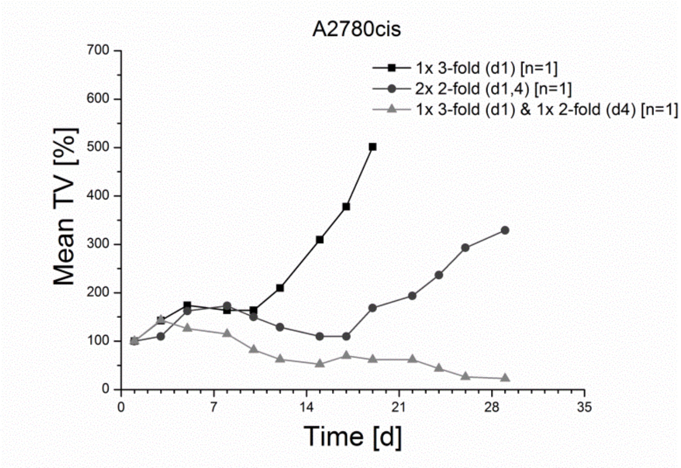

Fig. 39. A2780cis tumor volume (TV) increase normalized to day 1 over time. PBS control group (Means ± SD, n = 5) and doxorubicin therapy group (Means ± SD, n = 5). Mice received either PBS or doxorubicin (5 mg/kg BW) i.v. at day 1 and 4. Different treatments with the **A***S*200Dox conjugate are depicted (each n = 1). Treatment with doxorubicin induced only negligible growth retardations whereas application of a 5-fold total dose of the conjugate led to a complete regression.

Even the treatment with a single 3-fold dose had a clear improved impact on tumor growth inhibition compared to free doxorubicin treatment. The onset of response of A2780cis tumors was observed to be earlier compared to 1411HP tumors. This was already observed and shortly discussed in the previous trial, described in subsection 3.2.3.

Besides the immediate tumor response, increased toxic side effects, especially a loss of bodyweight, were observed again in A2780cis tumor xenograft bearing mice. Due to the increased toxicity, only lower total doses compared to 1411HP tumor xenograft bearing mice were tolerated. It was assumed that not only therapeutic success but also toxicity profiles were dependent on the particular tumor type. As already outlined in the section before, the higher toxicity observed in the A2780cis model might be associated with a more acidic microenvironment in these tumors. It can be suspected, that a very early release of doxorubicin, immediately after delivery of the conjugate in the tumor tissue, may lead to a partial re-circulation of doxorubicin. This would also contribute to the occurrence of systemic toxicity. Therefore, further investigations were made to corroborate this assumption.

3.3.2 Examination of increased Doxorubicin delivery to the tumor site

While the used pHPMA based drug delivery systems have shown improved tumor accumulation, it was further expected that the administration of higher doses of the conjugate also resulted in an increased doxorubicin accumulation within the tumor tissue. To prove this assumption, 1411HP tumor xenograft bearing mice were treated with free doxorubicin (5 mg/kg BW) and the **A***S*200Dox conjugate in the 1-fold, 2-fold or 3-fold doxorubicin equivalent dose. Due to the spectral properties of doxorubicin and the strong autofluorescence of living tissue within the blue wavelength range, an *in vivo* detection of doxorubicin was not possible. However, *ex vivo* examinations allowed the detection of doxorubicin and subtraction of the autofluorescence signal. The necropsied and cross-sectioned tumors were analyzed by msFI 48 h after i.v. injection to determine the doxorubicin fluorescence intensity. As shown in Fig. 40, even the 1-fold dose led to a clear improvement compared to free doxorubicin, which directly demonstrates the effect of the pHPMA-carrier. The application of increasing doses of pHPMA-doxorubicin conjugate resulted in stepwise increased doxorubicin derived signals, indicating an improved drug delivery (Fig. 40). Therefore, a very high local doxorubicin amount can be expected after the administration of an overall 5- to 6-fold dose in the previous study. It is imaginable that the release of this high amount could have been responsible for the overcoming of resistance in both tumor types.

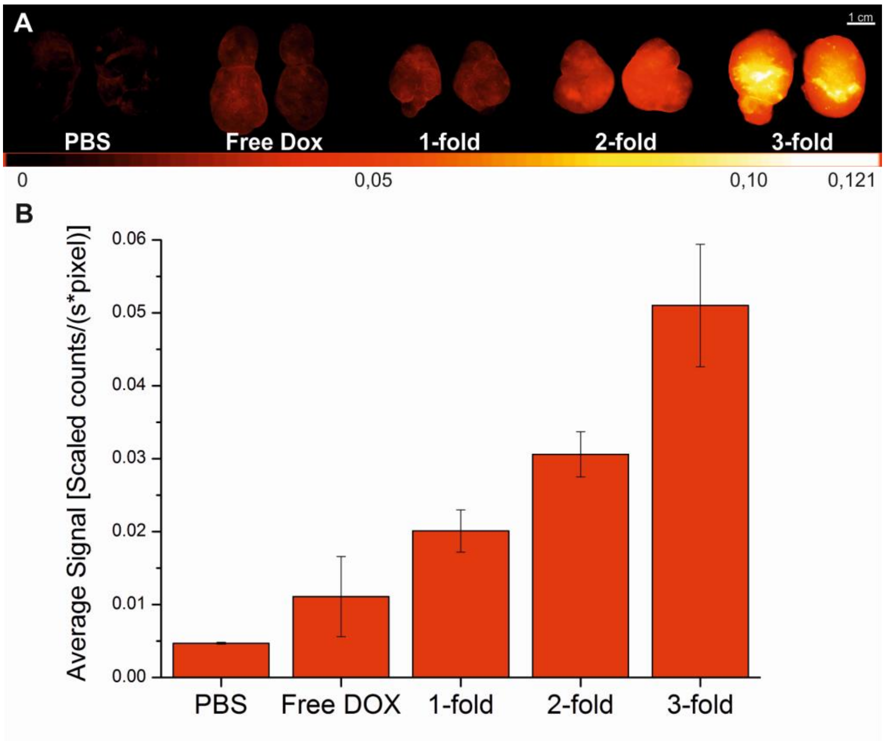

Fig. 40. Evaluation of intratumoral doxorubicin accumulation. (A) Fluorescence images of necropsied and cross sectioned 1411HP tumor xenografts 48 h after injection of either free doxorubicin (5 mg/kg BW), 1-, 2- and 3-fold doxorubicin equivalent dose of the **A***S*200Dox conjugate or PBS as a control. Dark red indicates low intensity whereas yellow/white indicates high fluorescence intensity (doxorubicin signal). Increasing dose led to increasing intratumoral doxorubicin accumulation.

(B) Bar plot of measured mean fluorescence intensities (FIs) of necropsied and cross sectioned 1411HP tumors (doxorubicin signal) of 2 trials (each group n=2). FIs were normalized by the tumor area and exposure time (Average signal [scaled counts/s*pixel]). Small black bars depict the range.

3.3.3 *In vitro* testing of pH-dependent cytotoxicity

Next studies were conducted to investigate a possible underlying mechanism of the differential delayed response to treatment with the **A***S*200Dox conjugate on cellular level. As it was important to determine the kinetics of the pH-dependent drug release and activation of the conjugate, it was pre-incubated for 24 h in buffers with different pH-values in a range of 5.5 to 7.4. Afterwards, it was used to prepare serial dilutions which were directly used for the cytotoxicity assays in comparison to free doxorubicin. In contrast to the cytotoxicity tests with free doxorubicin described in section 3.2.1, cells were incubated only 2 h instead of 96 h. As the cells within cell culture metabolize the nutritive ingredients, the pH of the culture medium shifts to lower values over time due to the secreted metabolites. In this case, the acidification of the medium would increase the pH-sensitive drug release uncontrolledly. Within 2 h, the pH of the used medium should be constant due to the contained bicarbonate buffering system.

As it is visible in the displayed dose-response curves (Fig. 41), a gradual lowering of the pH resulted in a stepwise increase of cytotoxicity. The pH-dependent pattern was observable in both cell lines 1411HP and A2780cis. Furthermore, comparable IC$_{50}$ values and a comparable shift in toxicity between the conjugate, which was incubated at pH 7.4, and free doxorubicin were observable. Thereby, the mechanism of pH-dependent drug release by the pHPMA-doxorubicin conjugate was confirmed and the comparable results led to the assumption that none of the tested cell lines exhibited a preferential cellular uptake of the conjugate or a higher sensitivity against the treatment.

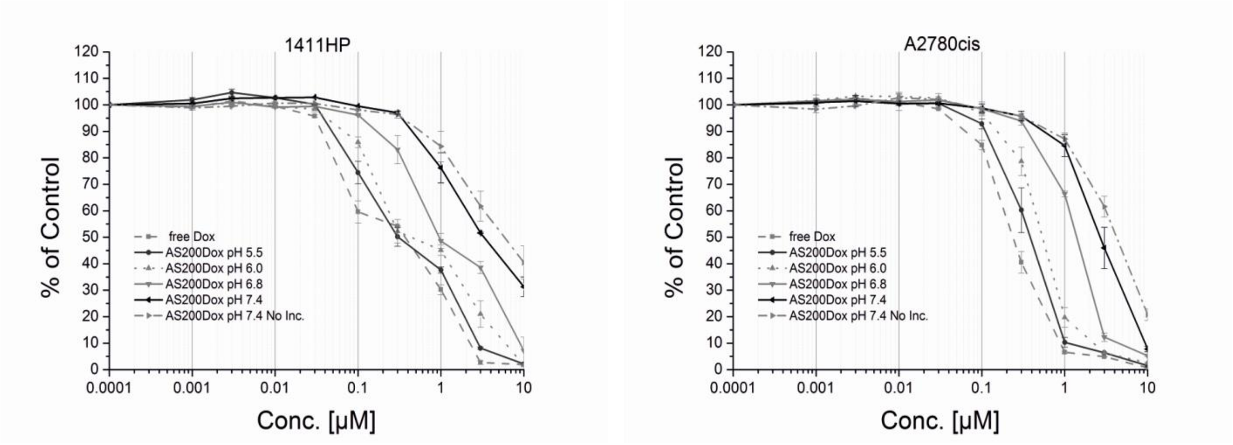

Fig. 41. Dose-response curves of 1411HP (left) and A2780cis (right) cell line determined after SRB-assay performance (Means ± range; n = 2) with pre-incubated (24 h) **A***S*200Dox conjugate in phosphate buffers with different pH values (5.5-7.4). Stepwise decrease of pH led to stepwise increase of cytotoxicity for both 1411HP and A2780cis cell line. A pH shift from 7.4 to 5.5 led to an approx. 10-fold lower IC$_{50}$. IC$_{50}$ values for free doxorubicin and pH 5.5 incubated **A***S*200Dox conjugate were comparable which indicated a nearly complete doxorubicin release from the polymer backbone at pH 5.5. Comparison of pre-incubated and non-incubated conjugate at pH 7.4 indicates a slight doxorubicin release at physiological pH.

Besides, the comparison of the non-incubated conjugate and the one which was pre-incubated for 24 h at pH 7.4 was performed to determine the stability of the hydrazone bond at physiological pH. As it can be seen in Fig. 41, the dose-response curve of the pre-incubated conjugate is slightly but reproducibly shifted to the left, indicating the release of a small amount of doxorubicin at pH 7.4 at 37 °C compared to the non-incubated conjugate. *In vivo*, this small amount of peripherally released doxorubicin could be responsible for toxic side effects. Although the released amount of doxorubicin at physiological pH is assumed to be negligible, it could be probably possible to avoid this peripheral release in future conjugates, as the stability of the bond could be increased by the use of special spacers in the vicinity of the hydrazone bond. A suitable spacer should stabilize the hydrazone bond at physiological pH during blood circulation but should allow an effective cleavage of the hydrazone bond under mild acidic conditions within tumor tissue. If the bond is too stable, the drug release is hampered, whereas a less stable bond might lead to peripheral release which can cause severe side effects and decreased drug accumulation at the tumor site. The influence of several spacers on the stability of the hydrazone bond was already investigated by Chytil *et al.* (52). The results revealed that the most promising spacers were doxorubicin itself, as it is used in the studies of this thesis, and a 4-oxo-4-(2-pyridyl)butanoyl (PYR) spacer. The latter exhibited increased stability at pH 7.4 *in vitro*. This is beneficial for avoiding peripheral drug release in case of *in vivo* application. Nevertheless, the drug release at mild acidic pH was decreased compared to doxorubicin which might hamper an effective drug release within the tumor. In case of the A2780cis tumor, one might consider choosing the PYR-spacer for future conjugates, as an enhanced stability at mild acidic pH might prevent the very early drug release from the conjugate in case of mice bearing this tumor xenograft. This would be beneficial for the toxicity profile and for the cellular uptake of the whole conjugate to overcome the multi-drug resistance.

In conclusion, a similar mechanism of a pH-dependent drug release from the pHPMA-doxorubicin conjugate was confirmed for both cell lines on cellular level. Therefore, it became much more obvious that rather xenograft specific characteristics must be responsible for the different tumor responses.

3.3.4 Tumor microenvironment studies by multispectral fluorescence imaging

Besides the proliferating tumor cells, the tumor microenvironment consists of several components such as tumor stroma, including the ECM, inflammatory cells, blood vessels and various associated tissue cells (82, 83). It is known that the microenvironment is designed and controlled by the tumor itself, as the tumor cells secrete several peptides such as growth factors and other enzymes which are necessary for tumor progress (83). There is a distinct heterogeneity of tumor microenvironments which can strongly influence the response to chemotherapeutic treatments (84). As the composition of the tumor microenvironment affects the tumor micromilieu regarding hypoxia and pH, it can be hypothesized that it strongly influences the pH-dependent drug release from the applied conjugate and thereby the therapeutic success. By the results of the therapy study, it was assumed that 1411HP tumors initially did not enable an efficient drug release due to inappropriate conditions of the tumor microenvironment. This might have led to the initial non-response, whereas the immediate tumor response of the A2780cis tumors might be attributable to a more advantageous micromilieu. To prove this assumption, tumor microenvironment studies were performed. Obviously, the most reasonable parameter to measure would have been the pH but unfortunately no adequate dyes for the non-invasive msFI measurement of the intratumoral pH were obtainable. Some commercially available dyes can be used for *in vivo* pH measurements but previous experiments in our laboratory have shown that the spectral properties of the respective dyes were inappropriate for a reliable evaluation of tumor pH *in vivo*. Therefore, hypoxia was chosen as a parameter of interest, which is also closely connected with the acidification of the tumor microenvironment.

As the onset of noticeable tumor response of the 1411HP tumor xenografts always occurred around day 10, a procedure was developed to investigate the microenvironment before and after an observed tumor response. For the characterization of the tumor microenvironment regarding hypoxia, the fluorescent imaging agent Hypoxisense® was used. It is targeted to carbonic anhydrase IX (CA IX) which is known to be overexpressed by cells due to local hypoxia (79, 85). Insufficient oxygen supply through the tumor mass due to poorly developed and defective tumor vasculature leads to the development of hypoxic areas within a solid tumor. In response to local hypoxia, the hypoxia-inducible factor 1-α (HIF-1-α) is upregulated, which leads to increased expression of CA IX (86). CA IX itself catalyzes the reversible dehydration of bicarbonate. While intracellular carbonic anhydrases (CAs) can convert intracellular hydrogen carbonate to carbon dioxide (CO_2) and water, the CO_2 can be reconverted after diffusion through the plasma membrane by extracellular CAs, such as CA IX (85). Thereby produced protons contribute to the acidification of the extracellular compartment of tumor tissue (87). Furthermore, the presence of hypoxia induces anaerobic glycolysis, which leads to the excessive production of lactic acid. Its removal is strongly impaired due to the poorly developed tumor vasculature. Consequently, the accumulation of lactic acid also contributes to the acidification of the tumor microenvironment. Thus, it appears that tumor hypoxia is beneficial for a pH-sensitive drug release from the applied pHPMA-doxorubicin conjugate. As cancer cells exhibit the ability to convert glucose to lactic acid even in the presence of oxygen, commonly known as Warburg effect, (68, 88, 89) it is obvious that hypoxia is not absolutely necessary for an acidic tumor microenvironment. However, it is undoubted that the presence of hypoxia can reinforce the acidification of the tumor microenvironment.

The evidence of hypoxia could be visualized by fluorescence imaging after previous injection of Hypoxisense® to the respective mouse. Unfortunately, the spectral properties of this imaging agent allowed no reliable *in vivo* detection of the fluorescence signal but it was possible to gather information about the presence of hypoxia within the tumor xenografts by *ex vivo* examinations of the necropsied tumors.

First, normal growing and untreated 1411HP tumors were tested. Therefore, an untreated control tumor, without previous Hypoxisense® injection, was examined by msFI within the same wavelength range as the Hypoxisense®-treated tumors. As it was expected, nearly no fluorescence signal was detected within this tumor (Fig. 42).

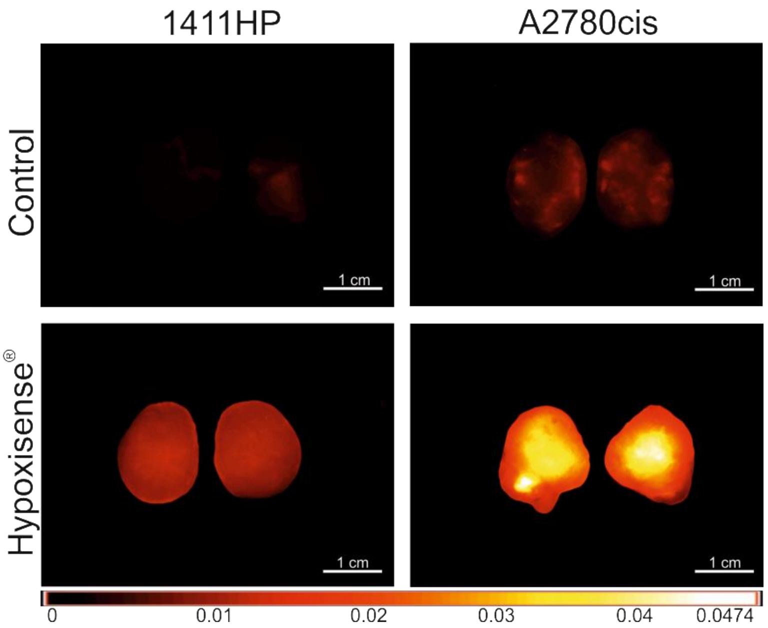

Fig. 42. Fluorescence images of excised and cross-sectioned 1411HP and A2780cis tumors. The mice with control tumors received no treatment whereas the other mice were previously treated with Hypoxisense®. The control tumors exhibited negligible fluorescence intensity within the chosen wavelength range. In comparison to the respective control only a slight Hypoxisense® accumulation was visible in case of the 1411HP tumor while the A2780cis tumor exhibited a strong accumulation of the hypoxia indicating agent.

Now, 1411HP tumor bearing mice were treated with an i.v. injection of 100 µl Hypoxisense®. 24 h after injection the mice were sacrificed, tumors necropsied, cross-sectioned and examined by msFI. Only a very low accumulation of the imaging agent was detectable in the tumors (Fig. 43, A, upper example). Therefore, a lack of distinct hypoxia can be assumed for this tumor xenograft type, at least when mice received no chemotherapeutic treatment. Then, 1411HP tumor bearing mice were treated with the **A***S*200Dox conjugate which was also used in the therapy studies and in a second experiment, with the fluorescently labeled pHPMA-doxorubicin conjugate **A***S*190DoxF (polymer backbone was additionally stably labeled with the NIR dye DY-782) to be able to track polymer accumulation independent of the doxorubicin signal. In each experiment, one treatment schedule included an injection of a 3-fold dose of the conjugate (15 mg/kg BW doxorubicin equivalent) on day 1 followed by an injection of Hypoxisense® on day 4 after a lacking tumor response was confirmed. The second schedule comprised treatments with 3-fold doses of the conjugate on days 1 and 4 followed by the application of Hypoxisense® on day 9 after the confirmation of first signs of tumor response. As shown in Fig. 43, only the responding tumors (two 3-fold injections) exhibited a clear accumulation of the hypoxia indicating agent, whereas the tumors which were treated only with a single injection still showed no accumulation.

These analyses clearly showed that an alteration of the tumor microenvironment has occurred at a time when the tumor regression process typically starts but not much earlier. Furthermore, a clear increased intratumoral content of the **A***S*190DoxF conjugate after treatments with two 3-fold doses was confirmed which was indicated by both, the doxorubicin- and the polymer-derived signal (Fig. 43, C, lower panels). In addition, a composite analysis of single signals was performed to visualize the localization of the single components. As shown in Fig. 43 C (upper panel), signals of doxorubicin and Hypoxisense® were closely related and most prominent in the responding tumor. A clear polymer-derived signal was observed at the rim of tumors (colored in green), which indicated the **A***S*190DoxF conjugate after the release of doxorubicin. These findings corroborate the assumption of an initial inappropriate tumor microenvironment for the pH-triggered doxorubicin release in the 1411HP model. It is assumable that a therapy associated switch to a more advantageous microenvironment led to the release of a high amount of doxorubicin from the strongly accumulated conjugate.

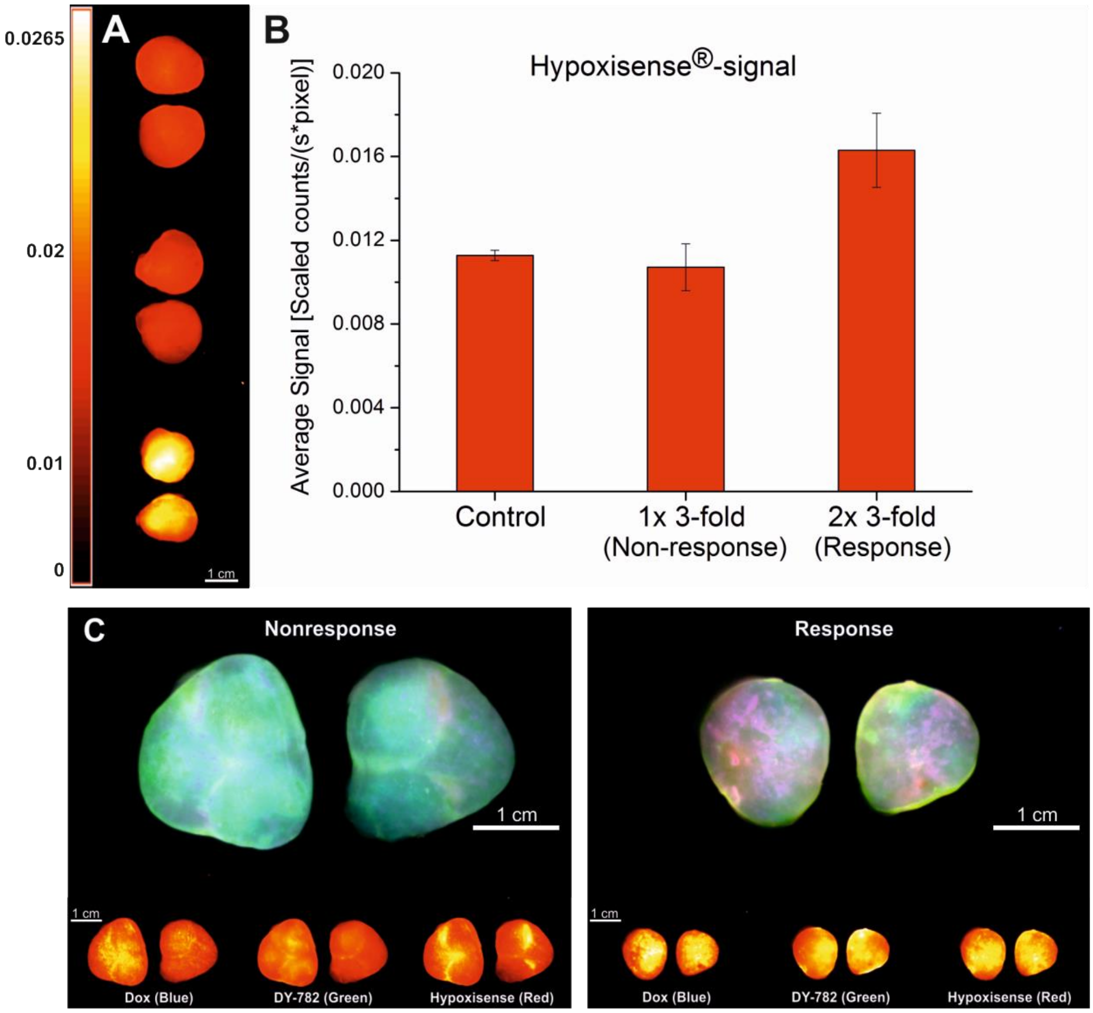
0.0265
0.02
0.01
0
A
1 cm
B
Hypoxisense®-signal
Average Signal [Scaled counts/(s*pixel)]
0.020
0.016
0.012
0.008
0.004
0.000
Control
1x 3-fold (Non-response)
2x 3-fold (Response)
C
Nonresponse
1 cm
1 cm
Dox (Blue)
DY-782 (Green)
Hypoxisense (Red)
Response
1 cm
1 cm
Dox (Blue)
DY-782 (Green)
Hypoxisense (Red)

Fig. 43. (A) Fluorescence images of necropsied and cross sectioned 1411HP tumors. Mice received either only Hypoxisense® as a control (upper sample) or 3-fold doxorubicin equivalent dose of the **A**S200Dox conjugate once (non-responding tumor, middle sample) or twice (d1 and d4, responding tumor, lower sample) with following Hypoxisense® injection. Dark red indicates low intensity whereas yellow/white indicates high FI (Hypoxisense® signal). Clear accumulation of Hypoxisense® can only be detected in the tumor that showed a therapy response.

(B) Bar plot of mean FIs (Hypoxisense® signal) of samples (1411HP tumors) shown in A and C (lower panel) after i.v. administration of the **A**S200Dox conjugate and the **A**S190DoxF, respectively, with following Hypoxisense® injection. FIs were normalized by tumor area and exposure time. Small black bars: standard deviation.

(C) Composite image (upper panel) of single signals (lower panels). Certain colors were allocated to the single signals. Signal overlay led to mixed colors. A clear increased intratumoral content of the **A**S190DoxF conjugate after treatment with two 3-fold doses was confirmed which was indicated by both, the doxorubicin- & the polymer-derived signal. An increased intensity of Hypoxisense® signal was observable in the responding 1411HP tumor. A polymer-derived signal was detectable at the rim of the responding 1411HP tumors indicating the pHPMA conjugate after release of doxorubicin.

Interestingly, a therapy induced hypoxia when using HPMA-copolymers was already described. Minko *et al.* ascribed this effect to the downregulation of vascular endothelial growth factor (VEGF) gene expression, induced by the HPMA-copolymer doxorubicin conjugate (33). This could be one possible explanation for the phenomenon of the reproducible, time and treatment related effect observed in the 1411HP model.

Over time also small amounts of released doxorubicin could have induced apoptosis and the development of necrotic areas. Within these areas, a hypoxic and acidified milieu can be assumed, which would trigger an enhanced doxorubicin release from the accumulated polymer. This could have led to a kind of chain reaction which might have finally contributed to the observed tumor regression.

Additionally, analyses of the microenvironment of A2780cis tumors in comparison to 1411HP were performed by the use of Hypoxisense®.

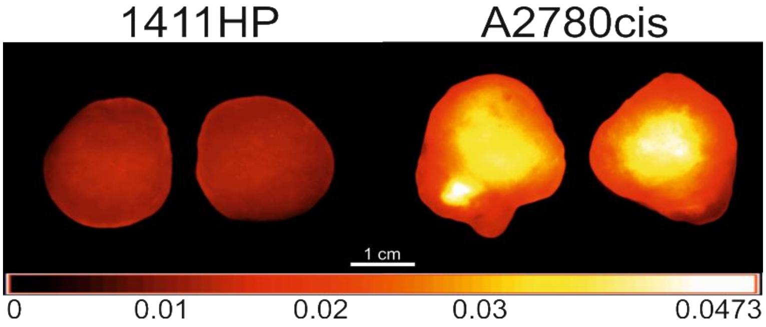

Fig. 44. Typical fluorescence image of necropsied and cross-sectioned 1411HP and A2780cis tumor which received no previous chemotherapeutic treatment. Images were acquired 24 h after Hypoxisense® injection. Dark red indicates low intensity whereas yellow/white indicates high FI. Clear accumulation of Hypoxisense® was observable in A2780cis tumors indicating a hypoxic microenvironment whereas 1411HP shows nearly no accumulation of the imaging agent indicating a lack of hypoxia.

A2780cis tumor bearing mice received a Hypoxisense® injection without any other previous treatment. 24 h later they were sacrificed and tumors were examined by msFI (Control tumor is displayed in Fig. 42). It was observable that untreated A2780cis tumors showed a much higher accumulation of the hypoxia indicating agent compared to untreated 1411HP tumors. Thereby, a more hypoxic microenvironment can be assumed (Fig. 44). These analyses revealed that A2780cis tumors are characterized by a more supporting microenvironment which probably accelerates the pH-dependent release of doxorubicin from the conjugate. This might have led to an earlier tumor response but also in increased side effects, due to the very early doxorubicin release before cell internalization. The recirculation of the released doxorubicin could be responsible for the remarkable lower tolerability of the pHPMA-doxorubicin conjugate in A2780cis tumor bearing mice compared to 1411HP-tumor bearing mice. These interesting results were a first hint on the way to find an explanation for the tumor-type dependent efficacy of the pHPMA-doxorubicin conjugate.

3.3.5 Further investigations of a tumor-type-dependency

The gathered results of the performed experiments already indicated a tumor-type-dependency regarding the efficacy of the pHPMA-doxorubicin conjugate treatment. To corroborate this assumption, another, structurally completely different, tumor type was examined. The multi-drug resistant human colon-carcinoma cell line HT-29 is structurally characterized by sparse vascularization and a high amount of ECM, which is a complex network of glycoproteins, proteoglycans, polysaccharides and several proteins such as collagen (84, 90). Furthermore HT-29 xenografts are characterized by the existence of abundant necrotic and fibrotic regions. The existence of large necrotic regions and the sparse vascularization of this xenograft model were supposed to create a more hypoxic and acidic microenvironment compared to the 1411HP and A2780cis tumor. The high amount of ECM within this tumor xenograft may represent a barrier for therapeutic agents, which might contribute to the drug resistance (84).

Besides HT-29, also another multi-drug resistant human colon-carcinoma cell line, DLD-1, was tested regarding the tumor microenvironment. DLD-1 is structurally comparable to HT-29 but the necrotic and fibrotic regions are much more pronounced here.

The imaging agent Hypoxisense® was used again to determine the presence of hypoxia within these tumor types, especially in comparison with the 1411HP and A2780cis tumor xenografts. Similar to the experiments in subsection 3.3.4, the HT-29 and DLD-1 tumor bearing mice received an i.v. injection of Hypoxisense® 24 h before they were sacrificed. The msFI analysis of the necropsied tumors revealed the existence of a hypoxic microenvironment within both colon-carcinoma xenograft models. While the HT-29 tumor showed a very strong accumulation of the hypoxia indicating agent, the accumulation of Hypoxisense® was lower in DLD-1 but still higher compared to 1411HP and A2780cis. This became much more obvious when they were compared directly as displayed in Fig. 45. As the HT-29 tumor type seemed to differ much more from A2780cis and 1411HP regarding its tumor microenvironment than DLD-1, it was focused on this colon-carcinoma cell line for the further comparative tumor-type-dependency examinations.

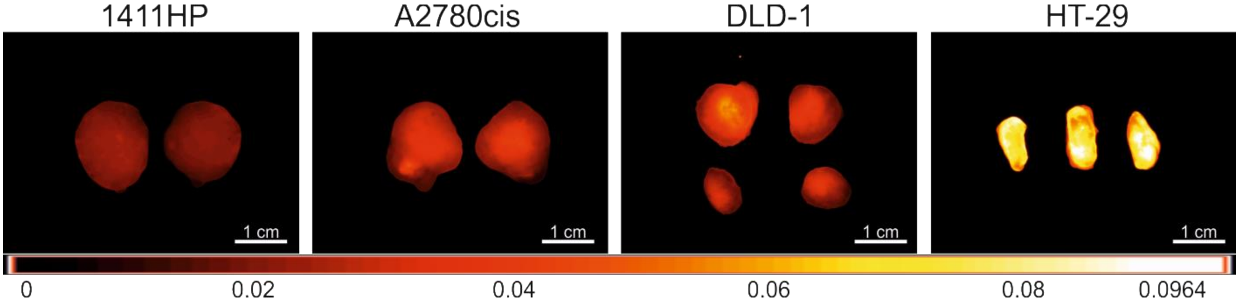

Fig. 45. Fluorescence image of necropsied and cross-sectioned 1411HP, A2780cis, DLD-1 and HT-29 tumor xenografts without any previous chemotherapeutic treatment but 24 h after Hypoxisense® injection. While 1411HP tumors showed nearly no accumulation of the hypoxia indicating agent, the A2780cis and DLD-1 tumors exhibited increased fluorescence intensities. A more hypoxic tumor microenvironment is assumable. The highest fluorescence intensity was measured in HT-29 tumors indicating a comparatively extreme hypoxic tumor microenvironment.

With the aim to reveal the underlying mechanism of the tumor-type-dependency, cytotoxicity tests with the **A***S*200Dox conjugate, which was pre-incubated in buffers of different pH similar to the experiments in subsection 3.3.3, were performed for the HT-29 cell line as well. Again, the pH-dependent pattern was observable for the dose-response curves, similar to the results for 1411HP and A2780cis (Fig. 46, A). Thereby, the mechanism of pH-dependent drug release by the **A***S*200Dox conjugate was confirmed also for HT-29 and the comparable results indicated no preferential cellular uptake of the conjugate or a higher sensitivity against the treatment compared to 1411HP and A2780cis.

For the comparative determination of efficacy 1411HP, A2780cis and HT-29 tumor bearing mice were treated with the pHPMA-doxorubicin conjugate. To ensure the application of the same total dose, a fixed dose schedule was used for all mice which consisted of two single injections (day 1 & 4) of the 2-fold dose of the conjugate (10 mg/kg BW doxorubicin equivalent). Although it was already known from the previous experiments that a total dose of 4-fold doxorubicin equivalent is not sufficient to induce a complete tumor regression in 1411HP and A2780cis tumors, higher total dose were avoided, as increased toxic side effects were expected for the HT-29 tumor bearing mice due to the even more advantageous microenvironment of these tumors compared to A2780cis. As expected, the 1411HP tumor grew continuously and no tumor response was observable.

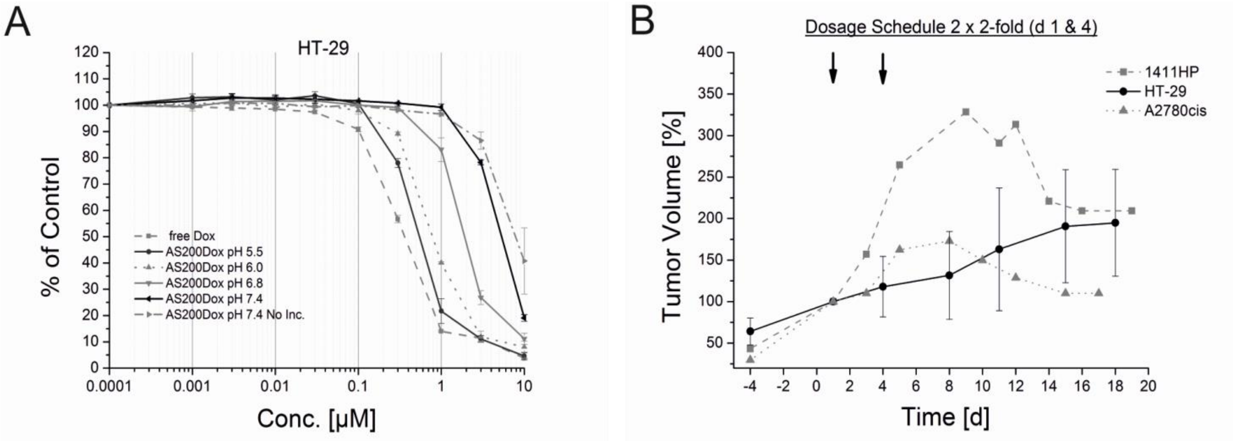

Fig. 46. (A) Dose-response curves of HT-29 cell line determined after SRB-assay performance (Means ± range, n = 2) with pre-incubated (24 h) **A***S*200Dox conjugate in phosphate buffers with different pH values (5.5-7.4). Stepwise decrease of pH led to stepwise increase of cytotoxicity. A pH shift from 7.4 to 5.5 led to an approx. 10-fold lower IC_{50}. IC_{50} values for free doxorubicin and pH 5.5 incubated **A***S*200Dox were almost comparable, which indicated a nearly complete doxorubicin release from the polymer backbone at pH 5.5. Comparison of pre-incubated and non-incubated conjugate at pH 7.4 indicated a slight doxorubicin release at physiological pH.

(B) Tumor volume over time normalized to 1^{st} day of treatment (d1). HT-29 tumor xenograft bearing mice (Means ± SD, n = 3) received respectively 2 injections (d1 & d4) of the 2-fold doxorubicin equivalent dose (10 mg/kg BW) of **A***S*200Dox conjugate. Representative curves of 1411HP and A2780cis tumor xenograft bearing mice (each n=1) which received the same treatment, were taken from the results of chapter 3.3.1 and are displayed for an improved comparison to HT-29. The same treatment schedule led to a different tumor response depending on the tumor type. Arrows point to treatments.

In contrast, the other two tumor types showed an immediate response, already after the first injection (Fig. 46, B). This indicated an early doxorubicin release in these tumors, while the release in the 1411HP tumor seemed to be insufficient, which was already expected from the previous experiments. Nevertheless, over time also differences between A2780cis and HT-29 became apparent. While the A2780cis tumor started to regrow continuously after the second injection, the HT-29 tumor growth was still inhibited. However, when the treatment was stopped (after the 2^{nd} injection) the tumor started to regrow (Fig. 46, B). It was assumed that the amount of the released doxorubicin was not sufficient to overcome the resistance and achieve a tumor regression, although the tumor microenvironment seemed to be very suitable for the pH-dependent release of the drug, at least in HT-29 and A2780cis. Besides, it became obvious that the HT-29 tumor bearing mice showed increased signs of toxicity, especially bodyweight loss, under the treatment with the **A***S*200Dox conjugate. This was already expected, as an advantageous microenvironment seemed to decrease the tolerability of the mice against the treatment due to a very early drug release. This was already observed for A2780cis compared to 1411HP. Consequently, no higher total doses could be administered to HT-29 tumor bearing mice. Therefore, no tumor regression was achieved with the applied treatment schedule. Considering these results, it became apparent that a very hypoxic tumor micromilieu is not necessarily advantageous for the therapy outcome and the toxicity profile, although it contributes to an efficient pH-dependent drug release. To confirm a tumor type dependent mechanism, it was important to enlighten the underlying mechanisms of action of the drug release. Therefore, msFM examinations were conducted.

3.3.6 Multispectral fluorescence microscopy of fixed cancer cell monolayers

MsFM is based on the same concept as msFI but allows the examination on cellular level within fixed cell monolayers or tissue sections. Because of the multispectral measurement, several dyes can be detected simultaneously, analogous to msFI.

An initial experiment was performed to determine whether the distribution of pHPMA-bound doxorubicin is more homogenous compared to free doxorubicin within cultured multi-drug resistant colon-carcinoma cells (DLD-1). After 24 h incubation with free doxorubicin (3 µM) or **A***S*200Dox conjugate (3 µM doxorubicin equivalent concentration), the fixed cells were examined. The intrinsic fluorescence of doxorubicin allowed its detection by msFM. The comparison of the fluorescence images showed a very inhomogeneous doxorubicin distribution in case of the free doxorubicin (Fig. 47). Some cells showed very strong fluorescence intensities especially within the cell nuclei, indicating the successful DNA intercalation of doxorubicin. In contrast, some cells appeared comparatively dark indicating lacking doxorubicin accumulation. The incubation with pHPMA-doxorubicin instead, resulted in a very homogenous distribution of doxorubicin. It was mainly detectable within the cell nuclei. However, the total fluorescence intensity was slightly lower compared to the free doxorubicin (Fig. 47). To improve the visualization, the brightness was adjusted (scale factor: 4). It has been reported, that the fluorescence intensity of doxorubicin is decreased when it is bound to the polymer backbone (91). Although doxorubicin will be released over time, it is likely that after the chosen incubation time a certain amount was still bound to the HPMA copolymer. Besides other resistance mechanisms, the DLD-1 cell line expresses MDR-1 (92), an efflux pump for e.g. chemotherapeutic agents. Therefore, free doxorubicin was expected to be pumped out of at least some cells, resulting in the inhomogeneous distribution of doxorubicin.

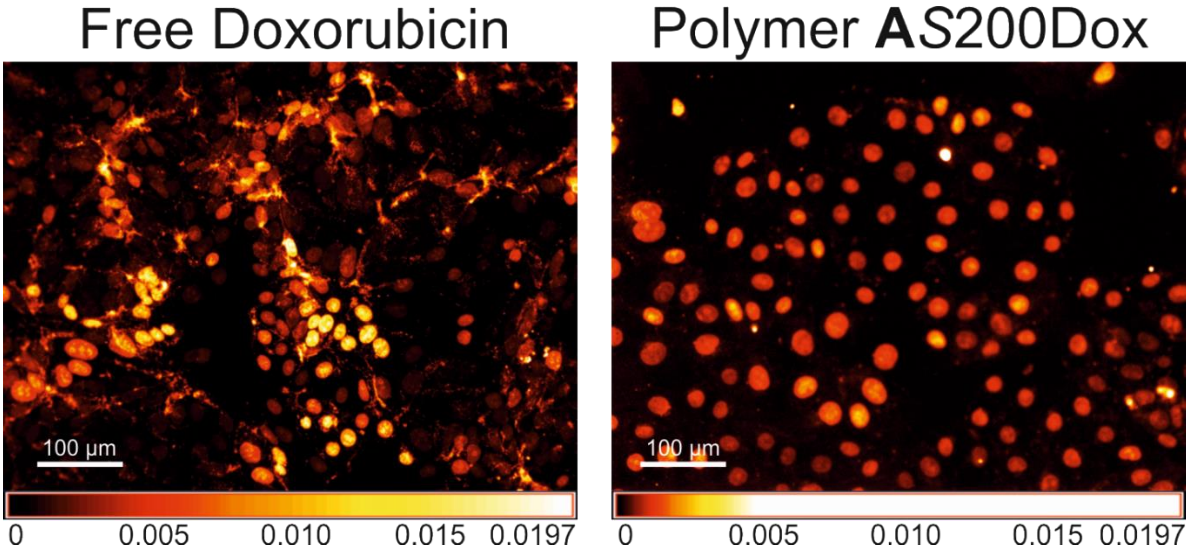

Fig. 47. MsFM images of fixed DLD-1 cells after a 24 h incubation with either free doxorubicin (3 µM) or **A***S*200Dox conjugate (3 µM doxorubicin equivalent concentration). Highest doxorubicin signal intensity was found in the cell nuclei but it was also detectable in the cytoplasm. The doxorubicin distribution was much more homogeneous in case of the **A***S*200Dox conjugate.

In case of the **A***S*200Dox conjugate the whole conjugate is assumed to be internalized via endocytosis, followed by a lysosomal uptake and pH-triggered drug release. Thereby, the efflux pump mediated drug resistance can be prevented, resulting in the more homogenous doxorubicin distribution within the cell monolayer. These results corroborate the assumed mechanism of the cellular uptake and drug release for the pHPMA-doxorubicin conjugate, at least for this cell line. Furthermore, the clear superiority of the pHPMA-bound doxorubicin compared to free doxorubicin was shown on a cellular level.

In the field of fluorescence microscopy, a variety of staining methods exists. Thereby, different cell compartments can be visualized, enabling a better orientation and improved localization of the signal of interest. One common method is the fluorescence staining with 4',6-Diamidin-2-phenylindol (DAPI). DAPI binds to A-T rich regions in the DNA. Therefore, it represents an excellent tool to stain the cell nuclei. When excited with UV light, the stained cell nuclei appear in light blue. Initially, it was checked if this staining method can be applied for further trials. This time, 1411HP cells were cultivated in chamberslides and incubated either with doxorubicin (3 µM) or with pHPMA-doxorubicin (3 µM doxorubicin equivalent concentration) for 7 h. After the DAPI staining, the fixed cells were examined. In Fig. 48 it can be seen that in case of previous free doxorubicin incubation the DAPI staining was not successful. The cell nuclei remained dark when excited with UV light but exhibited a strong doxorubicin signal when excited with blue light. This was different for the **A***S*200Dox conjugate.

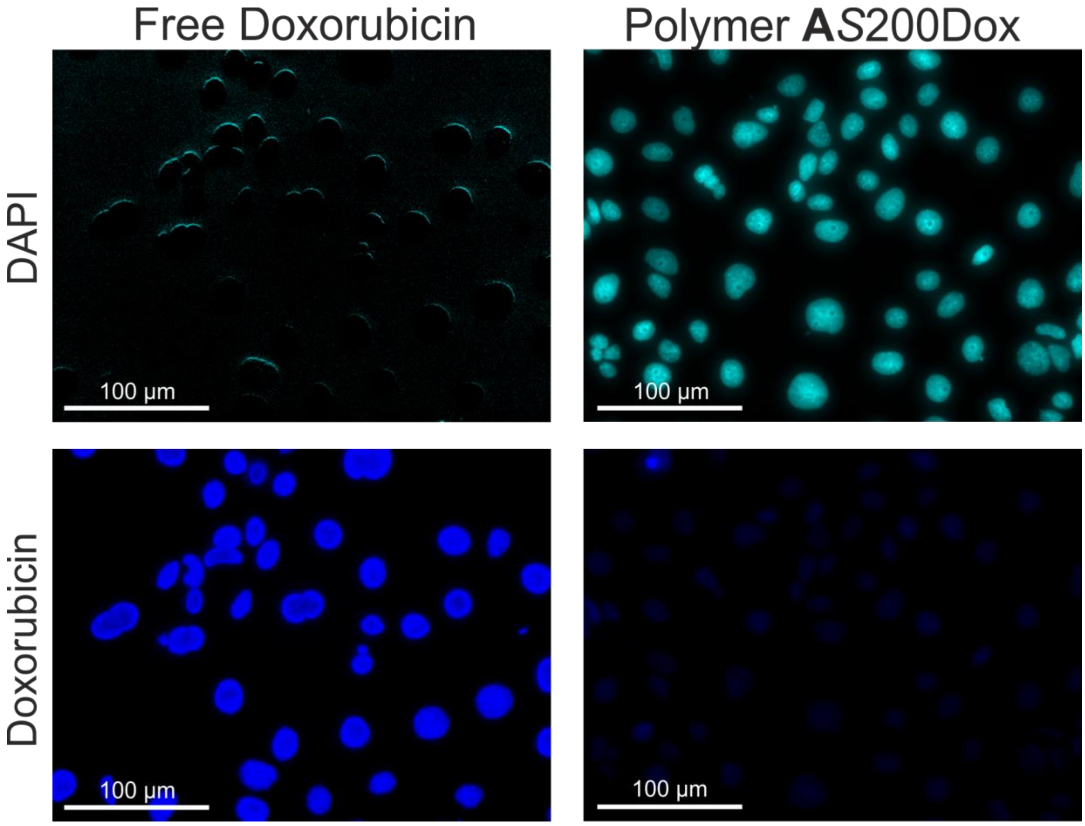

Fig. 48. MsFM images of fixed 1411HP cells after a 7 h incubation with either free doxorubicin (3 µM) or **A***S*200Dox conjugate (3 µM doxorubicin equivalent concentration). Cells were stained with DAPI to visualize the cell nuclei. In case of the free doxorubicin treatment, no DAPI signal could have been detected, while the doxorubicin signal within the cell nuclei was very intense. In case of **A***S*200Dox treatment, the doxorubicin signal intensity within the cell nuclei was low due to lacking doxorubicin release within the short incubation time. Here, DAPI staining of the cell nuclei was detectable.

Here, only a faint doxorubicin signal was detectable, whereas the fluorescence intensity of DAPI was comparatively intense. A strong interference between DAPI and doxorubicin can be concluded. Considering the fact that DAPI binds the DNA, it became obvious that the DNA intercalation of doxorubicin affects the DAPI staining or at least the signal extraction. Distinct quenching effects due to the coincident DNA intercalation of doxorubicin and DAPI might have led to the failed staining. While free doxorubicin quickly entered the cell nuclei, followed by its DNA intercalation, it can be assumed that in case of the pHPMA-bound doxorubicin, the pH-dependent drug release within this short incubation time was not sufficient to achieve extensive accumulation of doxorubicin within the cell nuclei. Therefore, the signal extraction of DAPI was still successful in this case. Nevertheless, it can be expected that a longer incubation time and a more efficient drug release would lead to the same problem as in case of free doxorubicin incubation.

Taking these important results into account, no DAPI staining was performed for further experiments with doxorubicin and pHPMA-doxorubicin. However, in the following experiments the orientation within the cell monolayer was improved by staining the cytoskeleton with Alexa Fluor® 488 Phalloidin.

After these preliminary trials, it was of great interest to visualize the fate of both the polymeric carrier and the drug on cellular level, to determine the underlying mechanism of cellular uptake for the different cell lines. It was presumed, that the different tumor response to the pHPMA-doxorubicin treatment was caused by xenograft specific characteristics such as tumor microenvironment and not by a different release mechanism on cellular level. To verify this hypothesis, cell monolayers of the respective cell lines were examined initially. For this purpose, another pHPMA-doxorubicin conjugate was used. As the amount (0.46 % wt.) of the usually applied polymer label (DY-782) was too low for the fluorescence microscopic detection and a higher labeling was not possible due to resulting quenching effects, CY-7 (NIR dye) was chosen as a covalently bound polymer label. Thereby, it was possible to load the polymer with 0.76 % wt. of the dye without noticeable quenching effects. Fortunately, this allowed the fluorescence microscopic detection. To exclude an influence of the new dye on the cellular uptake of the conjugate, or any other interference, the comparable behavior of the pHPMA-doxorubicin conjugate with CY-7 (**A***S*180DoxF) was confirmed by *in vitro* cytotoxicity assays similar to the *in vitro* trial conducted with the previous conjugate described in subsection 3.3.3. The results are displayed in Fig. 49. Stepwise decrease of pH led again to a stepwise increase of cytotoxicity.

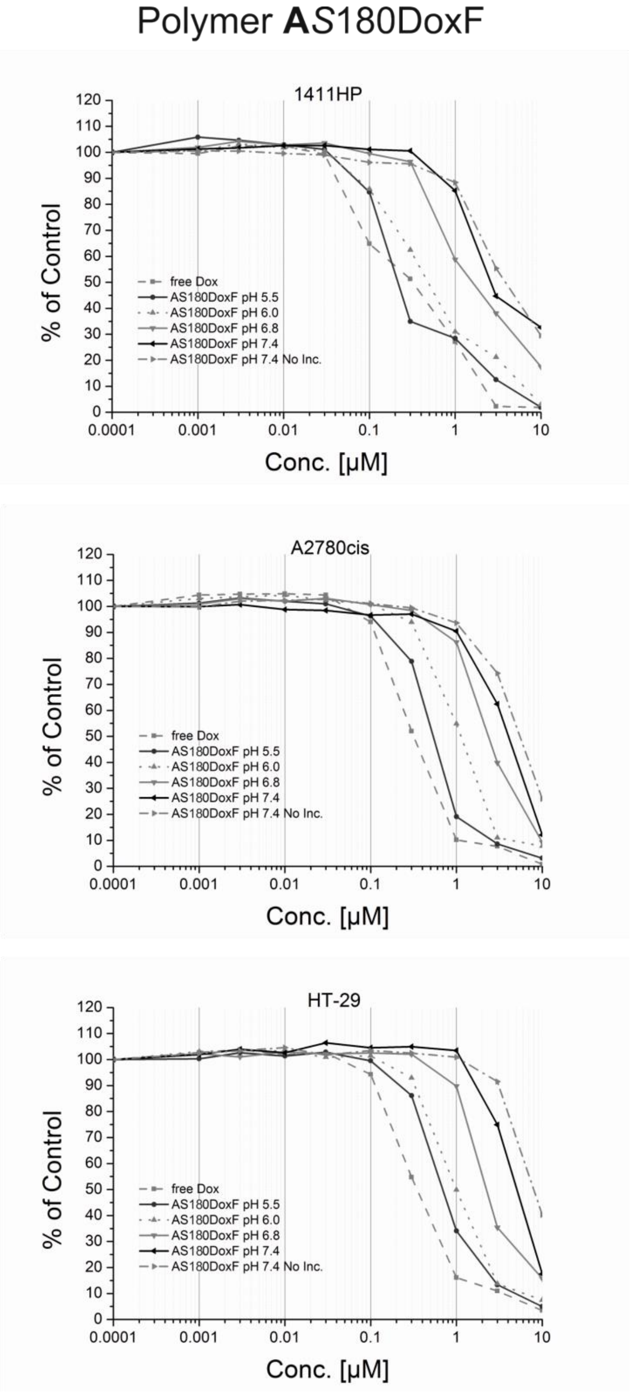

Fig. 49. Dose-response curves of 1411HP, A2780cis and HT-29 cell line determined after SRB-assay performance (n = 1) with the **A***S*180DoxF conjugate pre-incubated (24 h) in phosphate buffers with different pH values (5.5-7.4). Stepwise decrease of pH led to stepwise increase of cytotoxicity for all three cell lines. A pH shift from 7.4 to 5.5 led to an approx. 10-fold lower IC_{50}. IC_{50} values for free doxorubicin and pH 5.5 incubated **A***S*180DoxF conjugate were comparable which indicated a nearly complete doxorubicin release from the polymer backbone at pH 5.5. Comparison of pre-incubated and non-incubated conjugate at pH 7.4 indicates a slight doxorubicin release at physiological pH. These results were comparable with the **A***S*200Dox conjugate of the previous trials and confirmed similar *in vitro* behavior.

As this pH-dependent pattern and the IC_{50} values were comparable to the previous cytotoxicity trials, the new conjugate was considered as suitable for the microscopic investigations.

For the fluorescence microscopic examination the cells (1411HP, A2780cis and HT-29) were seeded and cultivated in chamberslides. They were incubated with the **A***S*180DoxF conjugate (equivalent to a doxorubicin concentration of 30 µM) for 8 h. A longer incubation time was not possible, as the cytotoxic effects of this comparatively high dose would induce cell death, allowing no further investigations of the localization of the conjugate and doxorubicin. However, lower doses were not acceptable due to the still low fluorescence intensity of the polymer label. By msFM it was possible to detect the fluorescence signal of doxorubicin, polymer (CY-7) and the cytoskeleton, which was stained with Alexa Fluor® 488 Phalloidin, simultaneously. Thereby, composite images were created allowing the localization of all three components. The results are displayed in Fig. 50. Here, the cytoskeleton signal was colored green, the doxorubicin signal blue and the polymer signal red. Interestingly, the distribution patterns of the polymer and doxorubicin were comparable in all three cell lines, although the cell lines exhibited a different morphological structure. A doxorubicin derived signal was visible in the cell nuclei, indicating a successful drug release from the polymer backbone and subsequent intercalation in the cellular DNA (Fig. 50). The polymer was locatable in the cytoplasm and mainly localized near the nuclear membrane. Besides, also purple regions were visible in some cells indicating the intact pHPMA-doxorubicin conjugate (Fig. 51). Previous studies have shown that the cell internalization of pHPMA-conjugates usually happens via endocytosis. After the fusion with lysosomes, the acidic pH in the lysosomal compartment leads to the rapid cleavage of the hydrazone bond and the release of doxorubicin. For HPMA copolymers with M_w below 25 kDa an endosomal escape with subsequent distribution into the cytoplasm or nucleus after a certain time period has been described (93, 94). Usually conjugates with increased M_w, such as the applied 200 kDa conjugate, should be excluded from the nuclei.

Nevertheless, during microscopic examinations also minor violet nuclei were observed, indicating the presence of the intact pHPMA-doxorubicin conjugate (Fig. 51). On the one hand, this might be a result of an overlapping of the fluorescence signals, as a three-dimensional structure is displayed two-dimensional.

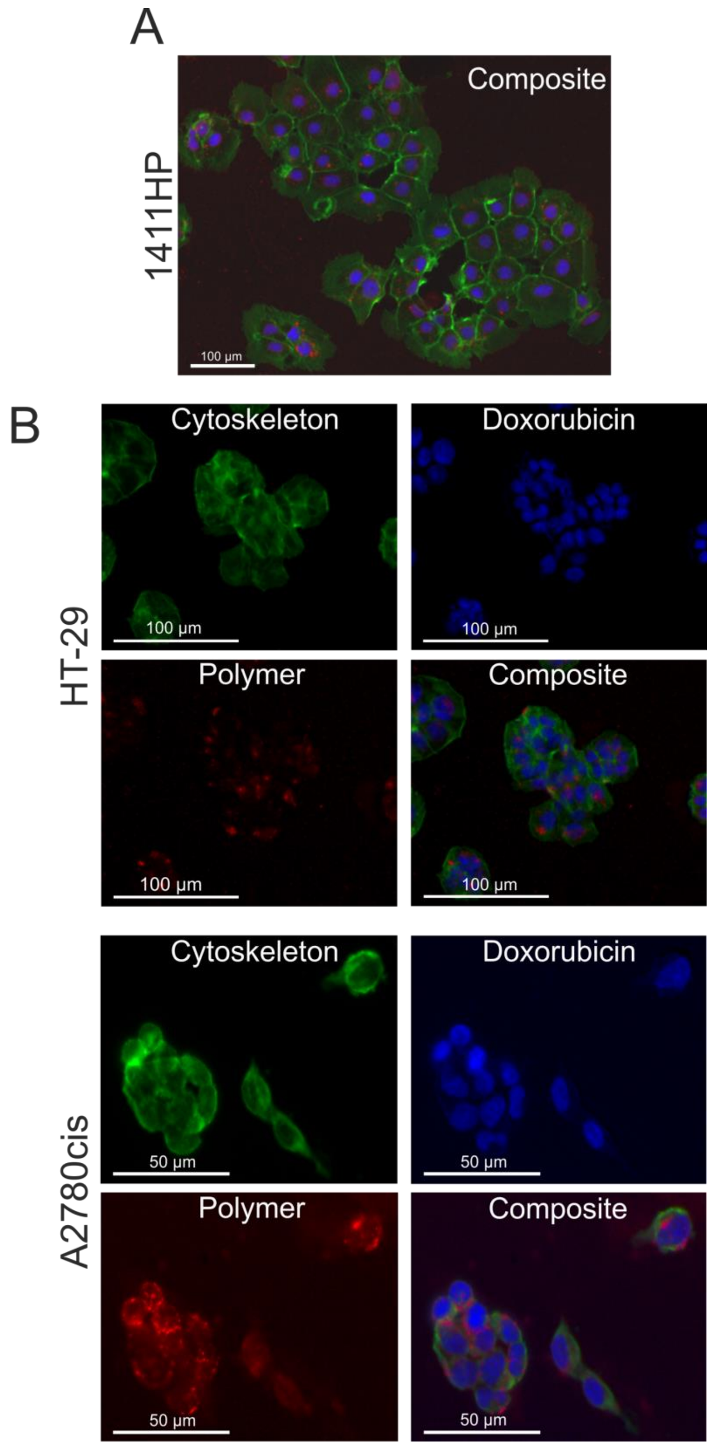
A
1411HP
Composite
100 µm
B
HT-29
Cytoskeleton
100 µm
Doxorubicin
100 µm
Polymer
100 µm
Composite
100 µm
A2780cis
Cytoskeleton
50 µm
Doxorubicin
50 µm
Polymer
50 µm
Composite
50 µm

Fig. 50. Single spectral images (B) and composite images (A and B) of cell monolayers (1411HP (A), HT-29 (B, middle) and A2780cis (B, bottom)) obtained by msFM. Blue color was assigned to doxorubicin, red to the polymer (dye CY-7) and green was assigned to the cytoskeleton (Alexa Fluor® 488 Phalloidin). Doxorubicin signal was always detectable in the cell nuclei whereas the polymer signal was mainly locatable in cytoplasm especially near the nuclear membrane. This pattern was comparable in all three cell lines and confirmed a similar mechanism of cellular uptake and intracellular cleavage of the pH-sensitive bond between doxorubicin and the polymer carrier. Purple regions visualized the polymer with doxorubicin.

On the other hand, the polydispersity of the pHPMA-doxorubicin conjugate obviously leads to the existence of fractions with higher and also much lower M_w than 200 kDa. The polymer fraction with lower M_w might be able to enter the nuclei already before the doxorubicin was released.

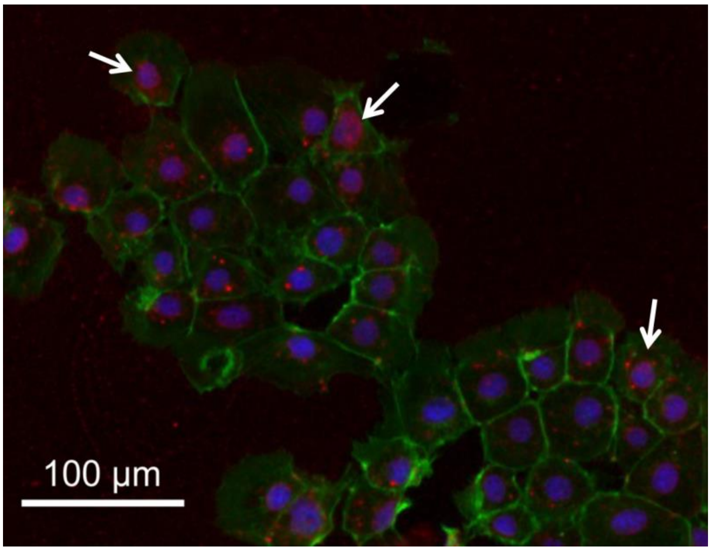

Fig. 51. Composite image of fixed 1411HP cells obtained by msFM. Blue color was assigned to doxorubicin, red to the polymer (dye CY-7) and green was assigned to the cytoskeleton (Alexa Fluor® 488 Phalloidin). Doxorubicin signal was always detectable in the cell nuclei whereas the polymer signal was mainly locatable in cytoplasm especially near the nuclear membrane. Purple regions (white arrows) visualized the polymer with still non-released doxorubicin or at least the co-localization of both within the same cellular compartment e.g. cytoplasm or cell nuclei.

However, the main distribution area of the polymer is the cytosol. Moreover, the punctate pattern of the polymer signal suggests the assumption of endosomal or lysosomal localization. These findings confirmed the assumed mechanism of the drug release from the polymeric carrier at least *in vitro* and indicated that the mechanism of cellular uptake is similar for the three different cell lines. Therefore, the assumption that xenograft specific characteristics are responsible for the different tumor response *in vivo* was strongly corroborated.

3.3.7 Multispectral fluorescence microscopy of fixed tumor xenograft sections

As the cell monolayer is an artificial model which did not nearly represent the *in vivo* situation within a solid tumor, further microscopic examinations were performed, to determine the mechanism of doxorubicin release specifically in these three tumor xenografts. The msFM also allowed the detection of doxorubicin and the polymer simultaneously within tumor sections of necropsied tumor xenografts, after the i.v. application of the **A***S*180DoxF conjugate. To ensure the fluorescence microscopic detection of the polymer label, the highest tolerable dose (30 mg/kg BW doxorubicin equivalent) was administered to A2780cis, 1411HP and HT-29 tumor xenograft bearing athymic nude mice. 48 h (in case of A2780cis and HT-29 24 h due to increased toxic side effects) after injection the mice were sacrificed, tumors were necropsied and sections were prepared. The tumor sections for the msFM examination were left unstained. The results of msFM (Fig. 52) revealed a quite different distribution pattern of doxorubicin and polymer in the 1411HP tumor xenograft compared to A2780cis and HT-29. In 1411HP tumors the polymer was mainly locatable within the cytoplasm and to a lower extend also in the interstitial compartment. Purple regions were also visible, indicating the intact **A***S*180DoxF conjugate. Doxorubicin was predominantly detectable within the cell nuclei (Fig. 52, top). This confirmed the mechanism of action, which comprises the endocytic uptake of the whole conjugate, the intracellular drug release and its DNA intercalation, as it was already observed *in vitro* at the cell monolayer. Unfortunately, no reliable quantification is possible with the applied method but it is assumable that the cellular uptake of the whole conjugate does not happen to the same extend and with the same speed like in the cell monolayer due to natural barriers like tumor ECM or necrotic areas, especially within bigger tumor xenografts. If this would not be the case, the *in vivo* response in 1411HP tumors would have been expected earlier instead of the delayed tumor regression. The high amount of accumulated doxorubicin within the cells and interstitial compartments, combined with the above discussed change of the microenvironment during the treatment, is supposed to be responsible for the remarkable therapeutic success.

In the A2780cis tumor xenograft another pattern became apparent (Fig. 52, middle). The polymer was predominantly distributed in the interstitial compartment. Doxorubicin was detectable in the cell nuclei, but also in cell nuclei which were remote from regions were the polymer was detectable. However, there were also regions were the polymer signal was also detectable in the cytoplasm comparable to 1411HP, but the displayed distribution pattern was much more pronounced. It can be assumed, that the pH-dependent cleavage of doxorubicin already happened in the interstitial compartment. This led to the distribution of the free drug through the tumor tissue into the cells. Overall, the distribution of doxorubicin was more inhomogeneous compared to the 1411HP tumor, probably due to its early cleavage.

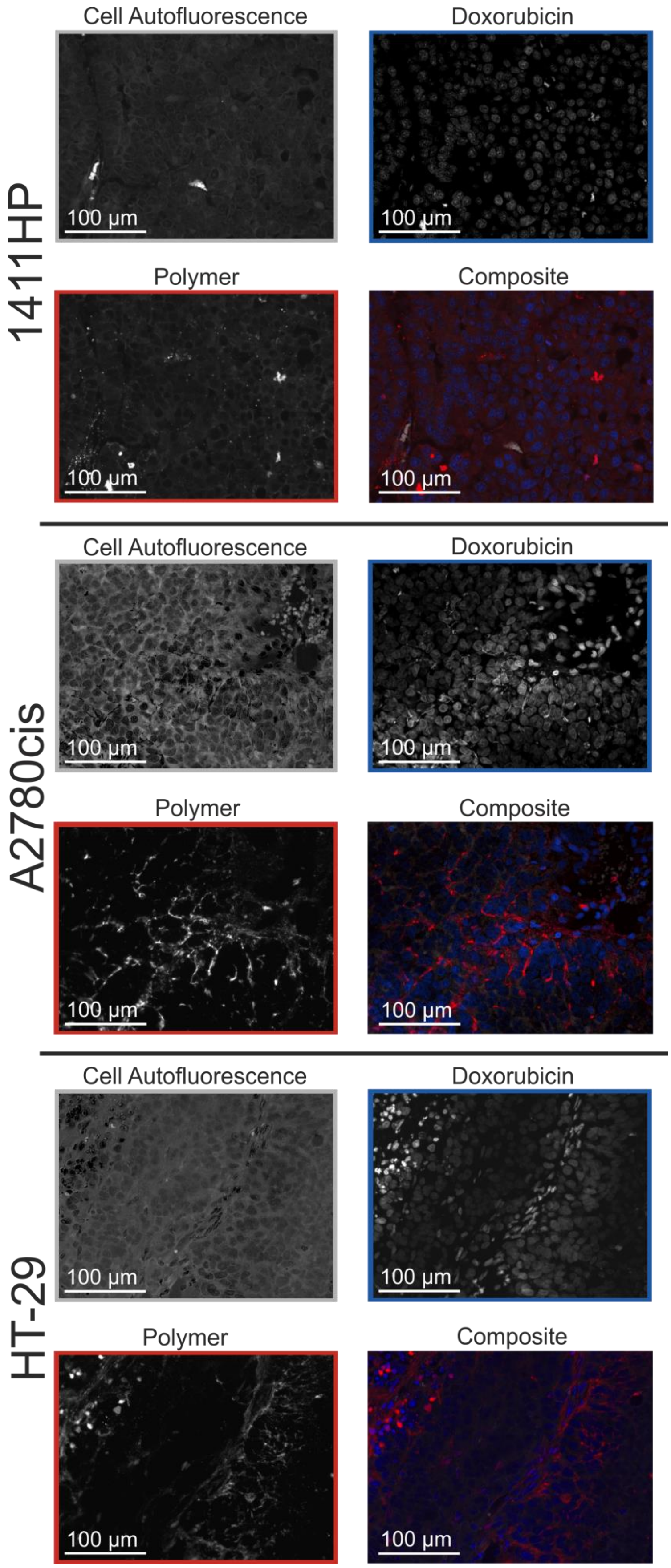
1411HP
Cell Autofluorescence
Doxorubicin
Polymer
Composite
A2780cis
Cell Autofluorescence
Doxorubicin
Polymer
Composite
HT-29
Cell Autofluorescence
Doxorubicin
Polymer
Composite
100 µm

Fig. 52. Single spectral images and composite images of necropsied and sliced 1411HP (top), A2780cis (middle) and HT-29 (bottom) tumor xenografts 48 h (A2780cis & HT-29 24 h) after i.v. administration of conjugate **A*S*180DoxF** (30 mg/ kg BW doxorubicin equivalent) obtained by msFM. Cell autofluorescence was colored grey, doxorubicin blue and the polymer (CY-7) red. Doxorubicin was detectable predominantly in the cell nuclei of all three tumor types. The polymer distribution differed. In the 1411HP tumor the polymer was mainly located in the cytoplasm whereas in A2780cis and HT-29 it was mainly detectable in the interstitial compartment indicating a quick doxorubicin release before cell internalization of the whole conjugate.

Furthermore, the efflux pumps, one of the A2780cis resistance mechanisms, could work much more effective if the free drug is internalized, compared to the whole pHPMA-doxorubicin conjugate. This would be disadvantageous for a successful anti-tumor treatment. These findings were in accordance with the results of the tumor microenvironment studies. The appropriate micromilieu in this tumor type for the pH-dependent drug release might have led to the early and interstitial cleavage of doxorubicin, already before the conjugate was internalized into the cells. This early cleavage might have led to the inhomogeneous tumor distribution and probably hampered the evasion of the efflux pumps. Furthermore, it can be assumed that at least a part from the interstitially released doxorubicin is responsible for the increased toxic side effects in A2780cis tumor bearing mice, due to a partial recirculation of the drug. The higher tolerability against the pHPMA-doxorubicin treatment of 1411HP tumor bearing mice leads to the assumption, that it is advantageous if the whole conjugate is internalized into the cells, avoiding interstitial drug release.

In the HT-29 tumor sections the distribution pattern was partly comparable to A2780cis tumor sections (Fig. 52, bottom). The polymer was detectable in the interstitial compartment and also within the septa, which are present in this tumor xenograft. Purple regions, indicating the intact conjugate, were rare. Doxorubicin was traced in the cell nuclei, also in regions were the polymer was lacking. Tumor sections of the HT-29 xenograft showed, that the distribution of the conjugate was quite inhomogeneous. In the displayed tumor slice three different regions were observable. At the upper left side an apoptotic region is visible. The cells are small and spherical and appear purple and very bright because of the overlapping fluorescence intensities within the shrinking cells. At the lower right side an area of vital tumor cells is visible with the typical pattern of interstitial located polymer, while doxorubicin was already released and detectable in the cell nuclei. In the middle a region of very low **A***S*180DoxF conjugate accumulation is visible. Although nearly no polymer signal could be detected, the cell nuclei appeared already blue, indicating the presence of doxorubicin. It can be assumed that due to the comparatively extreme hypoxic and acidic microenvironment in this tumor type, doxorubicin was already released before cell internalization of the conjugate, comparable to the A2780cis tumor xenograft. As a consequence, the free drug diffused through the tissue into the cells. The existence of efflux pumps and natural barriers like ECM resulted in an inhomogeneous distribution and a lacking tumor regression. This was already observed in the *in vivo* experiment.

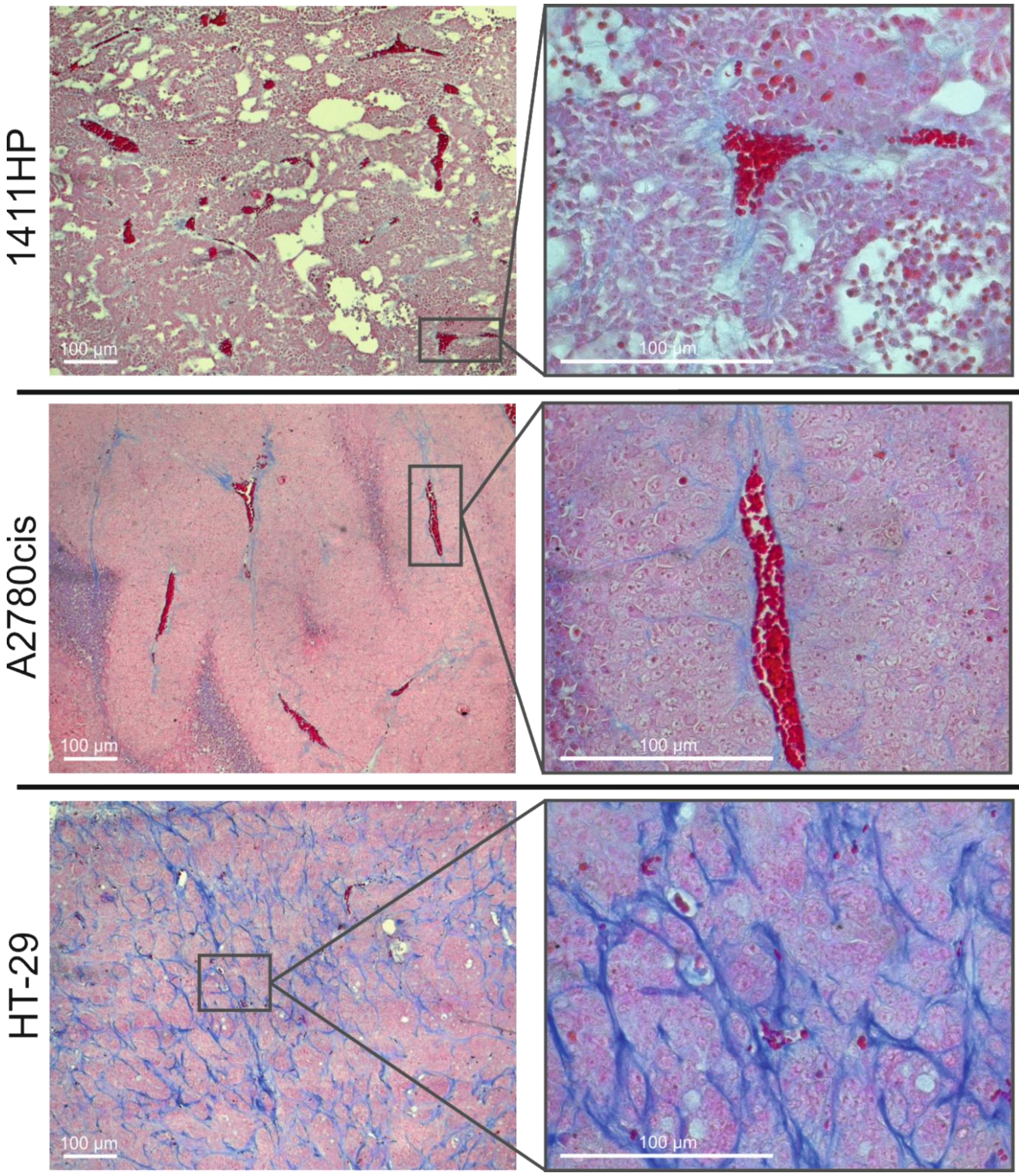

Fig. 53. Azan stained tumor tissue sections of 1411HP (top), A2780cis (middle) and HT-29 (bottom) xenografts. On the left side a histological overview image is displayed (100 x magnification), on the right side a zoom is displayed (400 x magnification). White bars display 100 µm. Cell nuclei appear red, cytoplasm pink and collagen is stained blue. 1411HP and A2780cis exhibit only low amounts of collagen, mainly as a part of the blood vessel walls. In the HT-29 xenograft the collagen amount is much higher indicating a high amount of ECM.

Beyond that, the tumor substructure seems to play an important role for the diffusion of the conjugate, which might be crucial for the therapeutic success. The interdependency between tumor microenvironment and the behavior of cancer nanomedicines was also recently discussed by Hare *et al.* (9) and is of great importance for the design of upcoming drug delivery systems. As it was already described in the previous section, the tumor substructure of HT-29 xenografts is characterized by large necrotic and fibrotic areas and sparse vascularization. Although these properties facilitate the pH-dependent drug release due to the hypoxic/acidic micro milieu, they obviously also inhibit a homogeneous distribution through the whole tumor and the beneficial intracellular drug release. Furthermore, the conjugate and the released drug might be trapped in the necrotic regions comparable to DLD-1 tumors, as it was already described in subsection 3.1.3.1. The ECM within a tumor xenograft can represent a barrier for the diffusion of the pHPMA-doxorubicin conjugates. Besides the tumor micromilieu, the amount of ECM can thereby affect the therapeutic success. Histological examinations of H & E stained tumor xenograft sections indicated that 1411HP and A2780cis tumors exhibit only a low amount of ECM whereas the amount in the colon-carcinoma cell line HT-29 is higher. For improved statements about the ECM in the respective tumor xenografts, a comparative histological evaluation of azan-stained tumor xenograft sections was performed.

This staining method is used to stain collagen, a main component of tumor ECM. After the staining, collagen appears blue while the cell nuclei appear red. The results of the microscopic evaluation of the stained tumor sections of 1411HP, A2780cis and HT-29 xenografts revealed obvious differences between the three tumor types regarding the amount of collagen as a part of ECM (Fig. 53). An overview (Fig. 53, left side) and a more detailed microscopic image (Fig. 53, right side) of each tumor type are displayed. In case of the 1411HP xenograft a high number of large blood vessels was visible. Only a few blue stained areas were observable. They were mainly localized around the blood vessels, which became much more obvious in the detailed microscopic image. This was not surprising, as collagen is a component of blood vessel walls. Apart from the blood vessels, only a very few blue areas were visible, indicating a low amount of ECM within this tumor xenograft. In the A2780cis tumor xenograft also a lot of large blood vessels were visible. They exhibited blue stained walls as well, indicating the presence of collagen. Besides, collagen was also partly detectable apart from blood vessels across the whole tumor section. These collagen fibers could be a part of the tumor ECM which is more pronounced in A2780cis compared to 1411HP. Nevertheless, this tumor type overall exhibits also a low amount of ECM. This became much more obvious when evaluating the histological sections of the HT-29 xenograft. In this tumor type the distinct presence of collagen can be observed across the whole tumor section, as a lot of blue stained areas were visible. This indicated the presence of a high amount of tumor ECM which might represent a natural barrier for the diffusion of the applied pHPMA-doxorubicin conjugate (81). This contributed to the lacking tumor regression within this tumor type, which was observed in the *in vivo* experiment.

Taking everything into account, it can be concluded that the coincident presence of a highly hypoxic and acidic micromilieu, which leads to an early, interstitial doxorubicin release, and the presumably hampered conjugate and drug distribution through the tumor tissue due to a high amount of ECM, is disadvantageous for the treatment with the applied pHPMA-doxorubicin conjugates. The results of this experiment revealed that a differing tumor microenvironment, especially regarding hypoxia, pH and ECM amount, led to a doxorubicin release at different rates, in different cell compartments and to a different extend. This has a notable influence on the therapeutic success and must be considered for the development of a suitable conjugate and dosage schedule for the respective tumor type.

3.3.8 **Summary**

Various investigations were made to figure out what happened inside of different solid tumors under the treatment with the pH-sensitive pHPMA-doxorubicin conjugate. *In vitro*, *in vivo* and *ex vivo* experiments were conducted to determine the underlying mechanisms of action, to allow predictions of the therapeutic success in several types of cancer. Based on the results of the therapy study described in section 3.2.3 it was determined, how the applied dosage schedule influences the therapeutic success in 1411HP and A2780cis tumor bearing mice. It became obvious, that a 5-fold total dose must be administered within 10 days independent of the number of injections. The necessary total dose and also the tolerability against the pHPMA-doxorubicin conjugate were lower in A2780cis tumor bearing mice. This confirmed the previously supposed tumor-type-dependent tumor response and toxicity profile. It is noteworthy, that by the use of the free drug it is not possible to administer these high doses of doxorubicin, like they were achieved with the pHPMA-doxorubicin conjugate, due to fatal toxic side effects. The enhanced tumor delivery of doxorubicin due to the administered high doses was clearly demonstrated by msFI. Additionally, *in vitro* cytotoxicity tests were performed and revealed a comparable pH-dependent sensitivity to the pHPMA-doxorubicin treatment of the three cell lines, indicating that xenograft characteristics must be responsible for the different *in vivo* behavior. Tumor microenvironment studies confirmed this assumption, as they revealed a much more advantageous micromilieu for the pH-dependent drug release in A2780cis than in 1411HP tumors. Further investigations regarding a tumor-type-dependency included also the human colon carcinoma cell line HT-29, which has a quite different tumor substructure. The HT-29 tumor xenografts were characterized by an extreme hypoxic/acidic microenvironment, which was observed in another tumor microenvironment study. Although this cell line showed an immediate tumor response already after the first injection, no tumor regression was achieved. Furthermore, a much lower tolerability against the treatment was noticed, which allowed only lower total doses compared to 1411HP and A2780cis.

By msFM a possible underlying mechanism for the tumor-type-dependent response to the **A***S*200Dox conjugate was determined. First, it was checked by *in vitro* examinations of cell monolayers, whether the cell uptake and drug release was comparable on cellular level. It was observable that the whole conjugate was internalized, assumably followed by the lysosomal cleavage of the pH-sensitive linker between drug and polymer backbone, which led to the doxorubicin release. Doxorubicin was then found in the cell nuclei, whereas the fluorescently labeled polymer was located in the cytoplasm, mainly near the nuclear membrane. This pattern was similar for all three cell lines. The cell monolayer did not represent the *in vivo* situation of a real solid tumor due to the lacking microenvironment and ECM. Therefore, similar examinations were performed with sections of necropsied tumor xenografts after previous injection of the **A***S*180DoxF conjugate. Interestingly, obvious differences became apparent here. While the intracellular drug release, which was assumed based on the *in vitro* results, could be observed in the 1411HP tumor model, a rather interstitial drug release was visible in the A2780cis and HT-29 tumor models. These observations were ascribed to the different tumor microenvironment which only develops within the xenografts and not on cell monolayers. As it is known from the experiments, A2780cis and also HT-29 revealed a much more advantageous micromilieu for the pH-dependent drug release. Thereby, the release happened very early and effective but obviously mainly before cell internalization of the conjugate. This was disadvantageous for the mechanism of action and hampered a homogenous drug distribution within the tumor. Consequently, the resistance mechanisms of the multi-resistant cells could not be negotiated sufficiently. Furthermore, the early and interstitial drug release induced increased and dose-limiting toxic side effects, which were observable in the therapy studies. The adjustment of the applied dosage schedule or the switch to another linker between drug and polymer backbone must be taken into consideration for the tumor types that exhibited a hypoxic/acidic microenvironment such as A2780cis and HT-29. These interesting findings are very important as they confirmed the existence of a tumor-type-dependency regarding the therapeutic success and toxicity profile of the applied system, which should be considered for upcoming studies with these conjugates.

4. Summary and Perspectives

Polymeric drug delivery systems represent excellent tools for cancer treatment as they are able to improve the tumor accumulation of the chemotherapeutic drug and decrease the toxic side effects. Furthermore, the development of stimulus-sensitive drug delivery systems can prevent the peripheral drug release which is also beneficial for the therapy outcome. Three different pHPMA-based stimulus-sensitive drug delivery systems, differing in M_w, architecture and linker between drug model and polymer backbone, were comparatively examined regarding their biodistribution and tumor-site specific drug release. For this purpose, the non-invasive method of *in vivo* msFI was applied. Thereby, it was shown that the reduction-sensitive as well as the enzymatically cleavable and pH-sensitive conjugates showed excellent tumor accumulation and achieved a drug release exclusively at the tumor site. With the exception of the pH-sensitive conjugate, it became obvious that the lower M_w conjugates were advantageous compared to the higher M_w conjugates. This effect was ascribed to the existence of steric hindrance, which hampered the accessibility for the enzymes that are partly necessary for the cleavage of the linker between drug and polymer backbone. In contrast, the star-like high M_w conjugate was preferential in case of the enzyme-independent pH-sensitive conjugate. As this conjugate showed an excellent tumor accumulation and a tumor-site specific drug model release, it was used for the performance of a therapy study after the replacement of the drug model by the chemotherapeutic agent doxorubicin. After the determination of a suitable multi-drug resistant tumor model, the conjugate was investigated regarding its therapeutic efficacy in tumor bearing mice. The results were very promising, as an overcoming of drug resistance in the chosen human germ cell carcinoma model was achieved.

The influence of the applied treatment schedule on the therapy outcome was determined. The administration of a total dose of 25 mg/kg BW of polymer-bound doxorubicin within a time period of maximal 10 days led to the reproducible onset of the tumor regression independent of the number of injections or the time interval. However, the dose schedule with applications once a week was preferably tolerated, as there was an optimal balance between toxic side effects and therapy outcome.

When the same treatment schedule was applied in a multi-drug resistant human ovarian carcinoma model, differences regarding tolerability and therapeutic efficacy appeared. These findings were attributed to a different tumor microenvironment in this tumor type. This was confirmed by comparative investigations of the tumor microenvironment especially regarding the presence of hypoxia. As hypoxia was found to be a supportive condition for the pH-sensitive drug release, it was assumed that tumors with a more hypoxic microenvironment show a quicker tumor response but also induce increased side effects. The performed studies confirmed these assumptions and indicated a tumor-type dependent therapeutic efficacy and tolerability.

In addition, two human colon-carcinoma cell lines with a different morphology were examined regarding their microenvironment and one of them was chosen for further investigations regarding the underlying mechanisms of intratumoral drug release. MsFM examinations were performed, to visualize the applied polymeric carrier and the pH-dependent cleavable drug simultaneously on cellular level. Initially, cell monolayers of the three different cancer cell lines were investigated after cultivation and incubation with the fluorescently labeled pHPMA-doxorubicin conjugate. The supposed mechanism of cellular internalization of the whole conjugate and lysosomal release of the pH-dependent cleavable drug was confirmed for all three cell lines. However, an unimpeded endocytosis of the 200 kDa pHPMA-doxorubicin conjugate was not expected for a real solid tumor. In contrast to the artificial model of a cell monolayer, a solid tumor comprises a very complex microenvironment which was already shown to have great influence on therapeutic response.

Further msFM examinations were performed, to clarify the influence of tumor substructure and microenvironment on the mechanism of intratumoral drug release. Tumor bearing mice were treated with the fluorescently labeled pHPMA-doxorubicin conjugate. Sections of the necropsied tumors were evaluated by msFM. Interestingly, the hypothesis of an interdependency of tumor microenvironment and drug release was confirmed. It was shown, that the presence of hypoxia, which supports the acidification of the tumor milieu, led to a very early doxorubicin release which inhibited the internalization of the whole conjugate. As a consequence the drug distribution within the tumor tissue was inhomogeneous. It was assumed, that the inhomogeneous drug distribution would affect the therapeutic success. Nevertheless, it was shown in the previous *in vivo* studies that a tumor regression was achievable in this tumor type but the early doxorubicin cleavage in interstitial compartments of the tumor induced increased toxic side effects. Moreover, it was shown that the coexistence of hypoxia and a high amount of ECM strongly affected the therapeutic success, probably due to hindered diffusion processes of the conjugate within the tumor. In this case, no tumor regression was achieved with the applied pHPMA-doxorubicin conjugate.

These important results indicate the necessity of an improved understanding on cancer heterogeneity and the influence of tumor microenvironment and substructure on the therapeutic success of the respective stimulus-sensitive drug delivery systems *in vivo*. Further studies need to be performed to explicitly determine the influence of tumor type dependent characteristics on the *in vivo* behavior of the pH-dependent polymeric drug delivery system. An improved knowledge about the relation between tumor microenvironment and response to the treatment would allow predictions about the therapeutic success in the respective cancer type, which is important to prevent therapy failure.

Despite the promising results for the star-like structured pHPMA-doxorubicin conjugate in two multi-drug resistant cancer cell lines, an optimization of the applied conjugate is recommended for future studies. Although previous studies have shown that even the high M_w, star-like conjugate was eliminated from the body within three months, the non-biodegradability of the pHPMA backbone and its restricted renal elimination, due to the increased M_w and $R_{H,}$ can lead to undesired long-term accumulation within the body. As already shown by Etrych *et al.*, the integration of e.g. enzymatically cleavable linkers like GFLG between the dendrimer core and the side-chains of the star-like conjugate, would allow a disassembly into lower M_w units which underlie renal elimination. Thereby, the beneficial tumor accumulation of a high M_w conjugate is ensured but an uncontrolled long-term accumulation could be prevented. Comparative studies regarding biodistribution and therapeutic efficacy of the non-degradable and a degradable conjugate should be performed to confirm this assumption.

Unfortunately, s.c. tumor xenografts do not exactly represent the *in vivo* situation. The development of orthotopic and metastasizing models and the performance of therapy studies with these models are crucial to allow reliable statements about therapeutic success *in vivo*, especially when considering future clinical studies.

5. Appendix

References

1. Karpozilos A, Pavlidis N. The treatment of cancer in Greek antiquity. European journal of cancer 2004; 40(14):2033–40.
2. Hajdu SI. Greco-Roman thought about cancer. Cancer 2004; 100(10):2048–51.
3. Stewart BW, Wild CP. World Cancer Report 2014. Lyon: International Agency for Research on Cancer/World Health Organization; 2014.
4. Gottesman MM. Mechanisms of cancer drug resistance. Annual review of medicine 2002; 53:615–27.
5. Carelle N, Piotto E, Bellanger A, Germanaud J, Thuillier A, Khayat D. Changing patient perceptions of the side effects of cancer chemotherapy. Cancer 2002; 95(1):155–63.
6. Danhier F, Feron O, Preat V. To exploit the tumor microenvironment: Passive and active tumor targeting of nanocarriers for anti-cancer drug delivery. Journal of controlled release 2010; 148(2):135–46.
7. Matsumura Y, Maeda H. A new concept for macromolecular therapeutics in cancer chemotherapy: mechanism of tumoritropic accumulation of proteins and the antitumor agent smancs. Cancer research 1986; 46(12 Pt 1):6387–92.
8. Maeda H. The enhanced permeability and retention (EPR) effect in tumor vasculature: the key role of tumor-selective macromolecular drug targeting. Advances in enzyme regulation 2001; 41:189–207.
9. Hare JI, Lammers T, Ashford MB, Puri S, Storm G, Barry ST. Challenges and strategies in anti-cancer nanomedicine development: An industry perspective. Advanced drug delivery reviews 2017; 108:25-38.
10. Steichen SD, Caldorera-Moore M, Peppas NA. A review of current nanoparticle and targeting moieties for the delivery of cancer therapeutics. European journal of pharmaceutical sciences 2013; 48(3):416–27.

11. Etrych T, Šubr V, Strohalm J, Sirová M, Rihová B, Ulbrich K. HPMA copolymer-doxorubicin conjugates: The effects of molecular weight and architecture on biodistribution and *in vivo* activity. Journal of controlled release 2012; 164(3):346–54.

12. Immordino ML, Dosio F, Cattel L. Stealth liposomes: review of the basic science, rationale, and clinical applications, existing and potential. International journal of nanomedicine 2006; 1(3):297–315.

13. Sudimack J, Lee RJ. Targeted drug delivery via the folate receptor. Advanced drug delivery reviews 2000; 41(2):147–62.

14. Sahoo SK, Ma W, Labhasetwar V. Efficacy of transferrin-conjugated paclitaxel-loaded nanoparticles in a murine model of prostate cancer. International journal of cancer 2004; 112(2):335–40.

15. Ryschich E, Huszty G, Knaebel HP, Hartel M, Büchler MW, Schmidt J. Transferrin receptor is a marker of malignant phenotype in human pancreatic cancer and in neuroendocrine carcinoma of the pancreas. European journal of cancer 2004; 40(9):1418–22.

16. Dotan E, Aggarwal C, Smith MR. Impact of Rituximab (Rituxan) on the Treatment of B-Cell Non-Hodgkin's Lymphoma. P & T a peer-reviewed journal for formulary management 2010; 35(3):148–57.

17. Lemery SJ, Zhang J, Rothmann MD, Yang J, Earp J, Zhao H *et al.* U.S. Food and Drug Administration approval: ofatumumab for the treatment of patients with chronic lymphocytic leukemia refractory to fludarabine and alemtuzumab. Clinical cancer research 2010; 16(17):4331–8.

18. Zhong Y, Meng F, Deng C, Zhong Z. Ligand-directed active tumor-targeting polymeric nanoparticles for cancer chemotherapy. Biomacromolecules 2014; 15(6):1955–69.

19. Liu Z, Wang F, Chen X. Integrin alpha(v)beta(3)-Targeted Cancer Therapy. Drug development research 2008; 69(6):329–39.

20. Ganta S, Devalapally H, Shahiwala A, Amiji M. A review of stimuli-responsive nanocarriers for drug and gene delivery. Journal of controlled release 2008; 126(3):187–204.

21. Studenovsky M, Heinrich A-K, Lucas H, Mueller T, Mäder K, Etrych T. Dual fluorescent N-(2-hydroxypropyl) methacrylamide-based conjugates for passive tumor targeting with

reduction-sensitive drug release: Proof of the concept, tumor accumulation, and biodistribution. Journal of Bioactive and Compatible Polymers 2016; 31(4):348–60.

22. Pola R, Heinrich A-K, Mueller T, Kostka L, Mäder K, Pechar M *et al.* Passive Tumor Targeting of Polymer Therapeutics: *In Vivo* Imaging of Both the Polymer Carrier and the Enzymatically Cleavable Drug Model. Macromolecular bioscience 2016; 16(11):1577–82.
23. Heinrich A-K, Lucas H, Schindler L, Chytil P, Etrych T, Mäder K *et al.* Improved Tumor-Specific Drug Accumulation by Polymer Therapeutics with pH-Sensitive Drug Release Overcomes Chemotherapy Resistance. Molecular cancer therapeutics 2016; 15(5):998–1007.
24. Gabizon A, Shmeeda H, Barenholz Y. Pharmacokinetics of pegylated liposomal Doxorubicin: review of animal and human studies. Clinical pharmacokinetics 2003; 42(5):419–36.
25. Barenholz Y. Doxil®-the first FDA-approved nano-drug: lessons learned. Journal of controlled release 2012; 160(2):117–34.
26. Dinndorf PA, Gootenberg J, Cohen MH, Keegan P, Pazdur R. FDA drug approval summary: pegaspargase (oncaspar) for the first-line treatment of children with acute lymphoblastic leukemia (ALL). The oncologist 2007; 12(8):991–8.
27. Veronese FM, Mero A. The Impact of PEGylation on Biological Therapies. BioDrugs 2008; 22(5):315–29.
28. Thomas A, Teicher BA, Hassan R. Antibody–drug conjugates for cancer therapy. The Lancet Oncology 2016; 17(6):e254-e262.
29. Zhang H. Onivyde for the therapy of multiple solid tumors. OncoTargets and therapy 2016; 9:3001–7.
30. Venditto VJ, Szoka FC JR. Cancer nanomedicines: so many papers and so few drugs! Advanced drug delivery reviews 2013; 65(1):80–8.
31. Tomalova B, Sirova M, Rossmann P, Pola R, Strohalm J, Chytil P *et al.* The structure-dependent toxicity, pharmacokinetics and anti-tumour activity of HPMA copolymer conjugates in the treatment of solid tumours and leukaemia. Journal of controlled release 2016; 223:1–10.
32. Sirova M, Mrkvan T, Etrych T, Chytil P, Rossmann P, Ibrahimova M *et al.* Preclinical evaluation of linear HPMA-doxorubicin conjugates with pH-sensitive drug release: efficacy,

safety, and immunomodulating activity in murine model. Pharmaceutical research 2010; 27(1):200–8.

33. Minko T, Kopečková P, Kopeček J. Efficacy of the chemotherapeutic action of HPMA copolymer-bound doxorubicin in a solid tumor model of ovarian carcinoma. International Journal of Cancer 2000; 86(1):108–17.
34. Dozono H, Yanazume S, Nakamura H, Etrych T, Chytil P, Ulbrich K *et al.* HPMA Copolymer-Conjugated Pirarubicin in Multimodal Treatment of a Patient with Stage IV Prostate Cancer and Extensive Lung and Bone Metastases. Targeted oncology 2016; 11(1):101–6.
35. Kopeček J., Bažilová H. Poly[N-(2-hydroxypropyl)methacrylamide]—I. Radical polymerization and copolymerization. European polymer journal 1973; 9(1):7–14.
36. Duncan R. Development of HPMA copolymer-anticancer conjugates: clinical experience and lessons learnt. Advanced drug delivery reviews 2009; 61(13):1131–48.
37. Kopeček J, Kopečková P. HPMA copolymers: origins, early developments, present, and future. Advanced drug delivery reviews 2010; 62(2):122–49.
38. Larson N, Ghandehari H. Polymeric conjugates for drug delivery. Chemistry of materials a publication of the American Chemical Society 2012; 24(5):840–53.
39. Nowotnik DP, Cvitkovic E. ProLindac (AP5346): a review of the development of an HPMA DACH platinum Polymer Therapeutic. Advanced drug delivery reviews 2009; 61(13):1214–9.
40. Goel S, England CG, Chen F, Cai W. Positron emission tomography and nanotechnology: A dynamic duo for cancer theranostics. Advanced drug delivery reviews 2016 [Epub ahead of print].
41. Allmeroth M, Moderegger D, Gündel D, Koynov K, Buchholz H-G, Mohr K *et al.* HPMA-LMA copolymer drug carriers in oncology: an *in vivo* PET study to assess the tumor line-specific polymer uptake and body distribution. Biomacromolecules 2013; 14(9):3091–101.
42. Herth MM, Barz M, Moderegger D, Allmeroth M, Jahn M, Thews O *et al.* Radioactive labeling of defined HPMA-based polymeric structures using [^{18}F]FETos for *in vivo* imaging by positron emission tomography. Biomacromolecules 2009; 10(7):1697–703.
43. Griffeth LK. Use of PET/CT scanning in cancer patients: technical and practical considerations. Proceedings (Baylor University. Medical Center) 2005; 18(4):321–30.

44. Levenson RM, Lynch DT, Kobayashi H, Backer JM, Backer MV. Multiplexing with multispectral imaging: from mice to microscopy. ILAR journal 2008; 49(1):78–88.

45. Hoffmann S, Vystrcilova L, Ulbrich K, Etrych T, Caysa H, Mueller T *et al*. Dual fluorescent HPMA copolymers for passive tumor targeting with pH-sensitive drug release: synthesis and characterization of distribution and tumor accumulation in mice by noninvasive multispectral optical imaging. Biomacromolecules 2012; 13(3):652–63.

46. Leblond F, Davis SC, Valdes PA, Pogue BW. Pre-clinical whole-body fluorescence imaging: Review of instruments, methods and applications. Journal of photochemistry and photobiology. B, Biology 2010; 98(1):77–94.

47. Schädlich A, Caysa H, Mueller T, Tenambergen F, Rose C, Göpferich A *et al*. Tumor accumulation of NIR fluorescent PEG-PLA nanoparticles: impact of particle size and human xenograft tumor model. ACS nano 2011; 5(11):8710–20.

48. Hoffmann S, Caysa H, Kuntsche J, Kreideweiss P, Leimert A, Mueller T *et al*. Carbohydrate plasma expanders for passive tumor targeting: *in vitro* and *in vivo* studies. Carbohydrate polymers 2013; 95(1):404–13.

49. Mondal SB, Gao S, Zhu N, Liang R, Gruev V, Achilefu S. Real-time fluorescence image-guided oncologic surgery. Advances in cancer research 2014; 124:171–211.

50. Nguyen QT, Tsien RY. Fluorescence-guided surgery with live molecular navigation-a new cutting edge. Nature reviews. Cancer 2013; 13(9):653–62.

51. Kraft JC, Ho RJY. Interactions of indocyanine green and lipid in enhancing near-infrared fluorescence properties: the basis for near-infrared imaging *in vivo*. Biochemistry 2014; 53(8):1275–83.

52. Chytil P, Hoffmann S, Schindler L, Kostka L, Ulbrich K, Caysa H *et al*. Dual fluorescent HPMA copolymers for passive tumor targeting with pH-sensitive drug release II: impact of release rate on biodistribution. Journal of controlled release 2013; 172(2):504–12.

53. Skehan P, Storeng R, Scudiero D, Monks A, McMahon J, Vistica D *et al*. New colorimetric cytotoxicity assay for anticancer-drug screening. Journal of the National Cancer Institute 1990; 82(13):1107–12.

54. Tomayko MM, Reynolds CP. Determination of subcutaneous tumor size in athymic (nude) mice. Cancer Chemotherapy and Pharmacology 1989; 24(3):148–54.

55. Yang J, Kopeček J. Macromolecular therapeutics. Journal of controlled release 2014; 190:288–303.

56. Lammers T. Improving the efficacy of combined modality anticancer therapy using HPMA copolymer-based nanomedicine formulations. Advanced drug delivery reviews 2010; 62(2):203–30.

57. Saito G, Swanson JA, Lee K-D. Drug delivery strategy utilizing conjugation via reversible disulfide linkages: role and site of cellular reducing activities. Advanced drug delivery reviews 2003; 55(2):199–215.

58. Liu L, Liu P. Synthesis strategies for disulfide bond-containing polymer-based drug delivery system for reduction-responsive controlled release. Frontiers of Materials Science 2015; 9(3):211–26.

59. Kovář M, Strohalm J, Etrych T, Ulbrich K, Říhová B. Star Structure of Antibody-Targeted HPMA Copolymer-Bound Doxorubicin: A Novel Type of Polymeric Conjugate for Targeted Drug Delivery with Potent Antitumor Effect. Bioconjugate Chemistry 2002; 13(2):206–15.

60. Lammers T, Kühnlein R, Kissel M, Šubr V, Etrych T, Pola R *et al*. Effect of physicochemical modification on the biodistribution and tumor accumulation of HPMA copolymers. Journal of controlled release 2005; 110(1):103–18.

61. Berquin IM, Sloane BF. Cathepsin B expression in human tumors. Advances in experimental medicine and biology 1996; 389:281–94.

62. Etrych T, Jelinková M, Rihová B, Ulbrich K. New HPMA copolymers containing doxorubicin bound via pH-sensitive linkage: synthesis and preliminary *in vitro* and *in vivo* biological properties. Journal of controlled release 2001; 73(1):89–102.

63. Ulbrich K, Šubr V. Polymeric anticancer drugs with pH-controlled activation. Advanced drug delivery reviews 2004; 56(7):1023–50.

64. Tannock IF, Rotin D. Acid pH in tumors and its potential for therapeutic exploitation. Cancer research 1989; 49(16):4373–84.

65. Martin GR, Jain RK. Noninvasive measurement of interstitial pH profiles in normal and neoplastic tissue using fluorescence ratio imaging microscopy. Cancer research 1994; 54(21):5670–4.

66. Cardone RA, Casavola V, Reshkin SJ. The role of disturbed pH dynamics and the Na+/H+ exchanger in metastasis. Nature reviews. Cancer 2005; 5(10):786–95.

67. Gillies RJ, Raghunand N, Karczmar GS, Bhujwalla ZM. MRI of the tumor microenvironment. Journal of magnetic resonance imaging JMRI 2002; 16(4):430–50.

68. Gatenby RA, Gillies RJ. Why do cancers have high aerobic glycolysis? Nature reviews. Cancer 2004; 4(11):891–9.

69. Rodewald R, Karnovsky MJ. Porous substructure of the glomerular slit diaphragm in the rat and mouse. The Journal of cell biology 1974; 60(2):423–33.

70. Haraldsson B, Nystrom J, Deen WM. Properties of the glomerular barrier and mechanisms of proteinuria. Physiological reviews 2008; 88(2):451–87.

71. Etrych T, Strohalm J, Chytil P, Cernoch P, Starovoytova L, Pechar M *et al.* Biodegradable star HPMA polymer conjugates of doxorubicin for passive tumor targeting. European journal of pharmaceutical sciences 2011; 42(5):527–39.

72. Etrych T, Kovář L, Strohalm J, Chytil P, Rihová B, Ulbrich K. Biodegradable star HPMA polymer-drug conjugates: Biodegradability, distribution and anti-tumor efficacy. Journal of controlled release 2011; 154(3):241–8.

73. Sadekar S, Linares O, Noh G, Hubbard D, Ray A, Janat-Amsbury M *et al.* Comparative pharmacokinetics of PAMAM-OH dendrimers and HPMA copolymers in ovarian-tumor-bearing mice. Drug delivery and translational research 2013; 3(3):260–71.

74. Zanetti SR, Maldonado EN, Aveldano MI. Doxorubicin affects testicular lipids with long-chain (C_{18}-C_{22}) and very long-chain (C_{24}-C_{32}) polyunsaturated fatty acids. Cancer research 2007; 67(14):6973–80.

75. Shinoda K, Mitsumori K, Yasuhara K, Uneyama C, Onodera H, Hirose M *et al.* Doxorubicin induces male germ cell apoptosis in rats. Archives of Toxicology 1999; 73(4-5):274–81.

76. Vogelzang NJ, Bronson D, Savino D, Vessella RL, Fraley EF. A human embryonal-yolk sac carcinoma model system in athymic mice. Cancer 1985; 55(11):2584–93.

77. Mueller T, Voigt W, Simon H, Frühauf A, Bulankin A, Grothey A *et al.* Failure of activation of caspase-9 induces a higher threshold for apoptosis and cisplatin resistance in testicular cancer. Cancer research 2003; 63(2):513–21.

78. Behrens BC, Hamilton TC, Masuda H, Grotzinger KR, Whang-Peng J, Louie KG *et al.* Characterization of a cis-diamminedichloroplatinum(II)-resistant human ovarian cancer cell line and its use in evaluation of platinum analogues. Cancer research 1987; 47(2):414–8.

79. McDonald PC, Winum J-Y, Supuran CT, Dedhar S. Recent developments in targeting carbonic anhydrase IX for cancer therapeutics. Oncotarget 2012; 3(1):84–97.

80. Aird RE, Cummings J, Ritchie AA, Muir M, Morris RE, Chen H *et al. In vitro* and *in vivo* activity and cross resistance profiles of novel ruthenium (II) organometallic arene complexes in human ovarian cancer. British journal of cancer 2002; 86(10):1652–7.

81. Koch M, Krieger ML, Stölting D, Brenner N, Beier M, Jaehde U *et al.* Overcoming chemotherapy resistance of ovarian cancer cells by liposomal cisplatin: molecular mechanisms unveiled by gene expression profiling. Biochemical pharmacology 2013; 85(8):1077–90.

82. Whiteside TL. The tumor microenvironment and its role in promoting tumor growth. Oncogene 2008; 27(45):5904–12.

83. Mbeunkui F, Johann DJ JR. Cancer and the tumor microenvironment: a review of an essential relationship. Cancer chemotherapy and pharmacology 2009; 63(4):571–82.

84. Netti PA, Berk DA, Swartz MA, Grodzinsky AJ, Jain RK. Role of extracellular matrix assembly in interstitial transport in solid tumors. Cancer research 2000; 60(9):2497–503.

85. Tafreshi NK, Lloyd MC, Bui MM, Gillies RJ, Morse DL. Carbonic anhydrase IX as an imaging and therapeutic target for tumors and metastases. Sub-cellular biochemistry 2014; 75:221–54.

86. Loncaster JA, Harris AL, Davidson SE, Logue JP, Hunter RD, Wycoff CC *et al.* Carbonic anhydrase (CA IX) expression, a potential new intrinsic marker of hypoxia: correlations with tumor oxygen measurements and prognosis in locally advanced carcinoma of the cervix. Cancer research 2001; 61(17):6394–9.

87. Švastová E, Huliková A, Rafajová M, Zat'ovičová M, Gibadulinová A, Casini A *et al.* Hypoxia activates the capacity of tumor-associated carbonic anhydrase IX to acidify extracellular pH. FEBS letters 2004; 577(3):439–45.

88. Kim J-w, Dang CV. Cancer's molecular sweet tooth and the Warburg effect. Cancer research 2006; 66(18):8927–30.

89. Van der Heiden MG, Cantley LC, Thompson CB. Understanding the Warburg effect: the metabolic requirements of cell proliferation. Science 2009; 324(5930):1029–33.

90. Lu P, Weaver VM, Werb Z. The extracellular matrix: a dynamic niche in cancer progression. The Journal of cell biology 2012; 196(4):395–406.

91. Reddy LH, Couvreur P (eds.). Macromolecular Anticancer Therapeutics. Springer-Verlag New York; 2010; Part II, Chapter 3: 87-132 .

92. Herzog CE, Trepel JB, Mickley LA, Bates SE, Fojo AT. Various Methods of Analysis of mdr-1/P-Glycoprotein in Human Colon Cancer Cell Lines. JNCI Journal of the National Cancer Institute 1992; 84(9):711–6.

93. Jensen KD, Nori A, Tijerina M, Kopečková P, Kopeček J. Cytoplasmic delivery and nuclear targeting of synthetic macromolecules. Journal of Controlled Release 2003; 87(1-3):89–105.

94. Callahan J, Kopečková P, Kopeček J. Intracellular trafficking and subcellular distribution of a large array of HPMA copolymers. Biomacromolecules 2009; 10(7):1704–14.

Declaration of Original Authorship

Selbstständigkeitserklärung

Hiermit erkläre ich gemäß §5 der Promotionsordnung der Naturwissenschaftlichen Fakultät I der Martin-Luther Universität Halle-Wittenberg, dass ich die Ergebnisse der vorliegenden Arbeit unter Anleitung von Herrn Professor Dr. rer. nat. habil. Karsten Mäder selbständig erarbeitet und die Dissertation ohne fremde Hilfe verfasst habe.

Ferner erkläre ich, dass ich keine anderen als die von mir angegebenen Quellen oder Hilfsmittel verwendet und inhaltlich oder wörtlich übernommene Stellen als solche kenntlich gemacht habe.

Beiträge von Kooperationspartnern zu den Ergebnissen dieser Arbeit habe ich eindeutig gekennzeichnet.

Weiterhin erkläre ich, dass die vorliegende Arbeit keiner anderen Fakultät zur Erlangung eines akademischen Grades vorgelegt wurde und ich mich zuvor noch nicht um die Erlangung eines Doktorgrades beworben habe.

Kiel, den 25.04.2017

Anne-Kathrin Heinrich

Acknowledgements

Many people deserve my deep gratitude because without them, this work would not have been possible.

First of all, I want to thank my supervisor Professor Dr. Karsten Mäder for the opportunity to join his group and to perform this interdisciplinary work. Thank you very much, for your assistance, the trust in my work and also for your encouragement whenever it was needed.

I further want to give my special thanks to Dr. Thomas Müller. Thank you for your assistance during all of my *in vivo* and *in vitro* trials, for so many hours of fruitful discussions, for your sustained encouragement and optimism when I was stumbling, for celebrating our successes and for thousands of i.v. injections to the mice.

I also want to gratefully acknowledge the work of my cooperation partners from the Institute of Macromolecular Chemistry in Prague. Thank you Tomáš Etrych (PhD), Petr Chytil (PhD), Robert Pola (PhD), Lucie Schindler, Libor Kostka (PhD), Albert Koválik, A. Hoferová and Martin Studenovský (PhD) for the synthesis of my polymers, the interesting discussions, our common publications and for the warm welcome at our visit in Prague.

Furthermore, I want to thank Dr. Henrike Lucas for her valuable help during my *in vivo* and *in vitro* studies, for her excellent advice, several hours in front of the fluorescence imaging system and finally for becoming a good friend. Sincere thanks also go to Franziska Reipsch, for her excellent practical assistance during my *in vitro* trials, her patience when things have to be done again and again, for several tumor sections and for a very nice atmosphere in the laboratory. I also want to thank Dr. Bernhard Hiebl, Martina Hennicke and the animal care attendants of the ZMG, for continuously taking care of my laboratory animals.

Undoubtedly, this work would not have been possible without the financial support. In this regard, the Deutsche Forschungsgemeinschaft is acknowledged for the financial Support (MA 1648/8-1).

I also want to thank Stefan Hoffmann for its very helpful introduction to the group and especially to the mice studies. Thanks also go to Johannes Stelzner for being my office mate in my first year, his nice introduction to the group, for cooking coffee and for his steady help with my PC. Special thanks go also to all members of the group of Professor Dr. Karsten Mäder.

Thank you for the warm welcome, for laughing and crying together, for the nice trips and celebrations and unforgettable evenings in the university. Of course the technical assistants Ute Mentzel and Kerstin Schwarz should not be forgotten. Thank you for your assistance in the laboratory and during the practical courses. Also Claudia Bertram is acknowledged for her steady support with the bureaucracy.

Warm thanks go to Juliane Frank, for being my office mate in the last two years. Thank you so much for the incredible time filled with discussions, talks, laugh, crying, and a lot of tea. And finally thank you for becoming a soulmate and a very good friend.

I also want to give special thanks to my family and friends for their steady support and their trust in me.

Finally, I want to express my deep gratitude to Andreas, for being at my side, for his trust in me and my work, his enduring patience, his steady encouragement when I was stumbling and for his love.

Curriculum Vitae

Persönliche Daten

Name	Anne-Kathrin Heinrich
Geburtsdatum	27.12.1986
Geburtsort	Hennigsdorf

Ausbildung und praktische Erfahrungen

Seit Februar 2017	Apothekerin in der Apotheke des Friedrich-Ebert-Krankenhauses Neumünster
November 2014 – November 2015	Teilzeittätigkeit als Apothekerin, Stern-Apotheke Halle
Mai 2013 – Februar 2017	Wissenschaftliche Mitarbeiterin, AG Prof. Dr. Karsten Mäder, Institut für Pharmazie, Martin-Luther Universität Halle-Wittenberg
Februar 2012 – April 2013	Apothekerin in der Krankenhausapotheke der Ruppiner Kliniken
Januar 2012	Approbation zum Apotheker 3.Staatsexamen
November 2011 – Dezember 2011	Mitarbeiterin in der Krankenhausapotheke der Ruppiner Kliniken
Mai 2011 – Oktober 2011	Pharmazeut im Praktikum, Krankenhausapotheke der Ruppiner Kliniken
November 2010 – April 2011	Pharmazeut im Praktikum, Ahorn Apotheke Velten
Oktober 2010	2. Staatsexamen
Oktober 2008 – Oktober 2010	Hauptstudium der Pharmazie an der Freien Universität Berlin
August 2008	1. Staatsexamen
Oktober 2006 – August 2008	Grundstudium der Pharmazie an der Freien Universität Berlin
August 1999 – Juni 2006	Hedwig-Bollhagen-Gymnasium Velten, Abitur

Publications

Articles

- Pola R, **Heinrich A-K**, Mueller T, Kostka L, Mäder K, Pechar M, Etrych T. **Passive Tumor Targeting of Polymer Therapeutics: In Vivo Imaging of Both the Polymer Carrier and the Enzymatically Cleavable Drug Model**. Macromolecular bioscience 2016; 16(11):1577–82.

- **Heinrich A-K**, Lucas H, Schindler L, Chytil P, Etrych T, Mäder K, Mueller, T. **Improved Tumor-Specific Drug Accumulation by Polymer Therapeutics with pH-Sensitive Drug Release Overcomes Chemotherapy Resistance.** Molecular cancer therapeutics 2016; 15(5):998–1007.

- Studenovsky M, **Heinrich A-K**, Lucas H, Mueller T, Mäder K, Etrych T. **Dual fluorescent N-(2-hydroxypropyl) methacrylamide-based conjugates for passive tumor targeting with reduction-sensitive drug release: Proof of the concept, tumor accumulation, and biodistribution.** Journal of Bioactive and Compatible Polymers 2016; 31(4):348–60.

Conference Contributions

- **Heinrich A-K**, Caysa H, Etrych T, Schindler L, Chytil P, Hoffmann S, Mäder K, Mueller T. **Improved Tumor Specific Drug Accumulation by Polymer Therapeutics with pH-sensitive Drug Release overcomes Chemotherapy Resistance.** The 42nd Annual Meeting and Exposition of the Controlled Release Society, 2015, Edinburgh, Scotland (Poster)

- **Heinrich A-K,** Etrych T, Schindler L, Hoffmann S, Caysa H, Mäder K, Mueller T. **Biodistribution and efficacy of pH-sensitive HPMA copolymer drug delivery systems in cancer treatment.** 9th World Meeting on Pharmaceutics, Biopharmaceutics and Pharmaceutical Technology, 2014, Lisbon, Portugal (Poster)

- Mäder K, Caysa H, Hoffmann S, **Heinrich A-K**, Mueller T. **Nano drug delivery systems for passive tumor targeting – hope or hype?** Special Issue: Abstracts of the 94th Annual Meeting of the German Physiological Society, 5-7 March 2015 (Acta Physiologica 213:30-31 · March 2015)